ELECTROMAGNETIC SIMULATION AND OPTIMIZATION OF AN ELECTROMAGNETIC LAUNCHER

A THESIS SUBMITTED TO
THE GRADUATE SCHOOL OF NATURAL AND APPLIED SCIENCES
OF
MIDDLE EAST TECHNICAL UNIVERSITY

BY

DOĞA CEYLAN

IN PARTIAL FULFILLMENT OF THE REQUIREMENTS
FOR
THE DEGREE OF MASTER OF SCIENCE
IN
ELECTRICAL AND ELECTRONICS ENGINEERING

AUGUST 2018

Approval of the thesis:

ELECTROMAGNETIC SIMULATION AND OPTIMIZATION OF AN ELECTROMAGNETIC LAUNCHER

submitted by **DOĞA CEYLAN** in partial fulfillment of the requirements for the degree of **Master of Science in Electrical and Electronics Engineering Department, Middle East Technical University** by,

Prof. Dr. Halil Kalıpçılar _____
Dean, Graduate School of **Natural and Applied Sciences**

Prof. Dr. Tolga Çiloğlu _____
Head of Department, **Electrical and Electronics Engineering**

Assist. Prof. Dr. Ozan Keysan _____
Supervisor, **Electrical and Electronics Engineering, METU**

Examining Committee Members:

Assist. Prof. Dr. Emine Bostancı
Electrical and Electronics Engineering, METU _____

Assist. Prof. Dr. Ozan Keysan
Electrical and Electronics Engineering, METU _____

Assist. Prof. Dr. Murat Göl
Electrical and Electronics Engineering, METU _____

Assist. Prof. Dr. Orkun Özşahin
Mechanical Engineering, METU _____

Prof. Dr. Müslüm Cengiz Taplamacıoğlu
Electrical and Electronics Engineering, Gazi University _____

Date: _____

I hereby declare that all information in this document has been obtained and presented in accordance with academic rules and ethical conduct. I also declare that, as required by these rules and conduct, I have fully cited and referenced all material and results that are not original to this work.

Name, Last Name: Doğa Ceylan

Signature :

ABSTRACT

ELECTROMAGNETIC SIMULATION AND OPTIMIZATION OF AN ELECTROMAGNETIC LAUNCHER

Ceylan, Doğa
M.S., Department of Electrical and Electronics Engineering
Supervisor : Assist. Prof. Dr. Ozan Keysan

August 2018, 126 pages

Electromagnetic launcher (EML) is an electromagnetic accelerator which uses electrical pulse power instead of conventional gunpowder. A large amount of electric current in the pulse waveform flows in the rails and armature. This current creates large magnetic field between rails. As a result of Lorentz force, armature and projectile accelerate. In this study, finite element (FE) model of an EML which includes both pulsed power supply (PPS) circuits with 2 MJ total electrical energy and barrel with 3 m length is developed. In the barrel side of the model, armature movement is simulated with stationary mesh elements using external variable resistances and inductances depending on the armature velocity, position, frequency of the excitation current and inductance gradient. In addition to the current density and magnetic field distribution in the barrel, alternating current (AC), contact, velocity skin effect and back electromotive force (EMF) resistances are investigated for the described switching scenario of the PPS creating pulsed shaped excitation current with 1 MA peak. Muzzle velocity of projectile and armature with 0.125 kg total mass is found to be 2040 m/s. Total muzzle kinetic energy and system efficiency are calculated as 260 kJ

and 13%, respectively. Outputs of the electromagnetic simulations of the designed EML are verified with experimental results. Moreover, the effect of lamination thickness of the containment which supports the rails mechanically is observed. Although using containment in the barrel side is a requirement in order not to lose the contact between the rails and armature, it decreases the efficiency of the launcher because of the eddy currents in the conducting containment. It is concluded that using laminations thicker than 10 mm in the containment is not reliable from the electromagnetic point of view. Finally, armature shape optimization study is presented in the last chapter. The objective function of the optimization study is the muzzle kinetic energy of the projectile. Genetic algorithm (GA) is used as the optimization method. Maximum contact current density and electromagnetic deflection pressure on the armature are chosen as constraints. Since the contact resistance affects the distribution of the contact current density, it is also modeled as thin layers between the rails and armature with variable resistivities depending on the contact pressure values acting on each thin layer.

Keywords: electromagnetic launcher, railgun, finite element method, velocity skin effect resistance, contact resistance, containment lamination, armature shape optimization

ÖZ

ELEKTROMANYETİK FIRLATMA SİSTEMİ SİMÜLASYONU VE OPTİMİZASYONU

Ceylan, Doğa
Yüksek Lisans, Elektrik ve Elektronik Mühendisliği Bölümü
Tez Yöneticisi : Dr. Öğretim Üyesi Ozan Keysan

Ağustos 2018 , 126 sayfa

Elektromanyetik fırlatma sistemi (EMFS) barut yerine elektriksel darbe uyartı gücünü kullanan bir elektromanyetik hızlandırıcıdır. Darbe uyartısı şeklinde yüksek miktarda elektrik akımı raylardan ve armatürden geçer. Bu akım raylar arasında yüksek miktarda manyetik alan oluşturur. Lorentz kuvvetinin sonucu olarak, armatür ve mühimmat hızlanır. Bu çalışmada, EMFS'nin 2 MJ başlangıç enerjisine sahip darbe güç kaynağını (DGK) ve 3 m uzunluğundaki namlusunu içeren sonlu eleman (SA) modeli geliştirilmiştir. Modelin namlu tarafında, armatür hızına, pozisyonuna, uyartı akımının frekansına ve endüktans gradyantına bağlı olarak değişen direnç ve endüktans yardımı ile armatür hareketi durağan elemanlar kullanılarak simüle edilmiştir. Namludaki akım ve manyetik alan dağılımına ek olarak, 1 MA tepe değerli darbe uyartı akımını yaratan DGK anahtarlama senaryosu için alternatif akım (AA), kontak, hız yüzey etkisi ve zıt elektromotor kuvveti direnci incelenmiştir. Toplam 0.125 kg kütlesindeki armatür ve mühimmatın namlu çıkış hızı 2040 m/s olarak bulunmuştur. Toplam namlu çıkış enerjisi ve sistemin toplam verimi ise sırayla 260 kJ ve %13 olarak hesaplanmıştır. Tasarlanan EMFS'nin elektromanyetik similasyonunun çıktıları test

sonuçları ile doğrulanmıştır. Buna ek olarak, rayları mekanik olarak destekleyen nüvenin laminasyonunun etkisi incelenmiştir. Raylar ve armatür arasındaki kontağı kaybetmemek için nüvenin kullanımı namlu tarafında bir gereklilik olmasına rağmen, atış sırasında nüve içerisinde endüklenen akımlar iletken bir malzemeden yapılmış nüvede kayıplara sebebiyet vermektedir. Bu durum EMFS'nin verimini azaltmaktadır. Elektromanyerik açıdan 10 mm'den daha kalın laminasyonlu nüve kullanımının mantıklı olmadığı sonucuna varılmıştır. Son olarak, armatür şekli optimizasyonu çalışması tezin son kısmında sunulmuştur. Amaç fonksiyonu mühimmat çıkış enerjisi olarak belirlenmiştir. Optimizasyon yöntemi olarak genetik algoritma (GA) kullanılmıştır. Kontak yüzeyindeki maksimum akım yoğunluğu ve armatür içerisinde oluşan ve armatürü deforme eden basınçlar optimizasyonun kısıtlayıcıları olarak seçilmiştir. Kontak direnci kontak yüzeyindeki akım dağılımını etkilediği için kontak direnci de raylar ve armatür arasında ince katmanlar halinde modele eklenmiştir. Bu ince katmanların direnci bu katmanlara uygulanan elektromanyetik kontak basıncına bağlı olarak değişmektedir.

Anahtar Kelimeler: elektromanyetik fırlatma sistemi, raylı silah, sonlu eleman analizi, hız yüzey etkisi direnci, kontak direnci, nüve laminasyonu, armatür şekli optimizasyonu

To my father and mother...

ACKNOWLEDGMENTS

First, and most of all, I would like to convey my gratefulness to Assist. Prof. Dr. Ozan Keysan for providing me an opportunity to complete this study. Without his expertise, assistance, guidance and patience, this thesis would not have been possible. I feel really lucky to be one of his graduate students and a part of his research group, which is called METU Power Lab.

I would like to thank my committee members, Assist. Prof. Dr. Emine Bostancı, Assist. Prof. Dr. Murat Göl, Assist. Prof. Dr. Orkun Özşahin and Prof. Dr. Müslüm Cengiz Taplamacıoğlu for their support, suggestions and encouragement.

I would like to extend my sincere gratitude to ASELSAN Inc. for its valuable support throughout my graduate studies. I would like to give special thanks to Mustafa Karagöz, Baran Yıldırım, Yasin Çevik and Anıl Civil, who helped me a lot during this project.

I also would like to thank my friends, who I have been working together in METU Power Lab. They have each made my time at Middle East Technical University more positive and enjoyable. Especially, I would like to thank Erencan Duymaz, Aysel Akgemci, Siamak P. and İlker Şahin, who together make invaluable contributions to my academic and personal life. Also, I want to thank my roomie, Uğur Güdelek. In addition to his contributions to the armature shape optimization study, his ideas and advices were very significant for the whole study. Moreover, I express my deepest gratefulness to Ceren Arslan for her support during this thesis. Without her, everything in my life would be incomplete.

Lastly, there are no words to express my gratefulness to my mother and father. They have believed in and supported me during my whole life.

TABLE OF CONTENTS

LIST OF TABLES

TABLES

LIST OF FIGURES

FIGURES

LIST OF ABBREVIATIONS

AC	Alternating Current
DC	Direct Current
EMF	Electromotive Force
EML	Electromagnetic Launcher
FE	Finite Element
FEM	Finite Element Method
ISL	Institute Saint Louis
NRL	Naval Research Laboratory
PPS	Pulsed Power Supply
VSE	Velocity Skin Effect

LIST OF SYMBOLS

a	Acceleration
$\vec{A}$	Magnetic Vector Potential
$\vec{B}$	Magnetic Flux Density Vector
c	Length of Caliber (Distance between the rails)
C	Capacitance of a Capacitor Bank
c_p	Specific Heat Capacity
d	Density
$\vec{D}$	Electric Flux Density Vector
E	Induced Electromotive Force
$\vec{E}$	Electric Field Intensity Vector
f	Frequency
$\vec{f}$	Electromagnetic Force Density Vector
F_{arm}	Electromagnetic Force on Armature in Shot Direction
F_{cont}	contact Force between One Rail and Armature
F_{fric}	Frictional Force on Armature
F_{net}	Net Force Acting on Armature
h	Height of the Rail
$\vec{H}$	Magnetic Field Intensity Vector
H_{soft}	Hardness of Softer Contact Member
I_{EML}	Electromagnetic Launcher Excitation Current
$\vec{J}$	Current Density Vector
k	Thermal Conductivity
k_c	Contact Resistance Constant
K_{vse}	VSE proportionality constant
k_0	First Experimental Contact Transition Constant
l	Length of Rails

l_{arm}	Length of Armature
L_c	Internal Inductance of a Capacitor Bank
L_{cable}	Inductance of Discharging Cable
$L_{crowbar}$	Internal Inductance of Crowbar Diode Stack
L_{EML}	Total Inductance of Rails and Armature
L_{ind}	Inductance of Pulse Shaping Inductor
l_{wing}	Length of Armature Wing
L'	Inductance Gradient
m	Second Experimental Contact Transition Constant
N	Number of Turns
P_c	Contact Pressure
R_{AC}	Alternating Current Resistance
$R_{back\ EMF}$	Back Electromotive Force Resistance
R_c	Contact Resistance
R_{cable}	Resistance of Discharging Cable
$R_{crowbar}$	Internal Resistance of Crowbar Diode Stack
R_{DC}	DC Resistance of Barrel
R'_{DC}	DC Resistance of Barrel for 1 m armature position
R_{EML}	Total Resistance of Rails and Armature
R_{ind}	Internal Resistance of Pulse Shaping Inductor
R_{sgs}	Internal Resistance of a Spark Gap Switch
R_{VSE}	Velocity Skin Effect Resistance
v	Velocity of Armature
V	Electric Scalar Potential
V_c	Initial Voltage of a Capacitor Bank
V_{breech}	Breech Voltage
w	Thickness of Rails
W	Stored Energy
W'	Coenergy
x	Armature Displacement after Preload Position

$x_{preload}$	Preload Position of Armature
α	Shaping Parameter of Dynamic Friction Coefficient
δ	Skin Depth
ε	Permittivity of Dielectric
ε_r	Relative Permittivity
ε_0	Permittivity of Free Space
η	Efficiency
λ	Total Magnetic Flux
μ	Permeability
μ_G	Limiting Value of Dynamic Friction Coefficient
μ_H	Static Friction Coefficient
μ_r	Relative Permeability
$\mu(v)$	Velocity Dependent Dynamic Friction Coefficient
μ_0	Permeability of Vacuum
ρ	Resistivity
ρ_v	Volume Charge Density
σ	Electric Conductivity
ϕ	Magnetic Flux

CHAPTER 1

INTRODUCTION

1.1 Brief Information on Electromagnetic Launchers

Electromagnetic launcher (EML), also known as railgun, is an electromagnetic device that converts electromagnetic energy into mechanical energy. It consists of two parallel rails, a conducting armature and a non-conducting projectile as shown in Fig. 1.1.

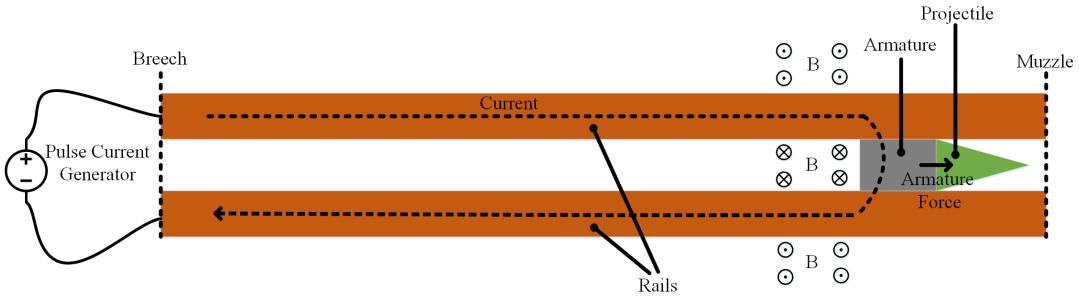

Figure 1.1: Working principle of an electromagnetic launcher.

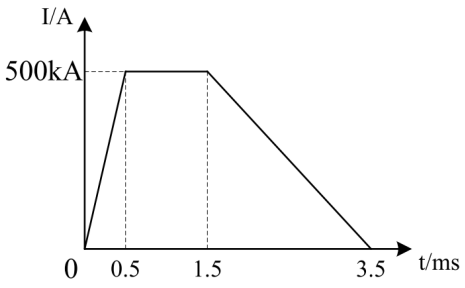

Figure 1.2: Typical current pulse, [1].

Large amount of pulse current is generated by pulsed power supply (PPS) to excite

EML. Typical current pulse is given as in Fig. 1.2, [1]. The current flows through the rails and armature. Electric current creates a magnetic field which causes an electromagnetic force on the armature due to Lorentz force. Electromagnetic force acting on a moving particle, with charge q and velocity v, can be expressed as in Eq. (1.1).

$$\vec{F}_{particle} = q\vec{v} \times \vec{B} \tag{1.1}$$

Electromagnetic force on the armature can be calculated by integrating Eq. (1.1) through the armature volume as in Eq. (1.2) where $\vec{F}_{\text{arm}}$, $\vec{J}$ and $\vec{B}$ are Lorentz force acting on the armature, current density and magnetic field, respectively.

$$\vec{F}_{arm} = \iiint \vec{J} \times \vec{B}\, dV \tag{1.2}$$

During the excitation, armature accelerates between the rails due to Lorentz force. According to Newton's laws of motion, acceleration of the projectile and armature can be calculated using Eq. (1.3) where F_{arm} is Lorentz force acting on armature in the shot direction, F_{fric} is frictional force on the armature, m_{total} is the total mass of projectile and armature.

$$a = \frac{F_{arm}(t) - F_{fric}(t)}{m_{total}} \tag{1.3}$$

The armature velocity when it leaves the rails, called muzzle velocity, can be calculated using Eq. (1.4) where v_{muzzle} is the muzzle velocity, t_{exit} is the time until armature leaves the rails.

$$v_{muzzle} = \int_0^{t_{exit}} \frac{F_{arm}(t) - F_{fric}(t)}{m_{total}} dt \tag{1.4}$$

System efficiency is expressed as in Eq. (1.5) where $\eta_{\text{ total}}$ is the efficiency of total system, E_{kin} is the muzzle kinetic energy and E_{PPS} is the input electrical energy of

PPS.

$$\eta_{total} = \frac{E_{kin}}{E_{PPS}} \tag{1.5}$$

The common PPS topologies used in EMLs will be disscussed in Section 1.4. Capacitive PPS is one of the most efficient PPS types, [2]. Also, in this study capacitive PPS modules are used to excite the launcher. Moreover, in order to increase the efficiency, it is reliable to use more than one PPS module in parallel, [3]. Input electrical energy of this type PPS modules can be expressed as in Eq. (1.6) where n is the number of parallel PPS modules, C is the capacitance of capacitor used in one module and V_c is the initial voltage of the capacitor.

$$E_{PPS} = n\,\frac{1}{2}\,C\,V_c^2 \tag{1.6}$$

Although input electrical energy of PPS of an EML can reach hundreds of MJs, total system efficiency cannot exceed 50% due to the theoretical limitations, [4], [5]. In order to increase the efficiency, inductance gradient is the most significant parameter in EMLs. During the motion of armature, the inductance of rails increases approximately linearly. Hence, the change of inductance with respect to the armature position which is called inductance gradient is constant during the launch as in Eq. (1.7) where L' is inductance gradient, L is the barrel inductance and x is the armature position.

$$L' = \frac{\partial L}{\partial x} \tag{1.7}$$

In addition to the inductance, barrel side has also a resistance. The calculation of barrel resistance during the launch is a complex task due to the effect of armature velocity, frequency of pulsed shape current and contact transition between rails and armature, which will be discussed in Section 1.5.5.

Moreover, in addition to the electromagnetic propulsive force acting on the armature in the acceleration direction, large amount of excitation current creates electromagnetic deflection forces on the rails as in Fig. 1.3 . Due to the deflection forces, rails repel each other during the excitation. Therefore, using mechanical support around

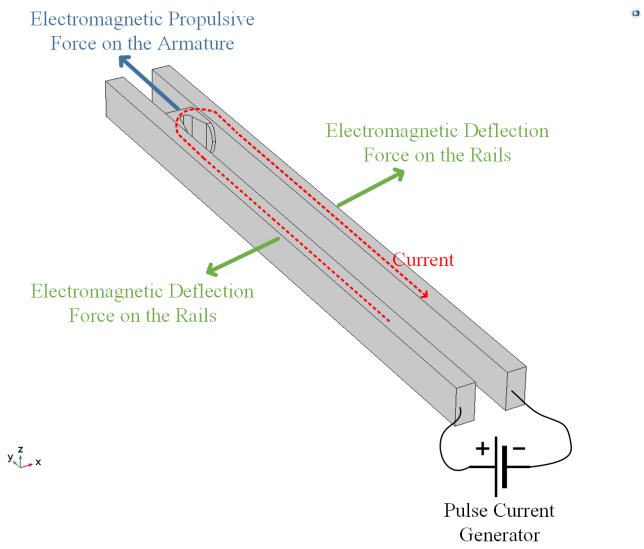

Figure 1.3: 3D view of rails and armature with the direction of electromagnetic forces.

the rails is a requirement in order not to lose the electrical contact between the rails and armature.

The mostly used PPS circuit topologies and the challenges on the barrel side will be presented in Section 1.4 and 1.5, respectively. Before the discussion on the topologies and challenges, it is significant to go through the properties of the EML used in the study.

1.2 Properties of the EML Used in the Study

In Turkey, ASELSAN Inc. has been developing an EML prototype since 2014, see Fig. 1.4, [6]. PPS modules with total energy of 1 MJ and 25 mm x 25 mm square bore 3 m barrel have been built at ASELSAN. In the early experiments, launch package with a total mass of 38 g is accelerated using the EML prototype called Tufan. The muzzle velocity is measured as 1000 m/s.

This study is funded by ASELSAN Inc. to analyze and optimize the electromagnetic aspects of Tufan. In the study, 10 PPS modules are used in parallel to accelerate a total mass of 0.125 kg instead of 5 modules and 38 g as in [6]. Hence, although electrical parameters of the PPS modules and geometric parameters of the barrel is

Figure 1.4: ASELSAN's EML: Tufan, [6].

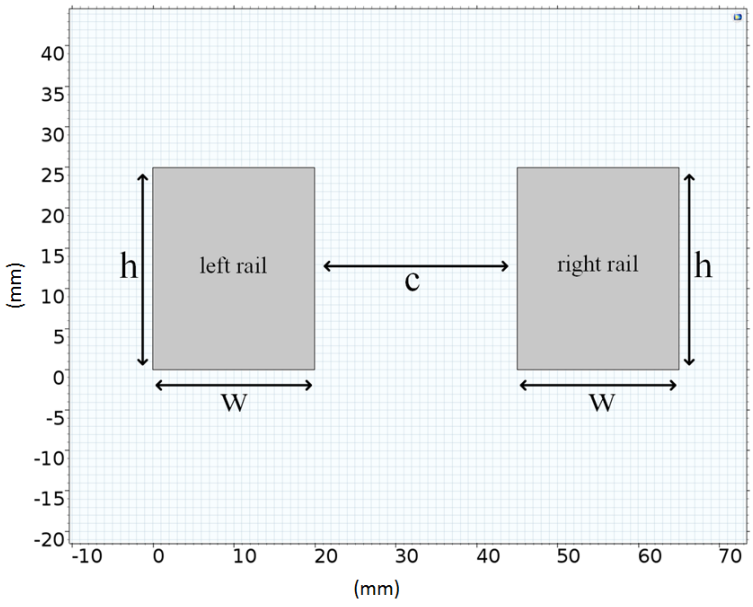

Figure 1.5: Rail and caliber dimensions on the rail cross section view.

the same with the ones presented in [6], PPS modules have 2 MJ total energy to reach 1 MA peak excitation current. In Fig. 1.5, cross section view of the Tufan's rails are presented. In this figure, w is the thickness of the rails, h is the height of the rails and c is the caliber. In Table 1.1, the values of these parameters are given.

Table 1.1: Geometric parameters of Tufan's barrel, [6]

rail thickness: w	20 mm
rail height: h	25 mm
caliber: c	25x25 mm
barrel length: l	3 m

Capacitive PPS topology is used as pulse power generation units in Tufan. In addition to the barrel side, the electrical parameters of the PPS units are also given in [6]. The view of PPS which consists of 5 capacitor bank units each of which has 200 kJ electrical energy is given in Fig. 1.6. The schema of one unit is given in Fig. 1.7. Working principle of this topology will be discussed in Section 1.4.1. The parameters of one PPS unit are available in Table 1.2.

Figure 1.6: The view of PPS units of Tufan placed in a container, [6].

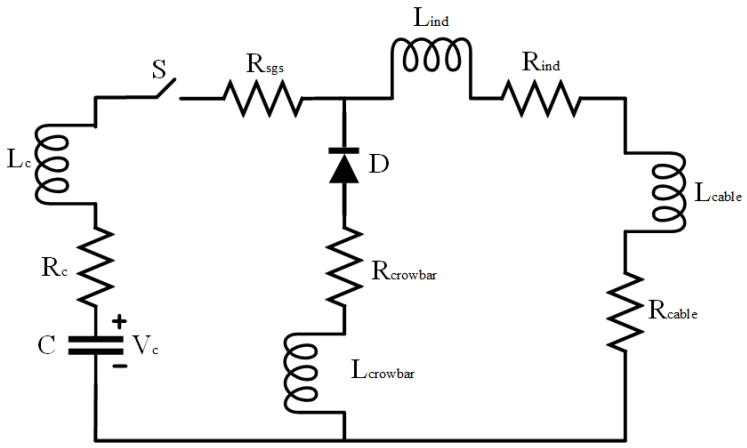

Figure 1.7: Schema of Tufan's short circuited single PPS module.

Table 1.2: Electrical parameters of Tufan's PPS units, [6].

Symbol	**Description**	**Value**
C	Capacitance of one capacitor bank	4 mF
V_c	Initial voltage of one capacitor bank	10 kV
R_c	Resistance of one capacitor bank	0.25 mΩ
L_c	Inductance of one capacitor bank	0.1 μH
R_{sgs}	Resistance value of spark gap switch	4 mΩ
$R_{crowbar}$	Resistance of crowbar diode stack	0.1 mΩ
$L_{crowbar}$	Inductance of crowbar diode stack	0.1 μH
R_{ind}	Resistance of pulse shaping inductor	0.1 mΩ
L_{ind}	Inductance of pulse shaping inductor	10 μH
R_{cable}	Resistance of discharging cable	0.9 mΩ
L_{cable}	Inductance of discharging cable	0.44 μH

In order to get 2 MJ input electrical energy, 10 identical PPS units each of which has 200 kJ energy are used in this study. Each spark gap switch conduct at different instant in order to excite the EML with pulse shaped current with 1 MA peak.

Materials of the armature, rails and containment are selected as aluminum, copper and annealed stainless steel 405, respectively. Some significant properties of these materials are given in Table 1.3, where σ, μ_r, ϵ_r, ρ and c_p are electrical conductivity, relative

permeability, relative permittivity, density and specific heat capacity, respectively.

Table 1.3: Properties of armature, rails and containment materials.

	σ (MS/m)	μ_r	ϵ_r	ρ (kg/m^3)	c_p (J/(kg*K))
Armature (aluminum)	37.74	1	1	2700	900
Rails (copper)	59.98	1	1	8960	385
Containment (stainless steel)	1.74	BH curve	1	7700	480

Before discussing the challenges on modeling PPS and barrel for an EML in detail, it is beneficial to review the history of EML technology.

1.3 History of Electromagnetic Launchers

Using electromagnetic force to accelerate projectiles is not a new idea. According to McNab's research, the first efforts to use electricity to power guns and launch projectiles started in 1844, [7]. Kolm *et al.* published an article called "Electromagnetic Launchers" [8] in 1980 to make a review of EMLs technology. This study shows that in these years, scientists were aware that it is possible to reach high muzzle velocities with EMLs. The first serious EML experiment was performed by Birkeland in Norway, with an EML of 6.5 cm caliber and 4 m barrel length, which is shown in Fig. 1.8, [9].

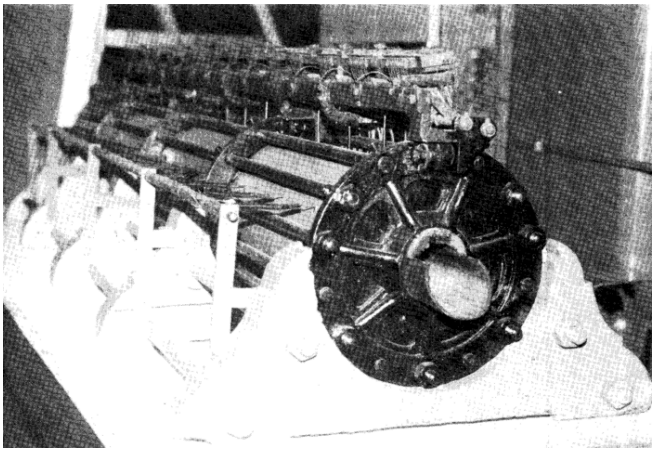

Figure 1.8: Birkeland's largest EML, [9].

Birkeland's work inspired a French scientist, Fauchon-Villeplee during Word War I. In [10], Fauchon-Villeplee designed a formidable EML with 128 MJ muzzle kinetic energy which is not achived even today. His long-range artillery gun mounted on a railway bogie was designed to launch 100 kg at 1600 m/s.

Although Fauchon-Villeplee's formidable design could not be implemented, an EML, with 10 MJ input electrical energy, was developed in French-German Institute Saint Louis (ISL) in France, [11]. PEGASUS facility is given in Fig. 1.9 with both barrel and PPS modules.

Figure 1.9: PEGASUS facility in ISL in 1999, [11].

United States has a long interest in technology of EMLs. In 1923, Naval Research Laboratory (NRL) was created within U.S. Navy to build an EML for use on future ships, [12]. In 2006, NRL published a paper, [13], to describe the designed EML with 21 kg launch mass, 2000 m/s muzzle velocity which means 42 MJ muzzle energy. In addition to NRL, EMLs are also investigated in Institute for Advanced Technology, University of Texas, Austin in United States. In [14], Fair explains the designed railgun system with 17 kg projectile mass and 420 m/s muzzle velocity as in Fig. 1.10.

In addition to United States and France, Germany always plays a key role in the development of defense industry technology. In 1940s, German scientist Dr. Hansler was also influenced by Fauchon-Villeplee's work. After he worked on his design

Figure 1.10: Test bench for the EML system developed in Institute for Advanced Technology, [12].

reports, Dr. Hansler decided to carry out Villeplee's EML with 200 kg projectile and 2000 m/s muzzle velocity. However, because of the necessities of World War II, he started to build a smaller EML with the goal of 2000 m/s and 6.5 kg projectile. For the pulse current generation, he used mechanical energy of homo-polar pulse generators as explained in the report of the work: [15]. During World War II, Japanese scientists also worked on EMLs. In 1946, they did some experiments on developed prototype with German scientists.

Although there exist a number of studies in the literature about EML technology, many scientists and engineers are still working on it to develop more realistic simulation model and more efficient launcher. In Section 1.4 and 1.5, pulsed power generation methods for EMLs and challenges on the barrel side will be discussed.

1.4 Pulsed Power Generation

EMLs consist of two main parts: the pulsed power supply (PPS) unit and the barrel. On one hand, in order to increase the electromagnetic force acting on the armature, large amount of current generation is required in PPS side. On the other hand, the excitation current should not be large when the armature leaves the barrel to reduce the

arc in the muzzle side. Therefore, the pulse current excitation is used in EMLs. After, current reaches its peak value rapidly, it stays at its peak for a while using parallel PPS modules which are fired at different instants. After all PPS modules are fired, current starts to decay slowly. The design of PPS units is critical to build an efficient EML. There exist three ways to generate pulse shaped current in the electromagnetic launch systems: inductive pulsed power supplies, pulsed alternators, capacitive pulsed power supplies.

1.4.1 Capacitive Pulsed Power Supplies

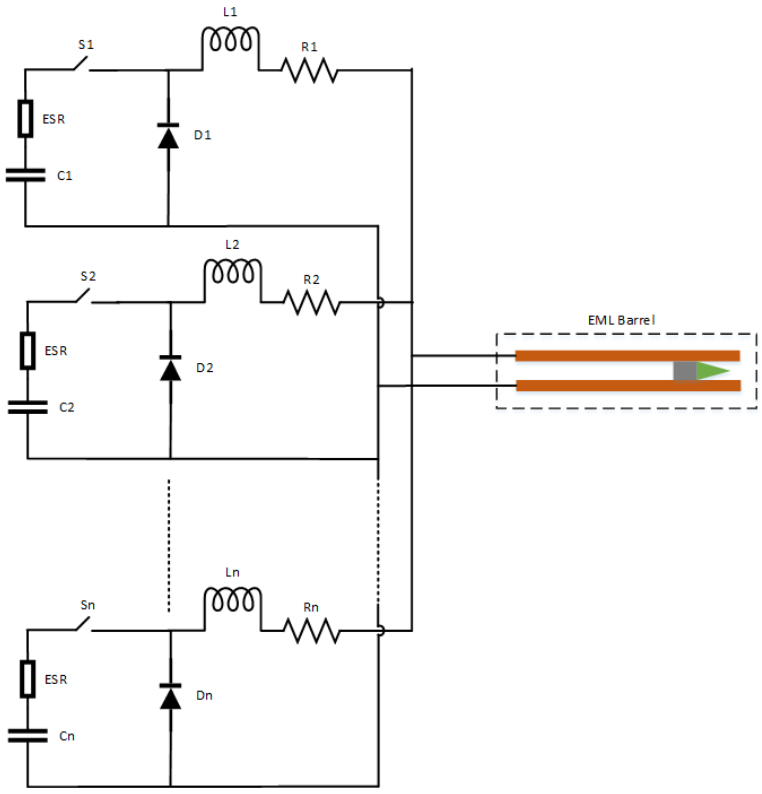

Figure 1.11: Capacitor-based pulsed power generation circuit.

The most favorable way to generate pulsed shape current is the capacitor-based PPS because of its ability to deliver the required power pulse, size and weight requirements, system placement constraints, and impact of energy losses, [16]. In [17], a capacitor-based pulsed power system is analyzed in terms of its efficiency. Moreover, Gou *et al.* work on the electric parameters of the capacitive PPS circuit topology in [18]. In Fig. 1.11, the circuit topology with n-state parallel PPS modules is given.

The working principle of one module is similar to the buck converter. Capacitor is charged to an initial voltage. After switch is closed, the capacitor starts discharging through the inductor and the rails and the armature of the EML. During the capacitor discharging process, the terminal current of the EML increases rapidly. Then, after the capacitor is fully discharged, free wheeling diode starts conducting. Hence, the inductor starts to discharge through the EML and diode. During the inductor discharging process, the terminal current of the EML decreases. Each module of the whole PPS unit has its own switching time instant.

1.4.2 Inductive Pulsed Power Supplies

In the literature, there exist two main circuit topologies used to generate inductive pulsed power: meat grinder and XRAM, [19].

Meat grinder circuit for energizing an EML was developed by Zucker *et al.* in 1986, [20]. Single stage meat grinder circuit configuration is given in Fig. 1.12 where L_1 and L_2 are coupled energy storage inductors.

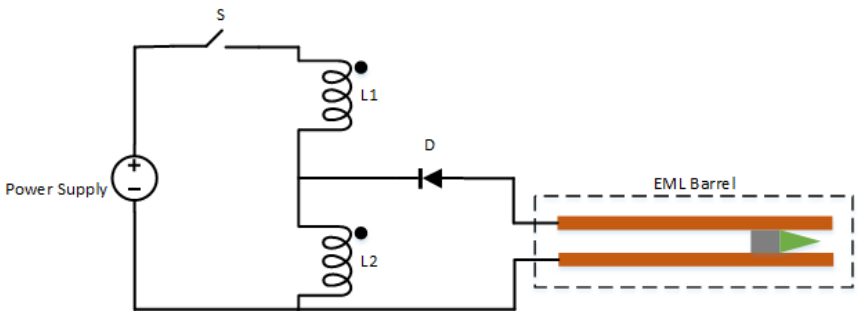

Figure 1.12: Generating pulsed power using meat grinder.

Working principle of this type of inductive pulse generation is explained in [21]. When "S" switch is closed, "D" diode is not conducting and feeding power supply charges the inductors. After "S" is opened, the magnitude of the current of L_1 decreases to zero because of the direction of coupling between L_1 and L_2. Hence, the energy stored in L_1 and the mutual inductance between L_1 and L_2 is instantly transferred to L_2. Therefore, meat grinder is an multiplication operation circuit. The relation between feeding current and the EML current is given in Eq. (1.8). This current

multiplication principle is also called as magnetic flux compression.

$$I_{EML_{max}} = (1 + \sqrt{\frac{L_1}{L_2}})I_{L_{1max}} \tag{1.8}$$

XRAM circuit topology was developed by a German scientist from Marx High Voltage Institute at Brunswick Technical University, Werner Koch, in 1967 as stated in [22]. The name of XRAM is the backward spelling of the high voltage generation device “MARX”. MARX generators are discussed in [23]. Circuit configuration of XRAM topology is given in Fig. 1.13.

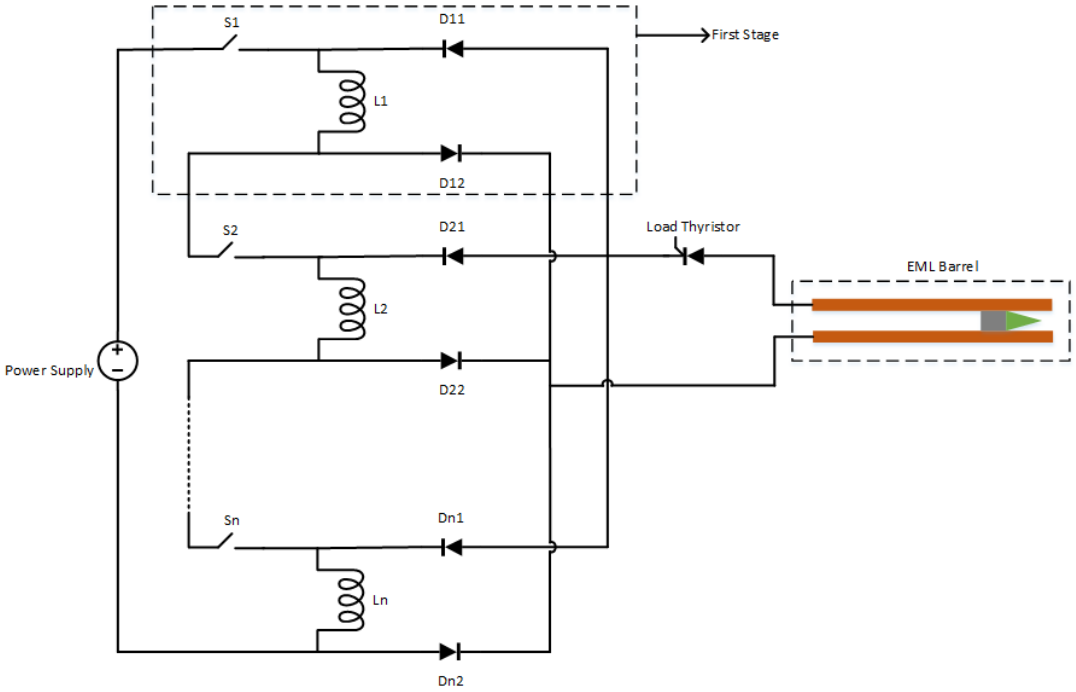

Figure 1.13: Generating pulsed power using n-stage XRAM.

Working principle of two stage XRAM generator is discussed in [24], while the design of a the XRAM with additional stages explained in detail in [25]. When "S" switches in Fig. 1.13 are closed and the load thyristor is not triggered, feeding power supply charges the inductors. Then, when "S" switches are opened and the load thyristor triggered, diodes conduct and inductors discharge through the EML.

To sum up, Although capacitive pulsed power supplies are the most common circuit topologies used in the EMLs, inductive pulsed power supplies are attractive because

of their high energy density, low charging voltage and short charging time.

1.4.3 Pulsed Alternator

Another way to generate pulsed power for EML excitation is pulse alternator-based power systems. Pulsed alternators use the stored inertial energy to generate electrical pulse power, [26]. In order to provide desired mechanical stored energy, rotor of the alternator is accelerated by a motor which is attached to the alternator shaft. The schema of air core pulsed alternator is given in Fig. 1.14, [27].

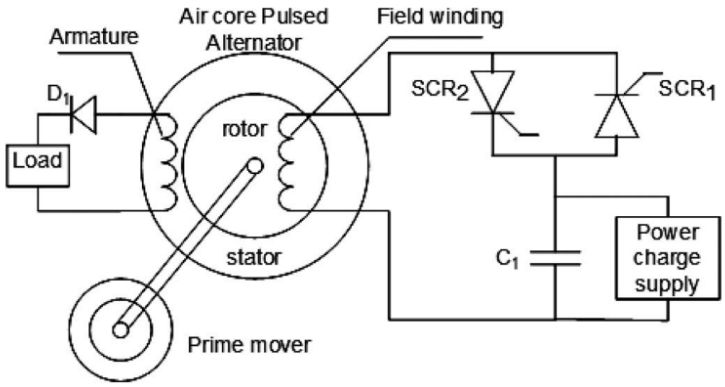

Figure 1.14: Schema of air core pulsed alternator, [27].

In Fig. 1.14, air core pulsed alternator is driven by prime mover with desired speed. C_1 is a pulse capacitor. It can be charged both in forward and reverse directions. While the prime mover drives the alternator, SCR_1 conducts to discharge the capacitor through field winding. After the capacitor is totally discharged, it charges by the field armature in the reverse direction. In the meanwhile, a pulsed current is induced in the armature winding. This pulse current excites the load which is an EML in our case. After the field and armature winding currents become zero, a new pulsed current can be induced in the armature winding by conducting SCR_2. Using this topology, repeated current pulses can be obtained on the load which is not possible with other topologies. Field and armature currents and capacitor voltage waveforms obtained with pulsed alternator is given in Fig. 1.15, [27].

In addition, to get large muzzle energy, required alternator size increases to store

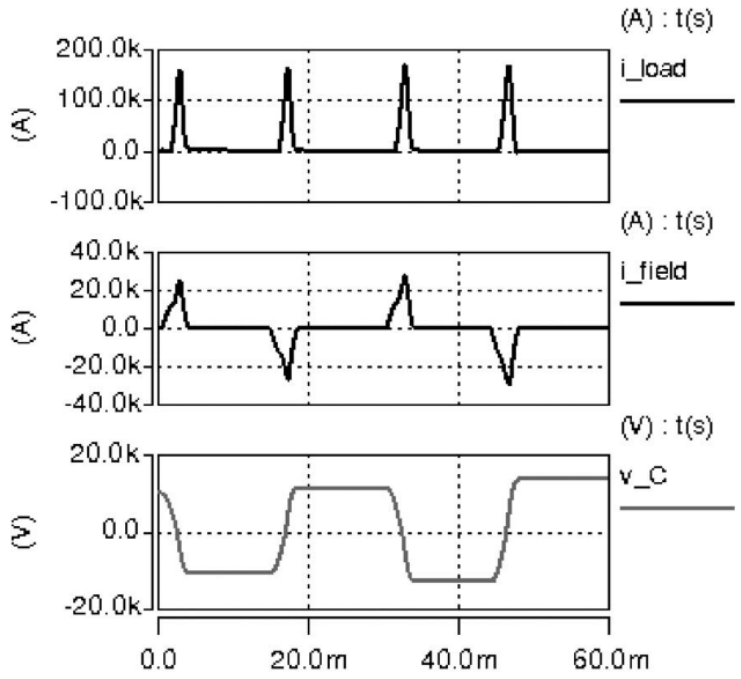

Figure 1.15: Winding currents and capacitor voltage waveforms of pulsed alternator, [27].

enough inertial energy in the rotor. Therefore, modular pulsed alternator power systems are more reliable than using single alternator for EML supply. Cui *et al.* make a review of modular pulsed alternator power systems to drive EMLs in [28]. Cui's proposed operation scheme of a pair of pulsed alternators power system in [28] is given in Fig 1.16.

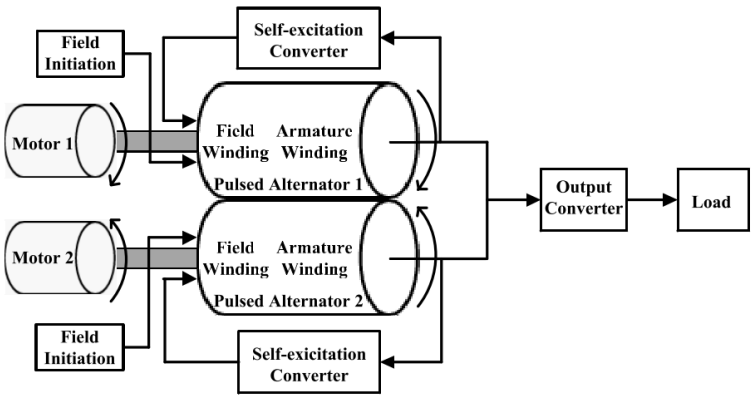

Figure 1.16: Operation scheme of a pair of pulsed alternators power system, [28].

To sum up, although it is possible to generate repeated current pulses on the load

using pulsed alternators, excitation losses limit the magnitude of field current of the pulsed alternators, [27]. Therefore capacitor based PPS topology is used more than pulsed alternators for the excitation of EMLs.

1.5 Challenges on the Barrel Side

Although the pulsed power generation circuit topologies are investigated in detail and certain topologies are used in the EML application, in the barrel side, there exit many challenges which are not still investigated and documented completely. In this thesis, challenges on the barrel side will be analyzed using finite element method (FEM) to design an efficient EML.

1.5.1 Type of Armature

In the literature, three types of armatures are used: solid armature, brushed armature and plasma armature.

The C-shaped solid armatures are the most common armature type. In [29], Chen *et al.* do some experiments to analyze the contact zone of their solid armature. In Fig. 1.17(a), the view of the solid armature used in Chen's experiments is given.

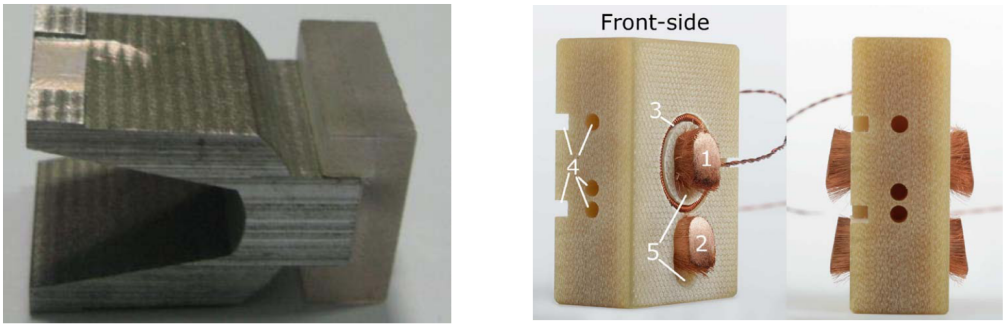

(a) Chen's experiment solid armature.

(b) ISL's brushed armature.

Figure 1.17: Solid and brushed armatures, [29] and [30].

In the brushed armatures, brushes provide improved electrical contact between the rails and armature. The view of the brushed armature developed in ISL is given

in Fig. 1.17(b), [30]. Since, the current path during the excitation is shorter for the brushed armatures, with using brushes for the electrical contact transition, ohmic losses caused by the armature can be decreased. However, C-shaped solid armatures provide lower friction than the brushed armatures. In [31], a comparison of C-shaped and brushed armature is investigated. It is concluded that the projectiles with C-shaped solid armatures convert the electrical energy into kinetic energy better than the projectiles with brushed armatures.

The last armature type is the plasma armature. Plasma is defined as fourth state of matter. A gas can be ionized under high temperature, large electric field, illumination by X-ray or bombardment with energetic charged particles. An ionized gas is called plasma. Scientists started working on using plasma as armature of an EML in 1980s. Marshall explain his experiments of an EML with plasma armature in [32]. Marshall's proposed structure for plasma armature EML is given in Fig. 1.18. Although the conductivity of plasma is much higher than the solid conductors, properties of plasma is quite complex. Moreover, these armatures may damage the rails during the current conduction via arcs. Therefore, solid and brushed armatures are used mostly in the today's EML technology.

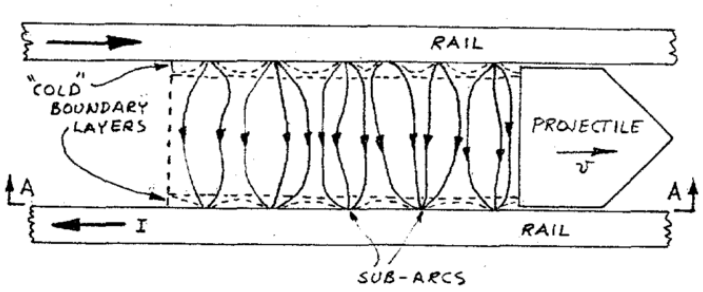

Figure 1.18: Structure of plasma armature EML, [32].

1.5.2 Rail Geometry

In the literature, there exist several studies about the influence of rail geometry on the efficiency of EMLs, [33–35]. Rectangular and round barrel cross sections are two main types of rail geometry. The schema of these two rail geometries are given in Fig. 1.19.

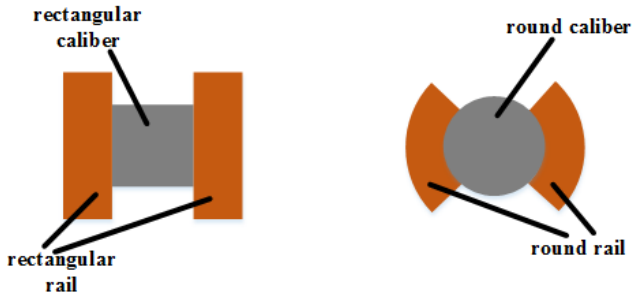

Figure 1.19: Rectangular and round barrel cross sections.

The investigations show that for the round barrel, the current density on the contact surface between rail and armature is smaller than for the rectangular barrel. However, the electromagnetic force acting on the armature of rectangular barrel is larger than the force acting on the armature of round barrel.

1.5.3 Structural Containment

As shown in Fig. 1.3, in addition to the propulsive force acting on the armature, a deflection force is created on the rails during the excitation. Because of this force, the rails repel each other and are deflected during the firing. In order to mechanically support the rails, using metal containment around the rails is a widely used method in railguns as investigated in [36] and [37].

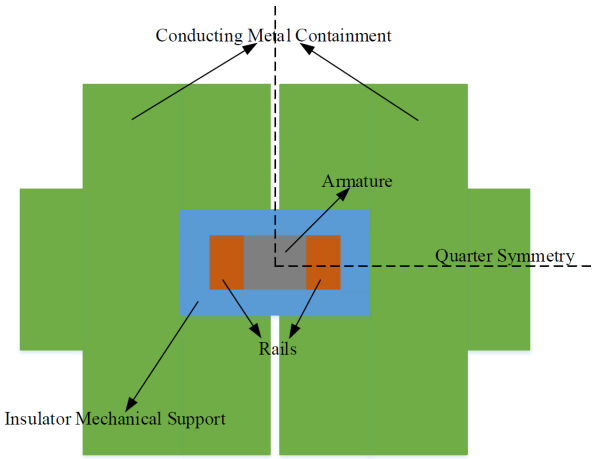

Figure 1.20: Sectional view of laminated containment model.

Containment must be used in EMLs in terms of mechanical requirements. However, due to the eddy current losses in the containment, the efficiency decreases. To solve the efficiency reduction problem, laminated containments are used in EMLs instead of the solid ones. Distance between the containment and the rails and the lamination thickness is two main parameters to design a containment for an EML to support the rails mechanically. In Fig. 1.20, an example of the cross section of a laminated containment is given. In [38], laminated containments are discussed in detail by us, which will be presented in detail in Section 4.1.

1.5.4 Recoil Force

In addition to the propulsive force acting on the armature and deflection force acting on the rails, there exist a recoil force acting on the busbars at the breech side of the barrel due to the conservation of momentum in reverse of the shot direction. Recoil forces are shown in schema of an EML in Fig. 1.21.

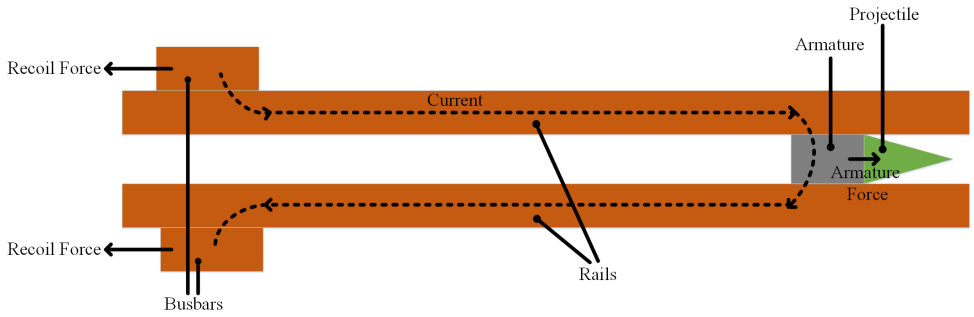

Figure 1.21: Electromagnetic recoil forces on the busbars.

Since the calculation of recoil force is critical in the design of busbars, it is thoroughly investigated in the literature. Kathe makes a review about the recoil considerations for EMLs in [39]. Also, Sadedin discusses the recoil concept in [40] analytically. While analytical solution to the launch momentum is discussed in both studies, Schneider *et al.* investigate the exact position where the recoil forces are created and the mechanical stress due to the recoil. In Section 3.6, busbars and coaxial cables are modeled using FEM. Then, the total recoil force and recoil force density distribution in the busbars and cables are presented.

1.5.5 Inductance and Resistance Estimation of Rails and Armature

From the electrical point of view, the barrel side of an EML can be modeled as series connected variable resistance and inductance as in Fig. 1.22. In Fig. 1.22, L_{EML} is the total inductance of rails and armature, R_{EML} is the total resistance of rails and armature, x is the position of the armature, v is the velocity of the armature, f is the frequency of the excitation current, F_{cont} is the contact force between one rail and armature.

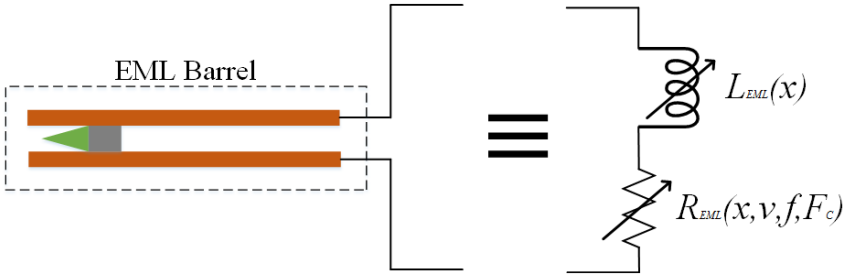

Figure 1.22: Barrel side of an EML can be modeled as series connected variable resistance and inductance.

The inductances of rails and armature only depend on the position of armature and the geometry of the rails and armature in the case of neglecting the effect of containment. The change of the barrel inductance is approximately linear with respect to the position of armature as in Eq. (1.9). In Eq. (1.9), L' is the change of inductance with respect to the armature position also called inductance gradient as explained in [41]. Inductance gradient of an EML only depends on height and thickness of the rail and caliber. Therefore the inductance gradient is constant for an EML. The calculation of the inductance gradient will be discussed in Section 3.3.

$$L_{EML} = L' * x \quad \text{where} \quad L' = \frac{dL_{EML}}{dx} \tag{1.9}$$

The calculation of the barrel resistance is more complex than the calculation of the barrel inductance. The resistance of the barrel of an EML consists of four components: alternating current (AC) resistance, velocity skin effect (VSE) resistance,

contact resistance and back electromotive force (EMF) resistance as in Eq. (1.10).

$$R_{EML} = R_{AC}(x, f) + R_{VSE}(x, v) + R_c(F_c) + R_{backEMF}(v, L') \tag{1.10}$$

AC resistance, R_{AC}, depends on the position of armature and the frequency of excitation current. VSE resistance, R_{VSE}, depends on the position and velocity of armature. Contact resistance, R_c depends on the contact force between rail and armature. Moreover, back EMF resistance, $R_{back\,EMF}$, depends on the velocity of armature and inductance gradient. These four components will be investigated in detail in Section 2.2.

1.5.6 Contact Transition between Rails and Armature

Analysis of electrical contact transition between two different materials in electrical circuits is a challenging problem. The main subject associated with the contact transition is the pressure dependency of contact resistivity as explained in detail in [42]. In EMLs, as the electromagnetic pressure on the armature-rail contact is not uniformly distributed, anisotropic contact resistance of the contact surface affects the current distribution which may melt the aluminum material of the armature. In addition to the melting effect of the contact transition, it creates an extra resistance which is formalized as in Eq. (1.11), [43].

$$R_c = \frac{k_c}{h}\sqrt{\frac{\mu\rho}{2\pi t}} \tag{1.11}$$

In Eq. (1.11), k_c is contact resistance constant, h is the height of the rail, μ is the permeability of the rail material and ρ is the effective resistance. Effect of contact transition on the contact current distribution and the resistive loss due to the contact resistance will be discussed in detail in Section 2.2.3.

1.5.7 Estimation of Current Density Distribution in the Rails

The analysis of current density distribution in the rails and armature is complex due to skin and proximity effects. Since pulse waveform of the excitation current has different frequency components, current density is largest near the surface of the conductor which is called skin effect. Well-known skin depth equation is given in Eq. (1.12) where δ is skin depth, ρ is the resistivity of the material, f is the frequency and μ is permeability.

$$\delta = \sqrt{\frac{\rho}{\pi f \mu}} \tag{1.12}$$

For larger frequencies, the current flows through the smaller skin depth which means the larger barrel resistance. Although the skin effect resistance is a well-known concept, the calculation of AC resistance of the rails and armature is not easy with analytical methods because of the proximity effect. Proximity effect is a current concentrating due to the one or more other nearby conductor. In the EMLs, magnetic field due to the one rail affects the current distribution in the other rail. Therefore, the current density on the inner surfaces of the rails is larger than their outer surfaces.

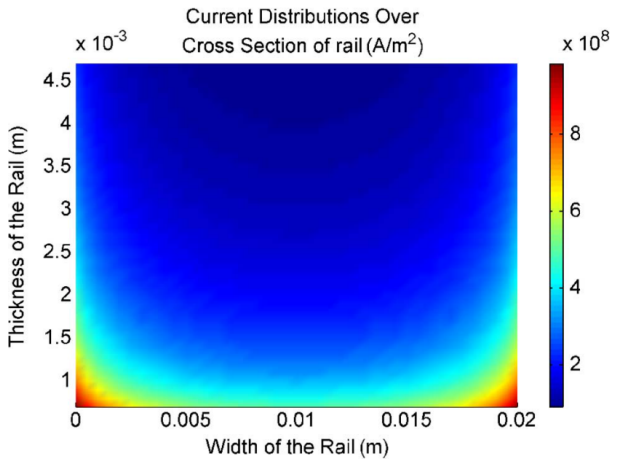

Figure 1.23: Current density distribution over the cross section of one rail, [44].

In [44], current distribution over the cross section of rectangular rail is calculated using FEM, see Fig 1.23. It can be observed that most of the current flows through the surface of the rail due to the skin effect. In addition, the current density is larger

on the contact surface, where the value of thickness (Y axis) in Fig 1.23 is zero, than the other rail surfaces due to the proximity effect.

The defined problems in the barrel side will be investigated in Chapter 2 to develop a realistic FE model of the EML. Moreover, In Chapter 3, results of the FE model will be presented with the change of barrel resistances, current density and magnetic field distributions and electromagnetic forces during the excitation. Kinematic calculations, thermal analysis and recoil force calculations will also investigated in Chapter 3. After the discussion on the results of FE simulation, the optimization study for the lamination of containment and armature geometry will be presented in Chapter 4. Finally, the thesis will be concluded in Chapter 5.

CHAPTER 2

FINITE ELEMENT MODELING OF THE ELECTROMAGNETIC LAUNCHER

In this chapter, the development of a realistic finite element (FE) model to simulate the proposed EML will be discussed. COMSOL Multiphysics is used as the simulation software. In the FE model, the armature is stationary at the position of preload: $x_{preload}$, which is the armature position after loading the armature mechanically between the rails and before the excitation, determined as 0.3 m from the experiments.

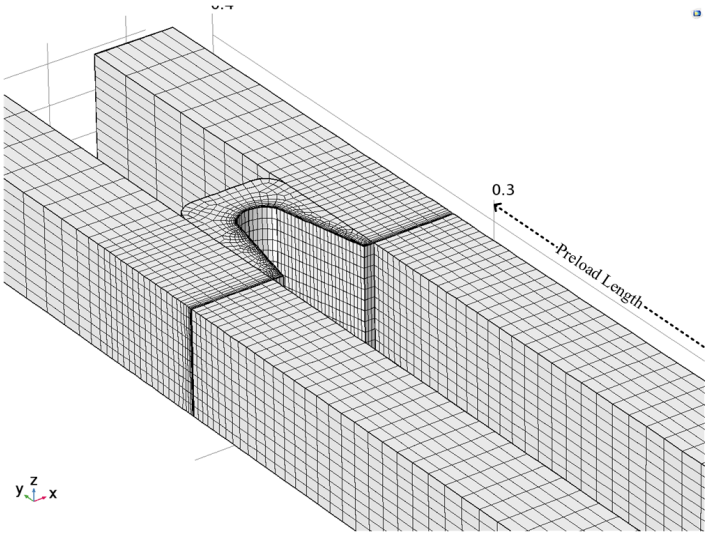

Figure 2.1: Mesh structure of rails and armature.

In Fig. 2.1, mesh structure of the rails and armature are given together. In Fig. 2.2, mesh structures of the armature and the cross section of the rails are given. In the rails and armature hexagonal mesh elements are used. Since the armature is stationary at preload position, it is enough to use only 0.4 m long rails in order to decrease the number of the mesh elements. The FEA model consists of 260194 domain elements,

22542 boundary elements, and 1356 edge elements. In addition to the hexagonal mesh elements, boundary layers are used in the inner surface of the armature and the outer surfaces of the rails to observe the skin depth right.

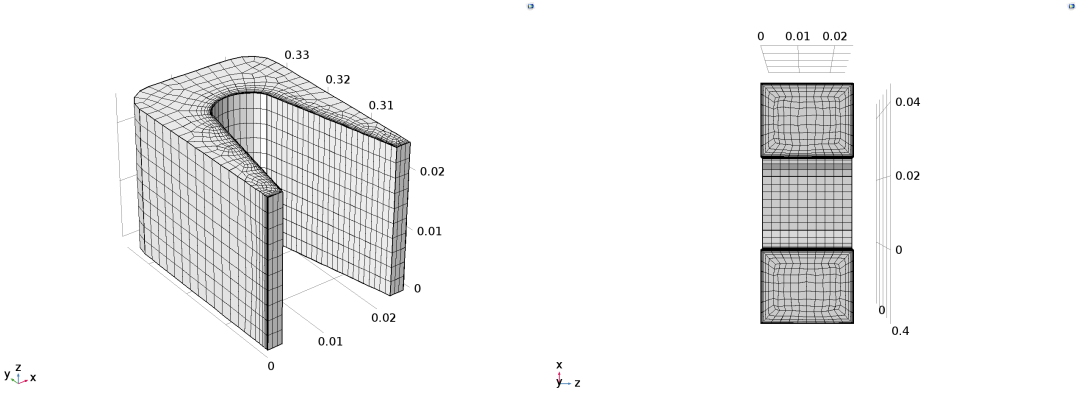

(a) (b)

Figure 2.2: Mesh structure of the armature and the cross section of the rails.

In addition, symmetry is a critical issue to decrease the computational cost of the model. EMLs intrinsically have two symmetry axises as shown in Fig 2.3

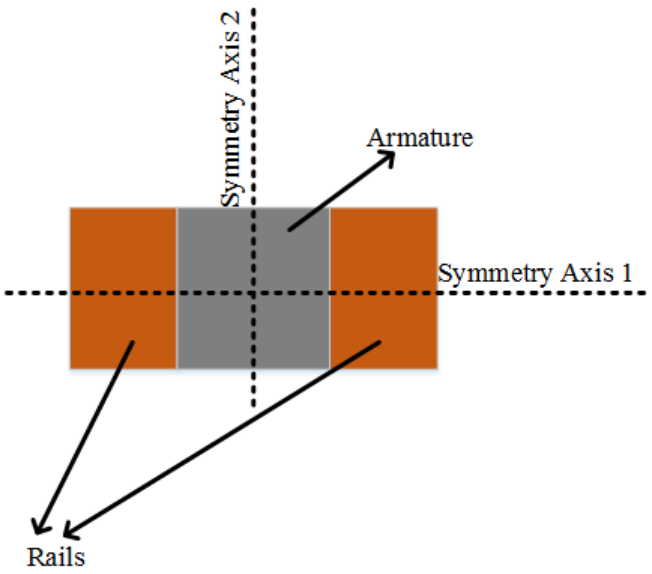

Figure 2.3: Symmetry axises of an EML.

While the current density vectors are parallel to the symmetry axis 1, the magnetic flux density vectors are perpendicular to it. Moreover, while the current density vec-

tors are perpendicular to the symmetry axis 2, the magnetic flux density vectors are parallel to it. Therefore it is enough to solve only one quarter of the FE model. In Fig. 2.4, only one quarter of the EML used in the study is given with the same mesh settings stated previously.

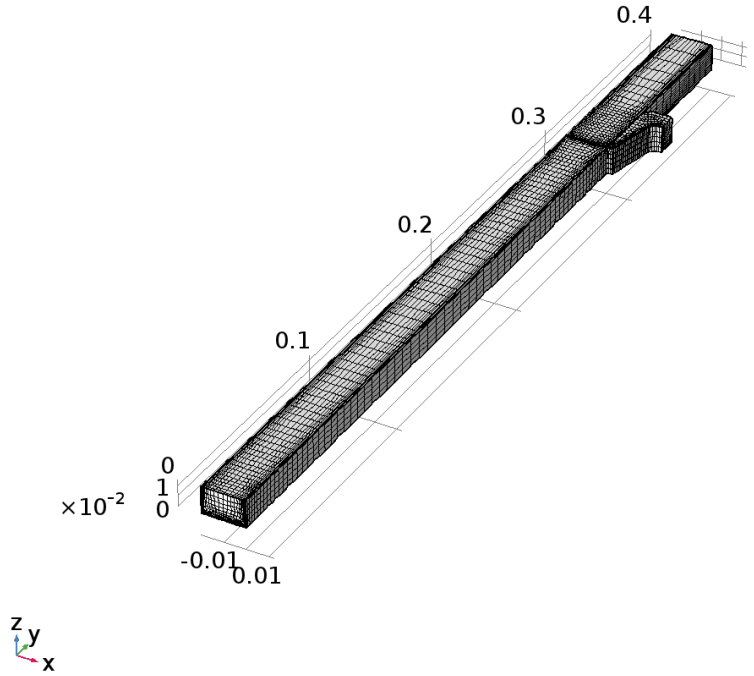

Figure 2.4: One quarter of the EML.

Although the symmetry property of the EML is used in the analysis to decrease the computational cost, in the next parts of the study, results are presented for the full geometry.

Moreover, since the 3D moving mesh approach is very challenging for EMLs due to its computational cost, a stationary FE model emulating the armature movement with variable barrel resistance and inductance is developed in this study. The schema of stationary FE model with its feedbacks is given in Fig. 2.5. As the EML's current is influenced by the variation of electrical parameters in the barrel side, capacitor based PPS is integrated into the FE model as in Fig. 2.5 where I_{EML} is EML current, V_{breech} is breech voltage and f is the frequency of the pulse shaped I_{EML}. In addition, the

variable resistances in the barrel side are AC resistance: $R_{ac}(x,f)$ which depends on armature displacement and current frequency, VSE resistance of the rails: $R_{vse\ rail}(x,v)$ which depends on the armature displacement and velocity, velocity skin effect resistance of the armature: $R_{vse\ arm}(v)$ which depends on the armature velocity, back emf resistance of the barrel due to the change of barrel inductance with respect to time: $R_{back\ emf}(v)$ which depends on the armature velocity. Moreover, the variable barrel inductance is represented as L(x) which depends only on the armature displacement.

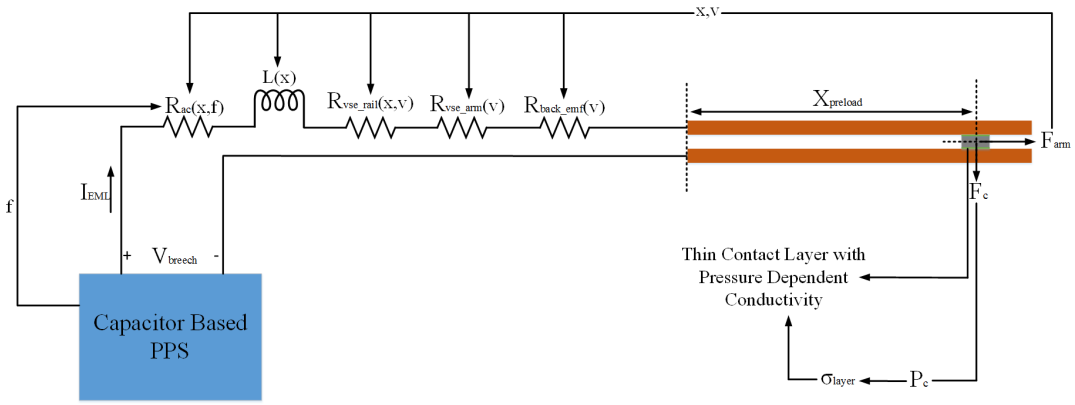

Figure 2.5: Schema of closed loop FE model to simulate the armature movement with stationary mesh elements.

Although during the computation of time dependent solver of FEM software, COMSOL Multiphysics, armature stays at $x_{preload}$, armature displacement: x and armature velocity: v are calculated as in Fig. 2.5. Then, to emulate the armature movement, the variable resistances and inductance are updated using x and v parameters. It is critical to note that the initial values of v and x are both zero. In addition, F_{arm} and F_c are the propulsive electromagnetic force acting on the armature in the acceleration direction and the electromagnetic contact force between the rails and armature, respectively. Thin contact layers with pressure dependent conductivities are placed between the rails and armature to take the contact resistance into account. The conductivities of the thin layers change with contact pressure: P_c. The calculation of barrel resistances and inductance will be discussed in the next sections of this chapter.

2.1 Pulsed Power Supply

As explained in Chapter 1, capacitor based PPS units are used to excite the barrel in this study. The topology of one short circuited PPS unit is given in Fig. 2.6. Also, the values of electrical parameters of this circuit are given in Table 1.2.

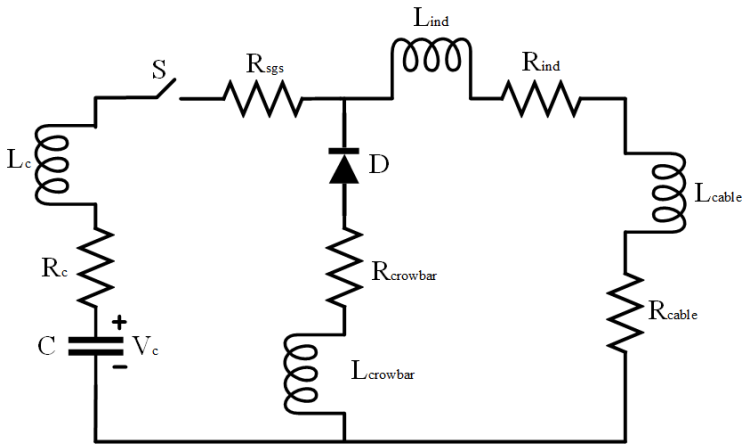

Figure 2.6: Topology of single short circuited PPS unit.

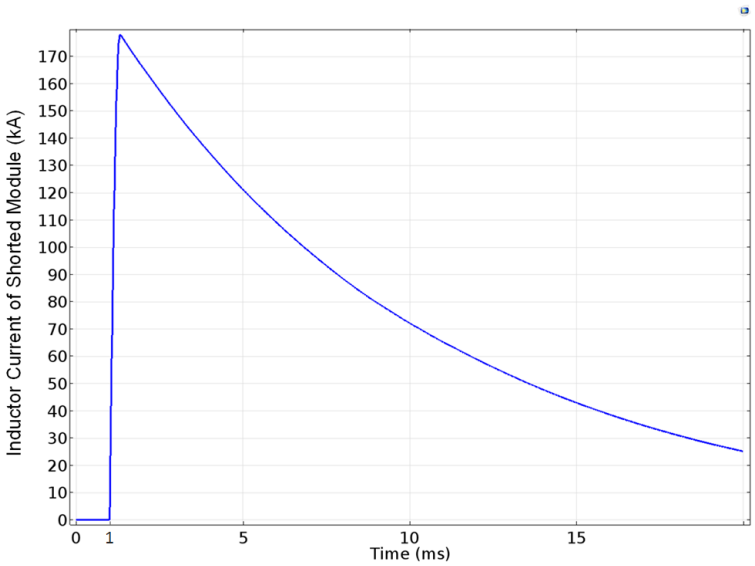

Figure 2.7: Pulse shaping inductor (L_{ind}) current with only single module firing without barrel.

In Fig 2.7, the current waveform through the pulse shaping inductor is given for the switching of one short circuited PPS unit at 1 ms. While the current rising takes 0.3 ms, the current falling takes approximately 40 ms. Moreover, the peak value of

pulse shaped current is 178 kA.

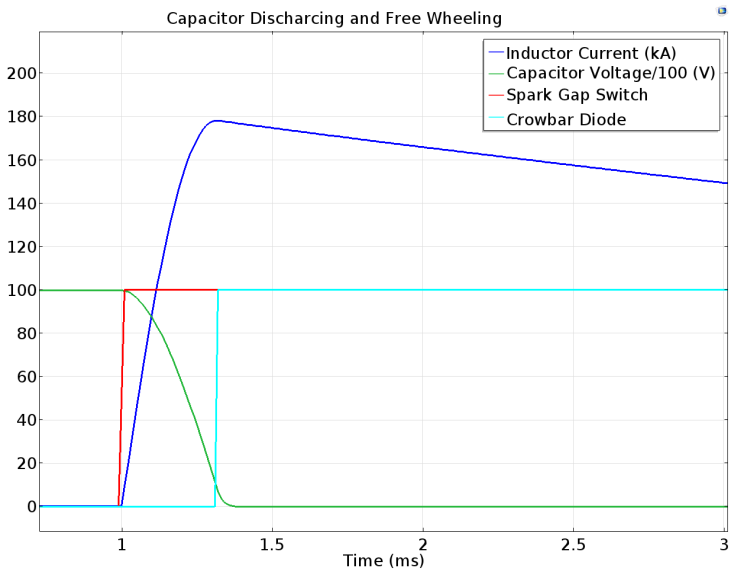

Figure 2.8: Inductor current, capacitor voltage and switching of semiconductors.

As shown in Fig. 2.8, after the switch conducts, capacitor with 10 kV initial voltage starts discharging through pulse shaping inductor. Therefore, during the capacitor discharging time interval, inductor current rises. When the capacitor is fully discharged, diode starts conducting. Then, the inductor starts to discharging through diode. During this time interval, inductor current decays.

In the PPS of the designed EML, there are 10 identical units connected in parallel. The switching sequence of these units determines the waveform of the short circuit current. The purpose is to keep the total current magnitude at its peak value as long as possible. Switching times of each PPS module which create a short circuit current with 1 MA peak are given in Table 2.1.

In Fig. 2.9, the waveform of total short circuit current for the given switching sequence is available. Its average peak value is approximately 1 MA.

It should be noted that if the barrel is attached to the PPS instead of shorting it, the peak value and the rising and falling times of the PPS currents alter, as will be shown later.

Table 2.1: Switching times of PPS modules to get short circuit current with 1 MA peak.

Module 1-6	0 ms
Module 7	1.6 ms
Module 8	3.2 ms
Module 9	4.8 ms
Module 10	6.4 ms

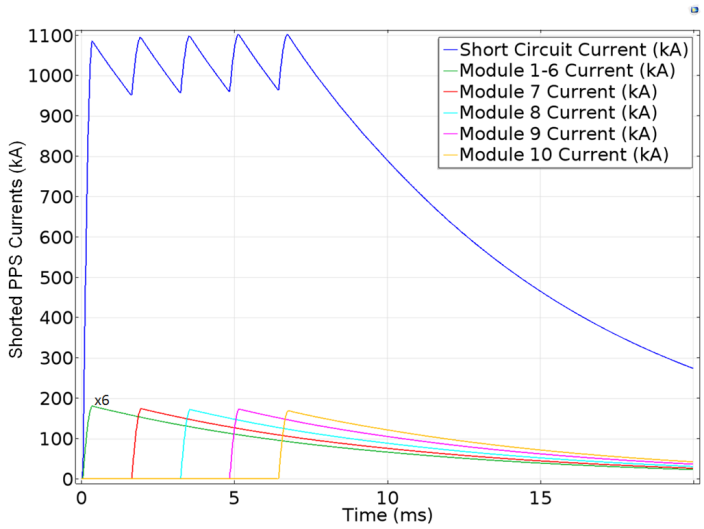

Figure 2.9: Short circuit current and module currents for 1 MA peak value scenario.

2.2 Barrel Resistance Estimation

In this section, calculation of AC resistance of the rails and armature, velocity skin effect (VSE) resistance, contact resistance and power loss due to the induced EMF will be presented.

2.2.1 AC Resistance of Rails and Armature

Direct current (DC) resistance of the barrel depends on the geometry and resistivity of rails and armature and the position of the armature. In Eq. (2.1), the total DC resistance of the rails is given where ρ_{rail} is the resistance of copper material of the

rails, x is position of the armature, h is height of the rails and w is thickness of the rails. Since current flows through two rails, it is necessary to multiply the equation by 2 to get total length of the rails.

$$R_{\mathrm{DC_{rails}}}(x) = 2\,\frac{\rho_{\mathrm{rail}}\,x}{h\,w} \tag{2.1}$$

In order to get rid of the dependency of armature position, $\mathrm{R'_{DC_{rail}}}$ can be defined as the resistance of the rails per meter (Ω/m).

$$R_{\mathrm{DC_{rails}}}(x=1) \;= R'_{\mathrm{DC_{rails}}} = 2\,\frac{\rho_{\mathrm{rail}}\,1}{h\,w} = 2\,\frac{1.67\,10^{-8}\,1}{0.025\,0.02} = 0.067\;m\Omega/m \tag{2.2}$$

DC resistance of the armature may be approximated as in Eq. (2.3) where ρ_{arm} is the resistance of the aluminum material of the armature, c is the caliber, l_{arm} is the length of the armature in the acceleration direction (y-direction in the model).

$$R_{\mathrm{DC_{arm}}} = \frac{\rho_{\mathrm{arm}}\,c}{h\,l_{\mathrm{arm}}} = \frac{2.65\,10^{-8}\,0.025}{0.02\,0.036} = 0.00073\;m\Omega \tag{2.3}$$

DC resistance of the barrel for the 1 m armature position is equal to the summation of armature and rail DC resistances as in Eq. (2.4).

$$R'_{\mathrm{DC}} = R'_{\mathrm{DC_{rails}}} + R_{\mathrm{DC_{arm}}} \approx R'_{\mathrm{DC_{rails}}} = 0.067\;m\Omega/m \tag{2.4}$$

In order to calculate $\mathrm{R'_{DC}}$, described FE model is excited with 1 kA DC current. The current density distribution in the rails and armature is given in Fig. 2.10.

In Eq. (2.5), the resistive power loss in the rails and armature is found by the volume integration of the multiplication of conductivity and the square of normalized current density.

$$P_{\mathrm{loss}} = \oint_{rail}\left(\rho_{\mathrm{rail}}\left(\sqrt{J_x^2+J_y^2+J_z^2}\,\right)^2\right)dV + \oint_{arm}\left(\rho_{\mathrm{arm}}\left(\sqrt{J_x^2+J_y^2+J_z^2}\right)^2\right)dV \tag{2.5}$$

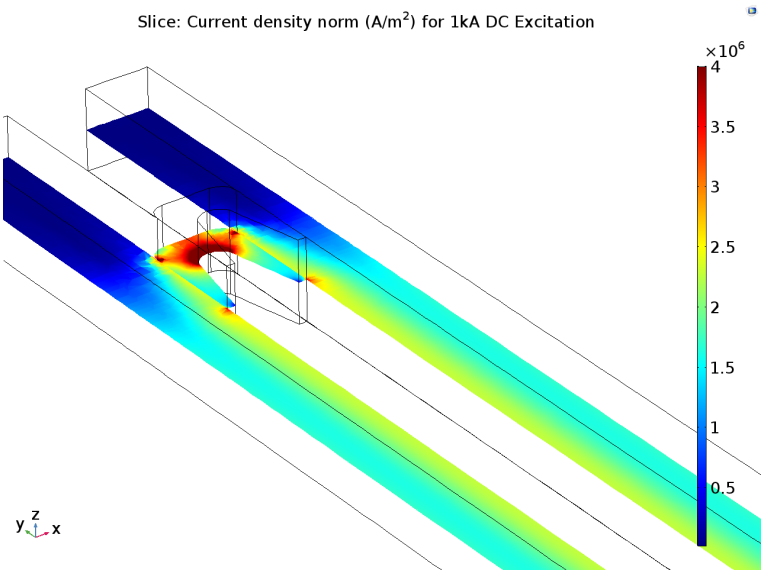

Figure 2.10: Current density distribution in the rails and armature for 1 kA DC current excitation.

In the FE model, the equivalent DC resistance per meter can be found using Eq. (2.6) when the armature is positioned at 1 m.

$$R'_{\mathrm{DC}} = \frac{P'_{\mathrm{loss}}}{I^2_{\mathrm{EML}}} \tag{2.6}$$

Using Eq. (2.5) and (2.6), DC resistances of the rails and the armature are calculated as 0.08 $m\Omega$ and 0.0025 $m\Omega$ using the FE model, respectively. Since the barrel is excited by DC current, skin effect resistance is not considered in this model. However, unlike the analytical calculations, this model takes the proximity effect and non-uniform distribution of the current density into account during the resistance calculation.

It is significant to note that the excitation current of the PPS has varying frequency components. Hence, it is not possible to mention a DC resistance during the firing of an EML. Therefore, for a realistic approximation, the information of frequency has to be calculated in the PPS side to be used in the the barrel side for each time step.

In order to calculate the AC resistance of the rails and armature, a FE model with frequency domain solution is used at varying frequencies. In Fig. 2.11, current density

distribution in the rails and armature are given for 50 Hz and 1 kHz cases.

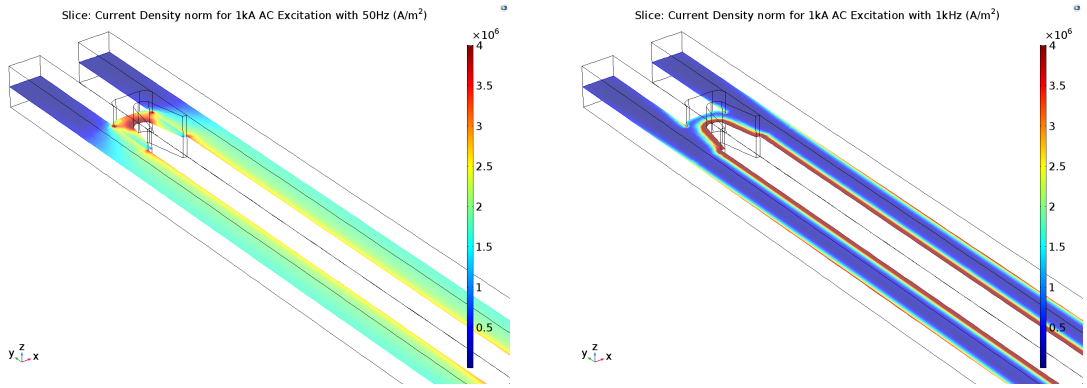

(a) 50 Hz AC excitation (b) 1 kHz AC excitation

Figure 2.11: Current density distribution in the rails and armature for 1kA AC current excitation with 50 Hz and 1 kHz.

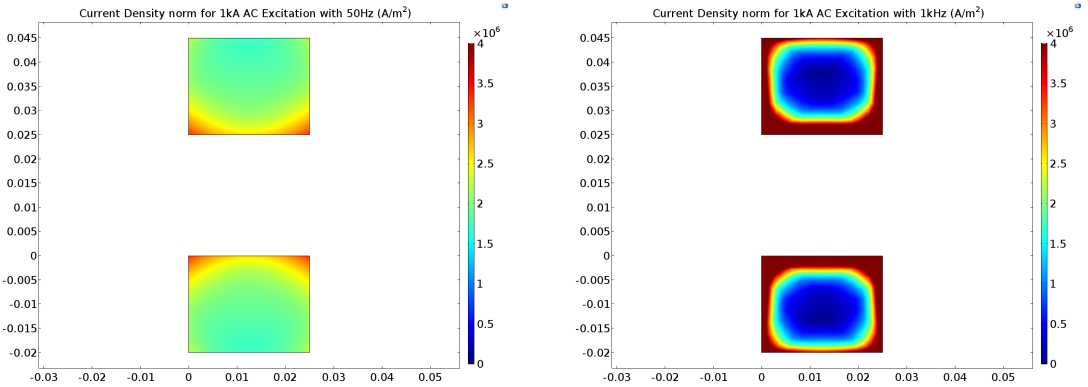

(a) 50 Hz AC excitation (b) 1 kHz AC excitation

Figure 2.12: Current density distribution on the cross-section of rails for 1kA AC current excitation with 50 Hz and 1 kHz.

In Fig. 2.12, skin depths on the cross-section of the rails are given for 50 Hz and 1 kHz cases. It can be observed that effective area of the rail cross section where current flows decreases with large current frequencies which is called skin effect. Hence, for the 50 Hz case in Fig. 2.12, the current is distributed more uniformly in the rails than for the 1 kHz case. Moreover, it can be seen that the current density around the contact surfaces of the rails is larger than the other surfaces due to the proximity effect.

AC resistance of the rails and armature can be calculated for different excitation current frequencies using the current distribution given in Fig. 2.11 and 2.12; and the resistance calculation approach given in Eq. (2.5) and (2.6). In Fig. 2.13, the change of AC resistance of the rails and armature with respect to the frequency is given for 1 m armature position.

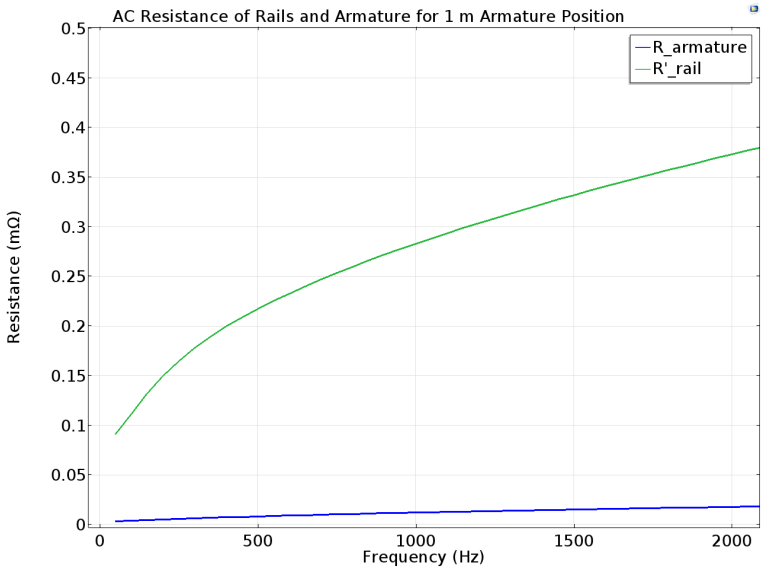

Figure 2.13: AC resistance of the rails and armature with respect to the excitation current frequency.

Fig. 2.13 shows that resistance of the rails and the armature increases with the increase of current frequency. Also, it can be stated that AC resistance of single rail is much larger than the AC resistance of the armature for any frequency value.

2.2.2 Velocity Skin Effect Resistance Modeling

In addition to the position of the armature, its velocity also affects the current distribution in the rails and armature. Hence, the resistance of an EML's barrel is not independent of armature velocity. This phenomenon is known as velocity related current clustering or known by name velocity skin effect (VSE). In Fig. 2.14, schema of the influence of VSE on the current path in the rails and armature is given. While in Fig. 2.14 (a), the armature is stationary or with low velocity, in (b), it has high velocity.

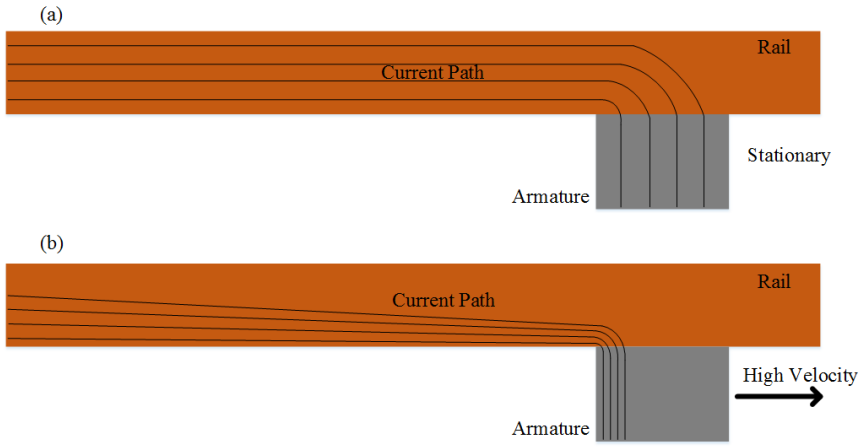

Figure 2.14: VSE changes the current path in the rails and armature: (a) Stationary armature, (b) High velocity armature.

In [45] and [46], Barber concluded that VSE may cause the local material of armature to melt, losing contact and discharge transition. Furthermore, the influence of VSE on the barrel resistance has been investigated by many researchers in the literature. In 1989, Barber and Marshall worked on an equation for the voltage drop along the rail due to VSE, [47]. They started with Eq. (2.7) where V is voltage drop along the rail from x=0 to $x=x_1$, x is armature position and j_r is surface current density along the rail.

$$V(x) = \int_0^{x_1} j_r(x)dx \tag{2.7}$$

It is critical to note that in their study, Barber and Marshall assume that while the current in the armature flows only perpendicular to the rail surface, the current flow in the rail is predominantly parallel to the rail. Moreover, in their equations, the armature velocity is constant during the armature transient time. Because of these assumptions, Barber and Marshall expressed the current density vectors in [47], as in Fig. 2.15.

Current density distribution in the rail can be expressed as in Eq. (2.8), if the previous assumptions are approved. Note that Eq. (2.8) must be integrated from $x_1=0$ to $x_1=x$

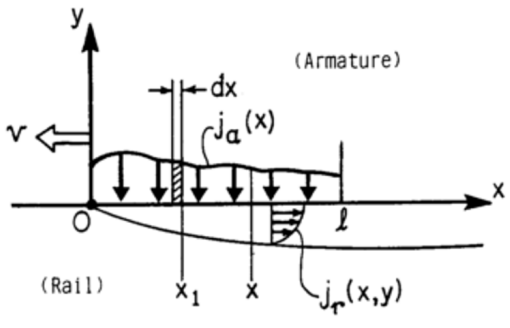

Figure 2.15: Barber's proposed current density distribution schema for VSE, [47].

which is the position of armature to find the total current at x.

$$j_r(x) = \int_0^x dj_r \tag{2.8}$$

According to the diffusion equation for magnetic flux, j_r diffuses into the rails as given in Eq. (2.9), where α is the current density reduction factor which is taken as 0.5 in [47], ρ_r is the resistivity of the rail material, μ_0 is the permeability of vacuum and t is elapse time since the armature point x_1 passed the rail point x.

$$dj_r = \frac{\alpha j_a(x_1)dx_1}{\sqrt{\frac{\pi\rho_r t}{\mu_0}}} \quad where \quad t = \frac{(x-x_1)}{v_c} \tag{2.9}$$

When Eq. (2.9) is substituted into Eq. (2.8), Eq. (2.10) can be observed with considering the constant velocity: v_c.

$$j_r(x) = \int_0^x \frac{\alpha j_a(x_1)dx_1}{\sqrt{\frac{\pi\rho_r(x-x_1)}{\mu_0 v_c}}} = \int_0^x \sqrt{\frac{\mu_0 v_c}{\pi\rho_r(x-x_1)}}\,\alpha j_a(x_1)dx_1 \tag{2.10}$$

When Eq. (2.10) is substituted into Eq. (2.7), Eq. (2.11) and (2.12) can be observed.

$$V(x) = \int_0^x \rho_r \int_0^{x_2} \sqrt{\frac{\mu_0 v_c}{\pi\rho_r}} \frac{\alpha j_a(x_1)}{\sqrt{x_2 - x_1}} dx_1 dx_2 \tag{2.11}$$

$$V(x) = \alpha\sqrt{\frac{\mu_0 v_c \rho_r}{\pi}} \int_0^x \left[\int_0^{x_2} \frac{j_a(x_1)dx_1}{\sqrt{x_2 - x_1}}\right] dx_2 \tag{2.12}$$

In, [48], Thurmond, Ahrens and Barber described the armature current density as in Eq. (2.13) according to their experimental results where h is the height of the rail as in Fig. 1.5, I is excitation current and $\delta(x_1)$ is a Dirac delta function at x_1=0.

$$j_a(x_1) = \frac{I}{h}\delta(x_1) \tag{2.13}$$

In Eq. (2.13), a Dirac delta function is used because it is also assumed that the current flows through only the back surface of the armature. After substituting Eq. (2.13) into Eq. (2.12) and integrate it, one can reach Eq. (2.14) and (2.15).

$$V(x) = \frac{I}{2h}\sqrt{\frac{\mu_0 v_c \rho_r}{\pi}}\,(\sqrt{x_2} - \sqrt{x_1}) \quad where \quad x_1 = 0 \; and \; x_2 = x \tag{2.14}$$

$$V(x) = \frac{I}{2h}\sqrt{\frac{\mu_0 \rho_r}{\pi}}\,\sqrt{x v_c} \tag{2.15}$$

Eq. (2.15) is a general formula for the voltage drop between the breech point and another point on the rail, x. Moreover, Engel *et al.* extend the study in, [49]. They did not consider the armature velocity constant for the VSE resistance calculation. They proposed a time constant for the armature movement: τ as in Eq. (2.16) where v_{max} is the maximum velocity that the armature can reach for a defined shot scenario, v is the instantaneous armature velocity for that shot and t is the time instant.

$$\tau = \frac{v_{max}}{v}t \tag{2.16}$$

The purpose of their study, in [49], is to get rid of the armature position dependency of the VSE resistance. Hence, in Eq. (2.17), the armature position is expressed as a function of τ, v_{max} and v.

$$x = \int v dt = \int \frac{v_{max}}{\tau} t dt = \frac{v_{max}}{2\tau}t^2 = \frac{v_{max}}{2\tau}(\frac{\tau v}{v_{max}})^2 = \frac{\tau}{2v_{max}}v^2 \tag{2.17}$$

After substituting Eq. (2.17) into Eq. (2.15), in Eq (2.18), it can be observed that

VSE resistance is proportional to VSE proportionality constant: K_{vse} and $v^{3/2}$.

$$R_{vse} = \frac{V}{I} = \frac{1}{2h}\frac{\sqrt{\mu_0\rho_r}}{\pi}\sqrt{\frac{\tau v^3}{2v_{max}}} = \frac{1}{2h}\frac{\sqrt{\mu_0\rho_r}}{\pi}\sqrt{\frac{\tau}{2v_{max}}}v^{3/2} = K_{vse}v^{3/2} \quad (2.18)$$

Eventually, [49] shows that, since VSE resistance is proportional to $v^{3/2}$, it is the dominant barrel resistance for large armature velocities. However, the calculation of K_{vse} is not very apparent. It was found experimentally in the literature with collector test rig experiment in [48]. In these experiments, the motor which turns the aluminum disk is capable of turning the disk at tip speeds up to 250 m/s. Moreover, the value of this constant varies from 2 10^{-9} to 7 10^{-9} in the literature. Although this analytical study ends up with a significant conclusion which is the fact that R_{vse} is proportional to the 2/3th power of the armature velocity, there exist many assumptions and empirical relations in it. Therefore, in this study, 2D FEM approach with moving mesh property is used to find a relation between armature position, velocity and R_{vse}. Mesh design of this model is given in Fig. 2.16.

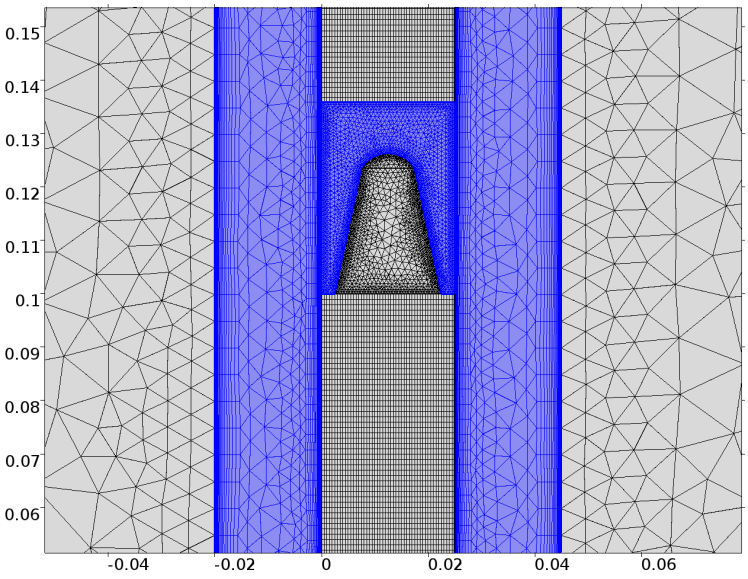

Figure 2.16: Mesh design of 2D moving geometry model.

In this model, to analyze the VSE resistance, armature moves with different constant speeds in the range between 10 m/s to 1000 m/s with 1kA DC current excitation. Then, the change of rail and armature resistances are investigated using the same

approach in 3D model which integrates the current density over the volume of rails and armature. The current distribution in the rail and armature for different velocities are given in Fig. 2.17 and 2.18, respectively.

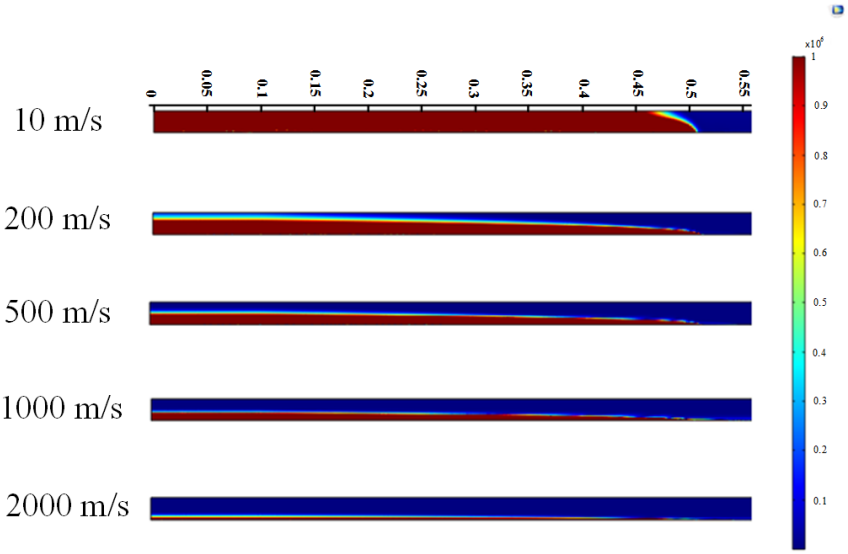

Figure 2.17: Current distribution in the rail for different velocities.

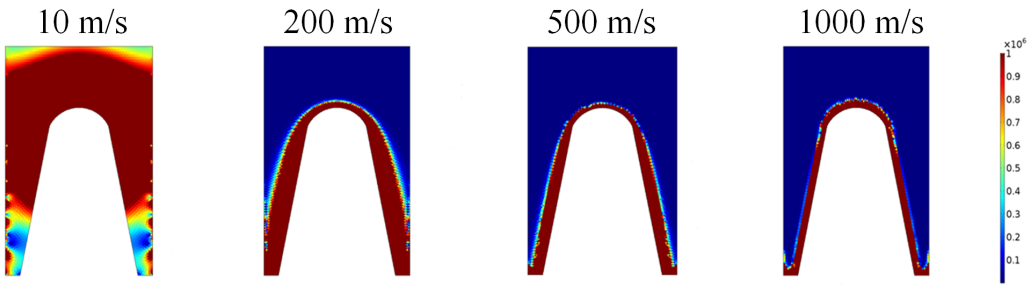

Figure 2.18: Current distribution in the armature for different velocities.

It can be observed that since the current concentrates in a small volume, the larger velocity means the smaller velocity skin depth which causes the greater VSE resistance.

After obtaining the current density distributions in the rails and armature for different constant velocities, resistances of rails and armature are calculated by integrating the current densities for these velocities. One significant inference of this study is that while the resistance of armature depends on only velocity, the resistance of rails

depends on both velocity and position as given in Eq. (2.19)

$$R_{total} = R_{rail}(x, v) + R_{arm}(v) \tag{2.19}$$

Resultant resistance values consist of 2 parts: DC resistances of rails and armature and VSE resistance as in Eq. (2.20).

$$R_{total} = R_{rail_{DC}}(x) + R_{rail_{vse}}(x, v) + R_{arm_{DC}} + R_{arm_{vse}}(v) \tag{2.20}$$

$R_{rail_{DC}}(x)$ is found in Section 2.2.1. Also, it was shown that $R_{arm_{DC}}$ is negligible. Therefore, Eq. (2.20) can be modified as in Eq. (2.21).

$$R_{total} \approx R'_{DC}x + R_{rail_{vse}}(x, v) + R_{arm_{vse}}(v) \tag{2.21}$$

In Fig. 2.19, the influence of armature velocity on the armature resistance is presented.

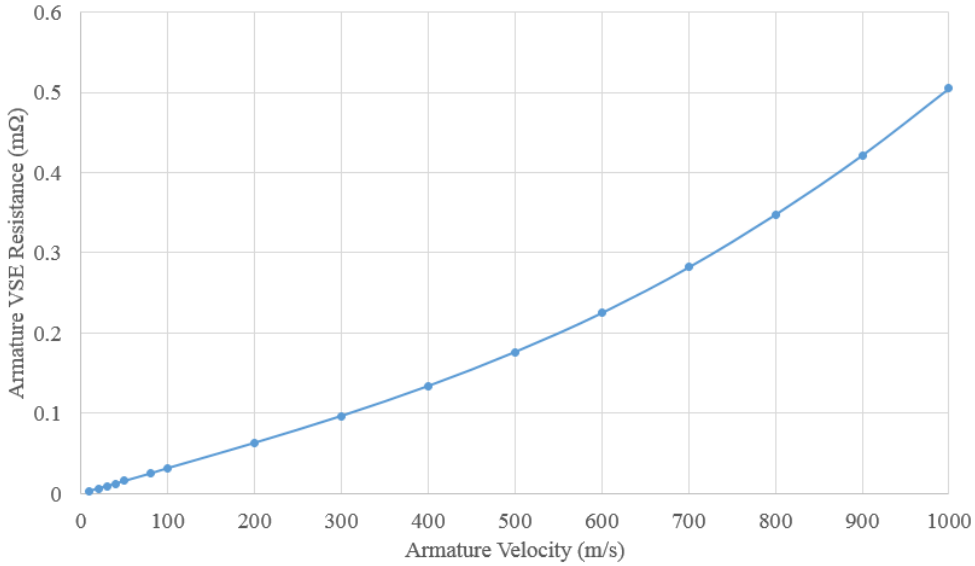

Figure 2.19: Change of armature VSE resistance with change of armature velocity.

As stated previously, $R_{rail_{vse}}$ is dependent both on armature velocity and position. In Fig. 2.20, the influence of armature velocity on total rail VSE resistance is given for

1 m armature position. Also, in this figure, constant $R_{rail_{DC}}$ for 1 m armature position is given for the comparison.

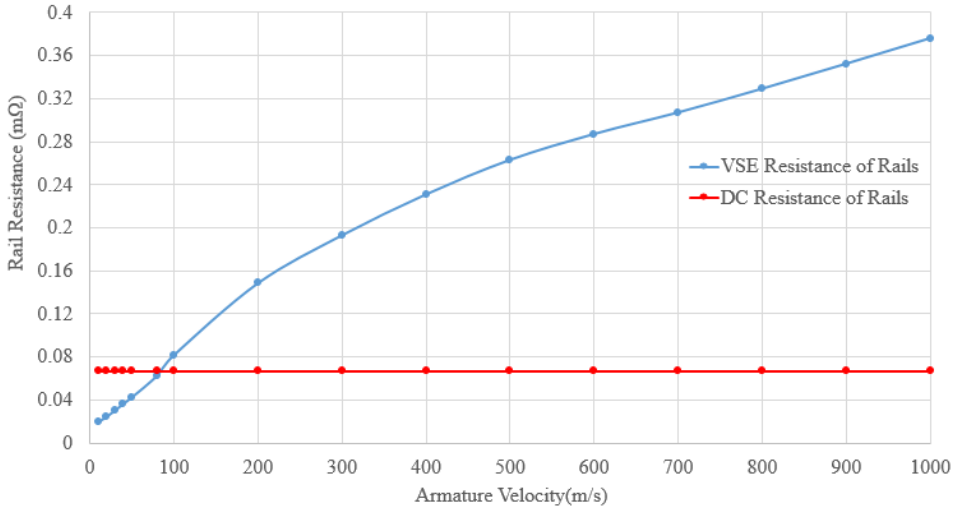

Figure 2.20: Change of total rail VSE resistance with armature velocity for 1 m armature position.

Moreover, it is observed that $R_{rail_{vse}}$ is linearly dependent of armature position. Therefore, $R_{arm_{vse}}$ and $R_{rail_{vse}}$ can be modeled as in Eq. (2.22) and (2.23).

$$R_{rail_{vse}}(x, v) = f_{rail_{slope}}(v)\, x + f_{rail_{offset}}(v) \tag{2.22}$$

$$R_{arm_{vse}}(v) = f_{arm}(v) \tag{2.23}$$

In these equations, $f_{rail_{slope}}$, $f_{rail_{offset}}$ and f_{arm} are velocity dependent functions. Then, polynomial fitting is implemented for these function in order to find an equation for each function as in Eq. (2.24) and (2.25).

$$R_{rail_{vse}}(x, v) = (k_{11}\, v^2 + k_{12}\, v + k_{13})\, x + (k_{21}\, v^2 + k_{22}\, v + k_{23}) \tag{2.24}$$

$$R_{arm_{vse}}(v) = k_{31}\, v^2 + k_{32}\, v + k_{33} \tag{2.25}$$

Coefficients in Eq. (2.24) and (2.25) cannot be given in this thesis due to the confidentiality agreement between ASELSAN Inc. and subcontractor in METU.

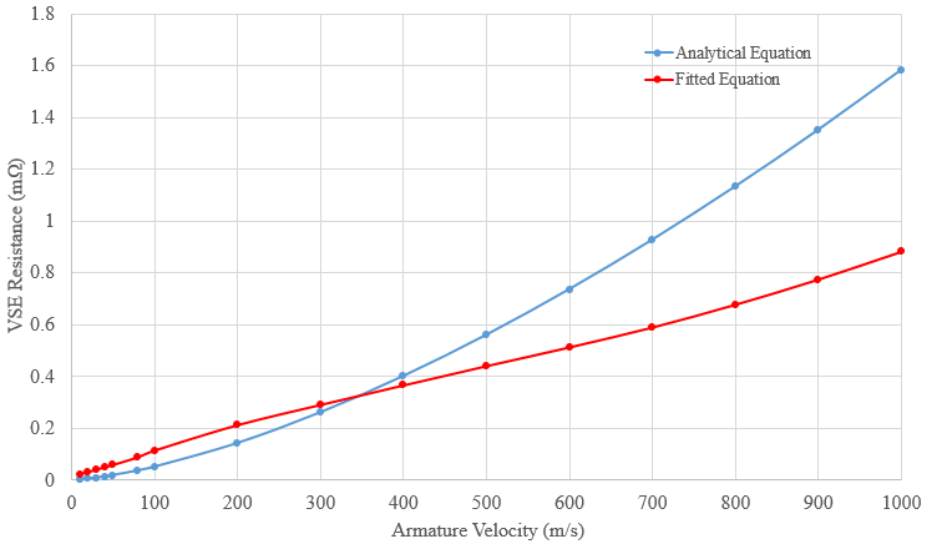

Figure 2.21: Comparison between analytical equation: $K_{vse}\, v^{3/2}$ and fitted equation: $R_{rail_{vse}}+R_{arm_{vse}}$ in Eq. (2.24) and (2.25).

In Fig. 2.21, two VSE resistance calculation methods are compared: analytical approach from the literature with the fact that VSE proportionality constant is 0.5 10^{-9} and FEM results. The comparison shows that although two methods give approximately same resistance results for low velocities, analytical approach gives lager VSE resistance values than ones found by the fitted equations for the larger velocity values than 500 m/s.

2.2.3 Modeling of Contact Resistance between Rail and Armature

Investigation of the electrical contact transition between two different materials in electrical circuits is a challenging problem. The real contact area is much less than the apparent contact area as explained in [50] due to the fact that the current is only flowing through the effective contact surface in the contact zone. Moreover, electrical resistance in the contact zone is higher than the bulk electrical resistance. Pressure dependency of contact resistivity is the main problem that makes the contact transition significant in electrical engineering. Holm presented the contact resistance in [50] as

in Eq. (2.26) where R_c is the contact resistance, ρ_1 and ρ_2 are reactivities of contact members, H_{soft} is the hardness of softer contact member and F_c is the contact force.

$$R_c = \frac{\rho_1 + \rho_2}{2}\sqrt{\frac{H_{soft}}{F_c(t)}} \tag{2.26}$$

In [42], it is noted that Eq. (2.26) is valid only for the contact force values from 0.1 N to 100 N. However, in EML applications, contact force exceeds 100 kN for 2 MJ charging energy. According to [51], there is an empirical formula for contact resistance of an EML. For Al–Cu area contact, a simplified form is shown in Eq. (2.27).

$$R_c = \frac{k_0}{(0.102F_c(t))^m} \approx \frac{19.2}{F_c(t)} \tag{2.27}$$

In Eq. (2.27), k_0 and m are contact transition constants for materials of the contact members. Contact force consists of two components: the electromagnetic force which is dependent of rail current and the mechanical force due to the preload process which is constant during the excitation as given in Eq. (2.28). Experiments show that $F_{c_{mech}}$ is 2.5 kN for only one side of the armature.

$$F_c(t) = F_{c_{em}}(t) + F_{c_{mech}} \tag{2.28}$$

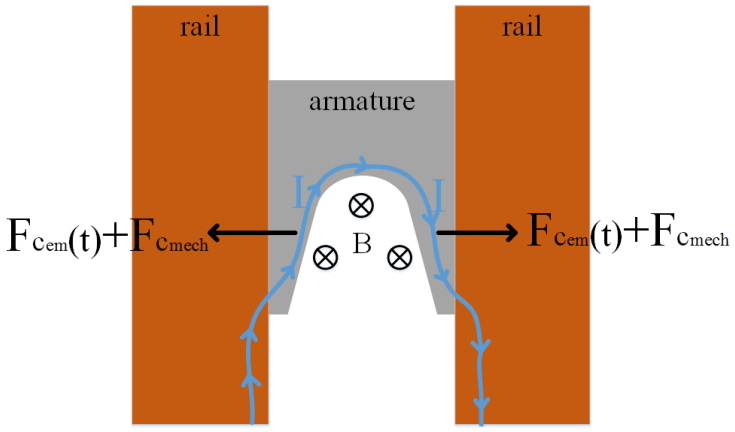

Figure 2.22: Electromagnetic and mechanical contact force.

Directions of electromagnetic contact forces are determined by the direction of the current in the armature and magnetic field just behind the armature. The directions of contact forces are given in Fig. 2.22.

Zhou *et al.* did a circuit simulation of their EML based on multifactor effects using Eq. (2.27) for contact resistance in [52]. In this study, the average contact force is calculated to find a contact resistance. Although this approach is reasonable to take the voltage drop due to the contact resistance into account, it does not contain the effect of the contact transition on the current density distribution on the contact surface.

Since the current density distribution on the contact surface depends on the distribution of the contact pressure, in this study contact resistance is modeled as not only time dependent but also position dependent. A layer with 0.5mm thickness (80 times smaller than the caliber) is included between armature and rail with position and time dependent resistivity. The contact layer section is divided into 100 pieces in the FEA model, each of which having variable conductivity with contact pressure. In addition to the contact layers, the armature is also divided into 100 pieces as in Fig 2.23. In every time step, contact forces of each armature piece including mechanical and electromagnetic parts are taken from the previous time step to calculate the contact resistivity of the each layer piece. This approach is developed by Doğa Ceylan, M. Uğur Güdelek and Ozan Keysan in [53].

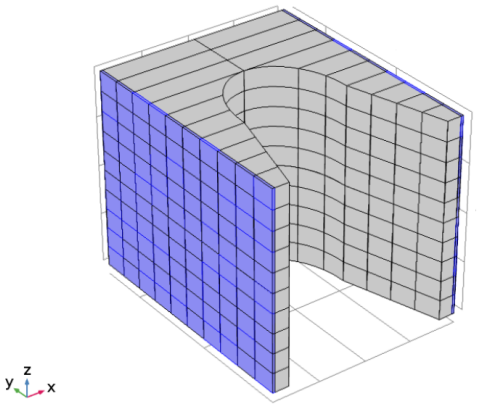

Figure 2.23: Contact layers with pressure-dependent conductivities, [53].

Calculation of the position and time dependent conductivities of contact layer is given

in Eq. (2.29) and (2.30) where ρ_c is the conductivity of one piece of contact layer, A is the area of one piece of contact layer, l is the thickness of the contact layer chosen as 0.5 mm in this study which is 80 times smaller than the caliber. On one hand, decreasing the thickness of the contact layer makes the FE model more realistic. On the other hand, decreasing the thickness of the contact layer causes too small mesh elements around it, which increases the computational cost of the model.

$$R_c(t,y,z) = \frac{19.2}{F_c(t,y,z)} = \rho_c(t,y,z)\frac{l}{A} \tag{2.29}$$

$$\rho_c(t,y,z) = \frac{19.2\,A}{F_c(t,y,z)\,l} = \frac{19.2}{P_c(t,y,z)\,l} \tag{2.30}$$

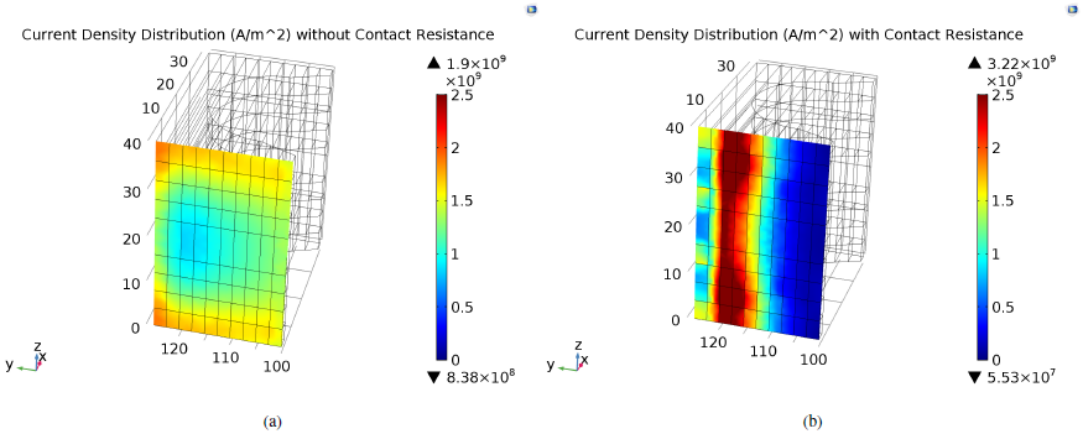

Figure 2.24: Influence of contact resistance on the current density distribution on the contact surface: (a) no contact resistance, (b) with contact resistance, [53].

Fig. 2.24 shows the change of the current density distribution on the contact surface with the contact layers for a time instant of current rising interval. Current concentrates in a smaller area which has large contact force than the one without contact resistance which may cause melting on the contact surface.

2.2.4 Power Loss due to the Induced Electromotive Force

According to Lenz's Law, induced voltage due to the change of magnetic flux on a coil is given in Eq. (2.31). E is the voltage drop or induced electromotive force

(EMF), λ is the total magnetic flux, N is the number of turns and ϕ is magnetic flux.

$$E = -\frac{d\lambda}{dt} \quad where \quad \lambda = N\,\phi(t) \tag{2.31}$$

Inductance is defined as the total magnetic flux that a coil can create per ampere. From the definition of inductance, Eq. (2.32) can be written.

$$L = \frac{\lambda}{I} \tag{2.32}$$

Eq. (2.33) can be obtained by substituting Eq. (2.32) into Eq. (2.31).

$$E = -\frac{d[L(x(t))I(t)]}{dt} \tag{2.33}$$

Since both the inductance of EML and rail current depends on time, the chain rule can be applied to Eq. (2.33) in order to obtain Eq. (2.34).

$$E = -[I(t)\frac{dL(x(t))}{dt} + L(x(t))\frac{dI(t)}{dt}] \tag{2.34}$$

In Eq. (2.34), while the first term represents the voltage drop due to the back EMF, the second term represents the voltage drop due to the barrel inductance. In order to simplify the back EMF voltage drop term, this term can be multiplied and divided by dx as in Eq. (2.35).

$$E = -[I(t)\frac{dL(x(t))}{dx}\frac{dx(t)}{dt} + L(x(t))\frac{dI(t)}{dt}] \tag{2.35}$$

Since the derivative of barrel inductance with respect to the armature position is equal to the inductance gradient and the derivative of armature position with respect to time is equal to the armature velocity, Eq. (2.36) can be written as below.

$$E = -[I(t)\,L'\,v(t) + L'\,x(t)\frac{dI(t)}{dt}] \tag{2.36}$$

Finally, equations of back EMF resistance depending on armature velocity and barrel inductance depending on the armature position is given in (2.37) and (2.38). Although there is no physical meaning of back EMF resistance, like resistive heat loss, in an EML, it is possible to model it as a resistance in the simulation as in Eq. (2.37).

$$R_{back\,emf}(v(t)) = L'\,v(t) \tag{2.37}$$

$$L(x(t)) = L'\,x(t) \tag{2.38}$$

2.3 Frictional Loss

Mechanical friction exists between the rail and armature due to contact force. Frictional force on the armature can be expressed as in Eq. (2.39) where μ(v) is velocity dependent dynamic friction coefficient. Since there are two contact surface between the rails and armature, it is required to multiply the contact force by two.

$$F_{fric} = 2\,F_c(t)\,\mu(v) \tag{2.39}$$

Dynamic friction coefficient is modeled experimentally in [54]. In Eq. (2.40), μ_{H} is static friction coefficient between copper and aluminum materials, μ_{G} is limiting value of dynamic friction coefficient and α is the shaping parameter of dynamic friction coefficient.

$$\mu(v) = (\mu_H - \mu_G)e^{-\alpha v} + \mu_G \tag{2.40}$$

Characteristic of μ can change due to the magnitude of contact force and speed. In [54], the characteristic for larger contact force than 100 N is given. In Table 2.2, the values of dynamic friction coefficient parameters are given in order to find realistic frictional loss case.

In Fig. 2.25, variation of dynamic friction coefficient with respect to armature velocity

Table 2.2: Parameters of dynamic friction coefficient.

static coefficient (μ_{H})	0.45
limiting value (μ_{G})	0.07
shaping parameter (α)	0.05

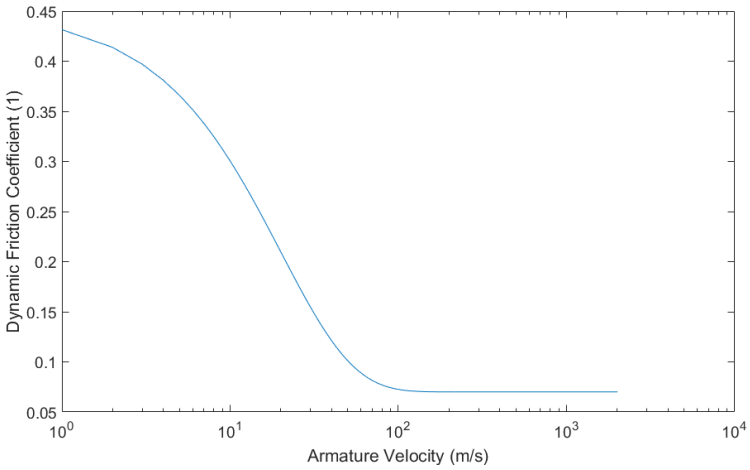

Figure 2.25: Dynamic friction coefficient with respect to armature velocity.

for the given coefficient parameters is shown. As stated previously, contact force consists of two parts: electromagnetic force which varies during the excitation with the change of rail current and mechanical preload force which is constant during the excitation.

$$F_c = F_{c_{em}}(t) + F_{c_{mech}} \tag{2.41}$$

While $F_{c_{mech}}$ can be calculated experimentally, in order to find the value of $F_{c_{em}}$ analytically, it is required to do some approximations. In Fig. 2.26, schema of electromagnetic component of contact force is given where c is the caliber, l_{wing} is the length of armature wing.

In Fig. 2.26, to derive an analytical equation for $F_{c_{em}}$, used assumptions are available below:

- Magnetic field on one limb of the armature is created only by the current pass-

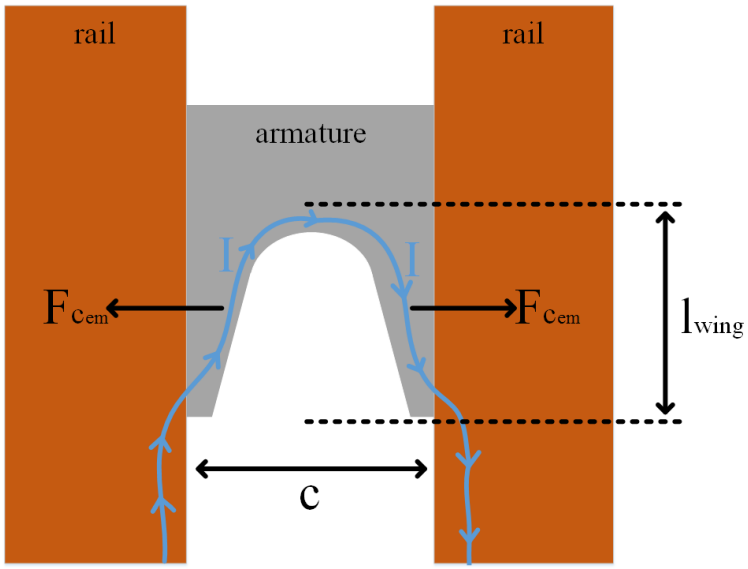

Figure 2.26: Schema of electromagnetic contact force.

ing through the other limb.

- Distance between the currents through armature limbs is equal to caliber.
- Currents through the armature wings are parallel to each other.
- Skin depth in the front side of the armature wings is much smaller than the length of the wings.

Equation of the magnetic field on one armature limb can be written as Eq. (2.41) with the consideration of the first assumption.

$$B = \frac{\mu_0 I}{2\pi c} \tag{2.42}$$

Equation of $F_{c_{em}}$ with respect to magnetic field is given in Eq. (2.42) according to Lorenz Law.

$$F_{c_{em}} = I l_{wing} B \tag{2.43}$$

Then, Eq. (2.43) can be obtained by using both Eq. (2.41) and (2.42).

$$F_{c_{em}} = I l_{wing} \frac{\mu_0 I}{2\pi c} = 2\ 10^{-7} \frac{l_{wing} I^2}{c} \tag{2.44}$$

As derived above, it is possible to obtain an analytical equation for $F_{c_{em}}$ only using the given assumptions. In this study, $F_{c_{em}}$ is also calculated by FEM in order to get the frictional loss in the model. Comparison of these methods will be discussed in the next chapter.

In the next chapter, the results of the described FE model will be presented. In this chapter, variation of PPS module currents, barrel resistances and breech voltage will be calculated. Also, current density, magnetic field and the electromagnetic force distributions in the rails and armature will be observed. Results of analytic and FE calculations will be compared. Moreover, kinematic equations will be solved to find the muzzle velocity and kinetic energy. In the last two sections of the chapter, results of thermal and recoil forces will be presented.

CHAPTER 3

SIMULATION RESULTS

Calculation of the EML parameters during the launch is a complex task due to the dependency of barrel resistance and inductance on the frequency of the excitation current, velocity and position of the armature. The FE model explained in Chapter 2 is used for this purpose. Muzzle velocity of the armature and the efficiency of the total system will be calculated. In addition to the variation of barrel resistance and inductance, breech voltage and PPS currents, current and magnetic field distribution in the rails and armature will be analyzed in this chapter. Also, electromagnetic forces acting on the armature, rails and busbars and the results of the thermal analysis will be discussed.

3.1 Barrel Resistances and Breech Voltage

As discussed in Chapter 2, PPS capacitors are charged with 10 kV. In the PPS side, there exist 10 modules each of which has 200 kJ. Hence, the total input energy to the system is 2 MJ. The switching sequence of these modules are given in Tab. 3.1. Since the barrel is connected to the PPS modules in series, the sequence in order to create a pulsed current with 1 MA peak is different from the one in Table 2.1 where the PPS modules are shorted.

In the model, FE mesh elements of the barrel side and electrical components of PPS modules are modeled in the same simulation environment as given in Fig. 2.5. Therefore the resistance or inductance change in the barrel side affects the current waveforms in the PPS side. In Eq. (3.1), capacitor equation for n^{th} module is given for the discharging process where C is the capacitance value, V_{c_n} is the capacitor voltage of

Table 3.1: Switching instants of PPS modules connected to the barrel to get 1 MA current peak with

Module 1-5	0 ms
Module 6	0.25 ms
Module 7	0.55 ms
Module 8	0.8 ms
Module 9	1 ms
Module 10	1.1 ms

n^{th} module, and I_{module_n} is the module current of n^{th} module.

$$C\frac{dV_{c_n}}{dt} = -I_{module_n} \tag{3.1}$$

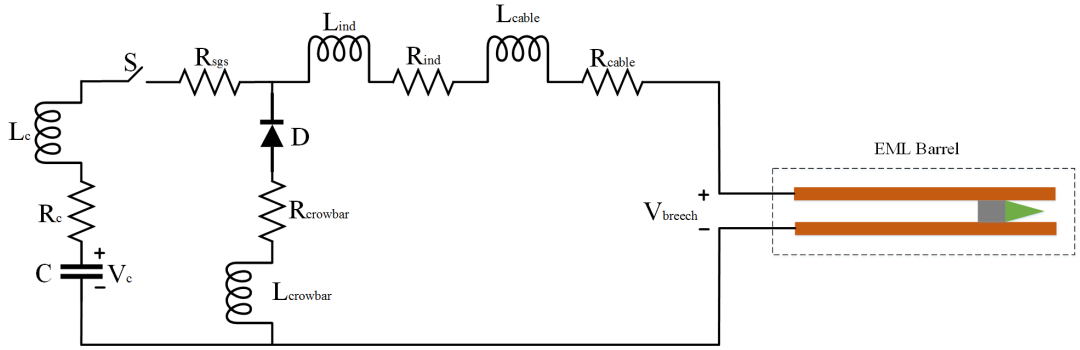

Figure 3.1: Connection of a PPS module to the barrel of the EML in series.

The schema of one PPS module connected to the barrel in series is given in Fig. 3.1. However, since the crowbar diode does not conducts during the capacitor discharging, equivalent circuit of Fig. 3.1 becomes in Fig. 3.2.

The capacitor voltage of n^{th} module can be expressed with respect to module resistances and inductances, module current and breech voltage as per Eq. (3.2) during the discharging process. In Eq. (3.2), R_c is capacitor internal resistance, R_{sgs} is switch internal resistance, R_{ind} is the resistance of the pulse shaping inductor, R_{cable} is the resistance of the cable connecting the module to the recoil busbar, L_c is the internal inductance of the capacitor, L_{ind} is the inductance of pulse shaped inductor, L_{cable} is

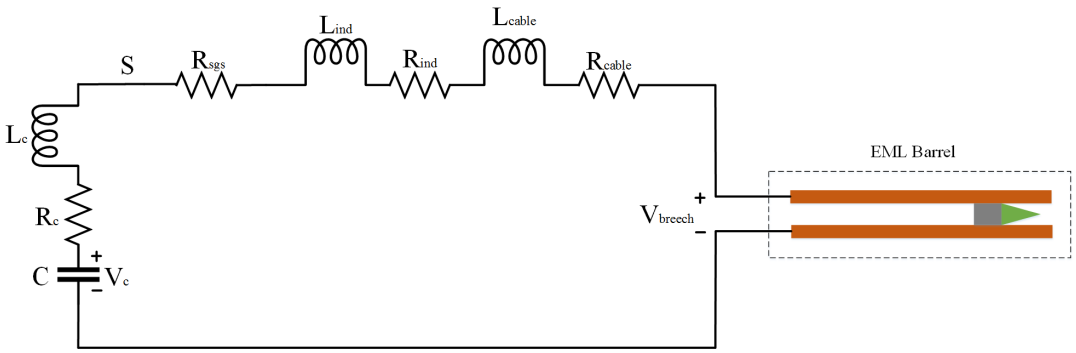

Figure 3.2: Equivalent circuit of one module connected to the barrel during the capacitor discharging.

the inductance of the cable connecting the module to the recoil busbar and V_{breech} is the breech voltage. The values of these components are given in Tab. 1.2.

$$V_{c_n} = (R_c + R_{sgs} + R_{ind} + R_{cable})I_{module_n} + (L_c + L_{ind} + L_{cable})\frac{dI_{module_n}}{dt} + V_{breech} \tag{3.2}$$

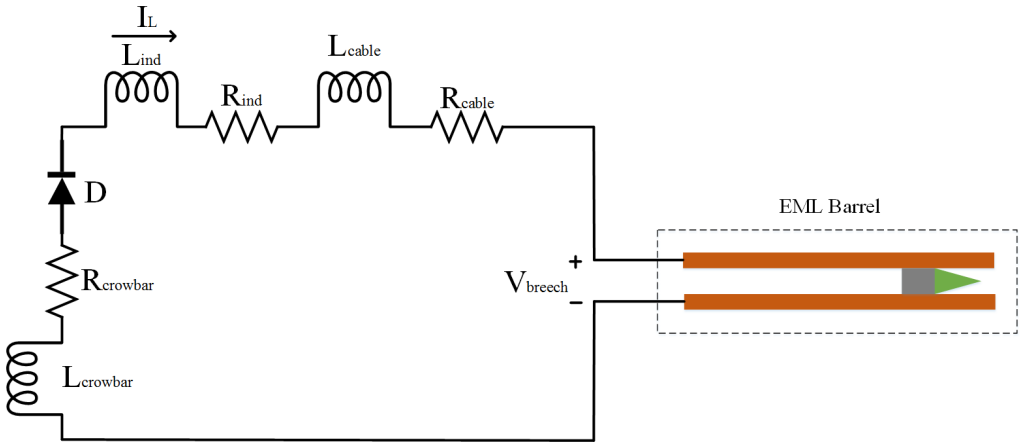

Figure 3.3: Equivalent circuit of one module connected to the barrel during the free-wheeling.

During the free-wheeling process, the crowbar diode conducts and capacitor voltage

is zero. The circuit equation for an module can be written as in Eq. (3.3).

$$0 = (R_{crowbar} + R_{ind} + R_{cable})I_{module_n} + (L_{crowbar} + L_{ind} + L_{cable})\frac{dI_{module_n}}{dt} + V_{breech} \tag{3.3}$$

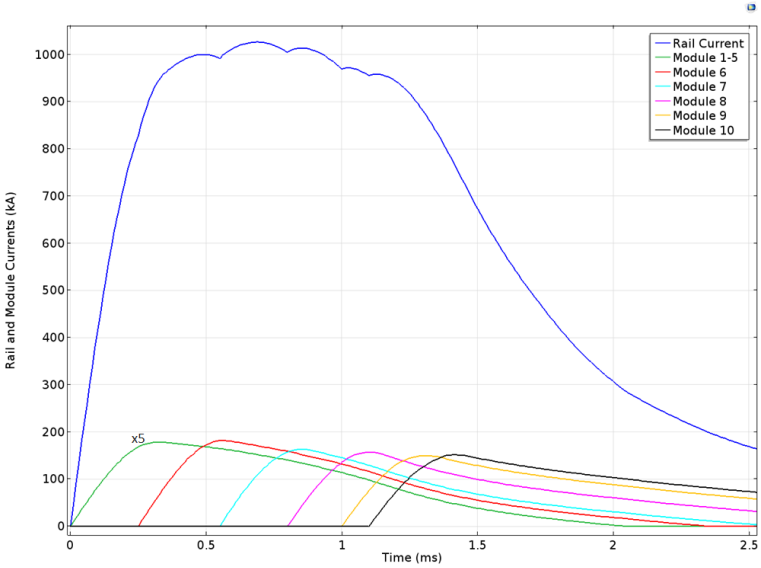

Figure 3.4: Module currents and rail current waveforms.

Rail current is equal to the summation of 10 module currents as given in Eq. (3.4). Also, module currents and resultant rail current waveforms are given in Fig. 3.4. It reaches its peak value, 1026 kA, at 0.7 ms.

$$I = \sum_{n=0}^{10} I_{module_n} \tag{3.4}$$

The breech voltage can be expressed with respect to the AC resistance, velocity skin effect resistance, contact resistance, back EMF resistance and inductance of the barrel as in Eq. (3.5).

$$V_{breech} = IR_{ac}(f,x) + IR_{vse}(v,x) + IR_c(F_c) + IR_{back\,EMF}(v) + L(x)\frac{dI}{dt} \tag{3.5}$$

Change of barrel resistances during the firing is given in Fig. 3.5.

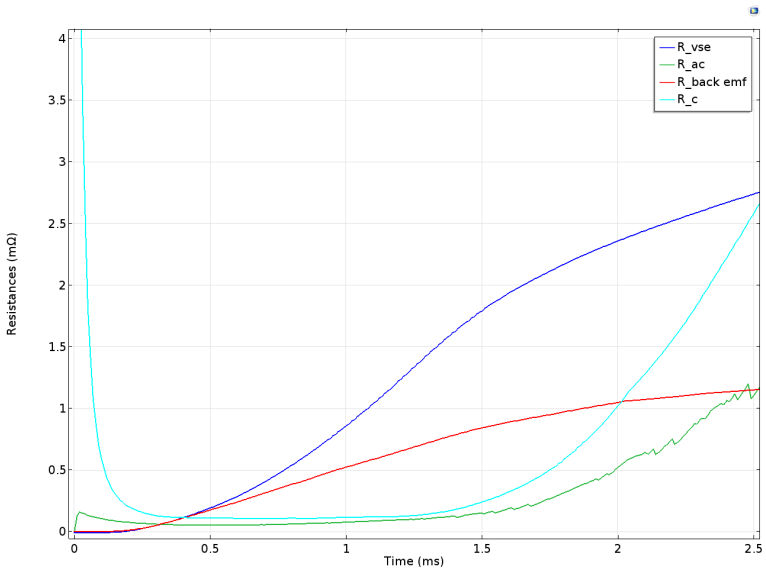

Figure 3.5: Change of barrel resistances during the excitation.

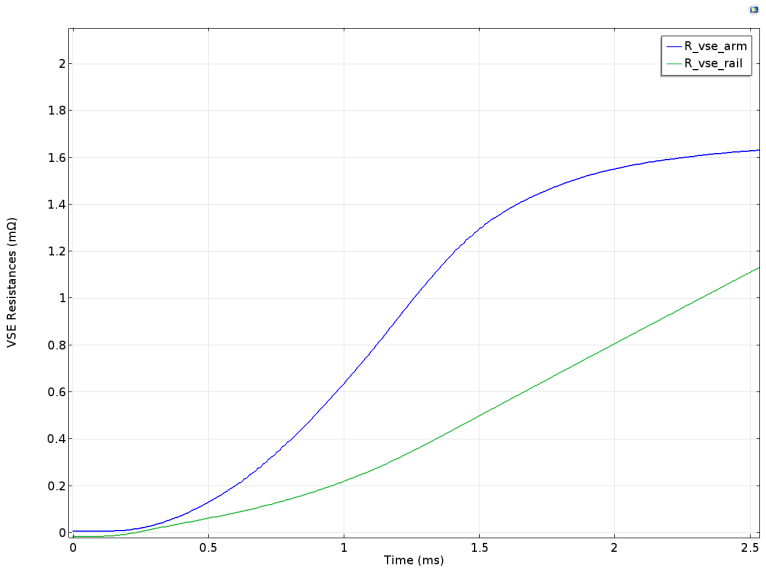

Figure 3.6: Change of armature and rail VSE resistances during the excitation.

For low rail currents, contact resistance has its largest value. In addition, AC resistance component depends on the frequency of rail current and position of armature, since the contact force is too small. Although the frequency is smaller than the one when rail current rises at the muzzle exit instant, AC resistance increases with the increase of armature displacement during the excitation. Moreover, back EMF resistance only depends on the armature velocity. Also, it is possible to observe that

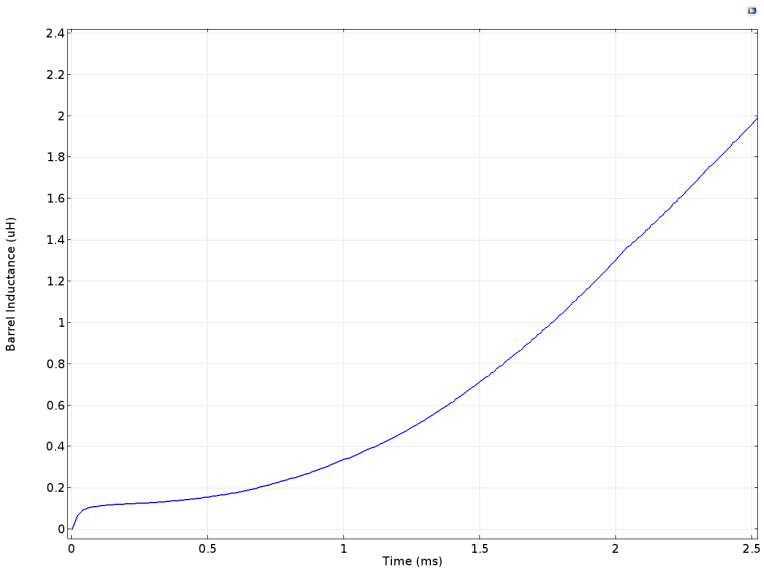

Figure 3.7: Change of barrel inductance during the excitation.

the VSE resistance increases with armature position and velocity. It can be concluded that VSE resistance is dominant when the rail current is at its peak which causes dominant heat loss at the barrel side. Fig. 3.5 shows VSE resistance of the armature and rail components. The variations of these components with time are given in Fig. 3.6. In addition, the change of barrel inductance is given in Fig. 3.7. As derived in the previous chapter, it linearly changes with armature position.

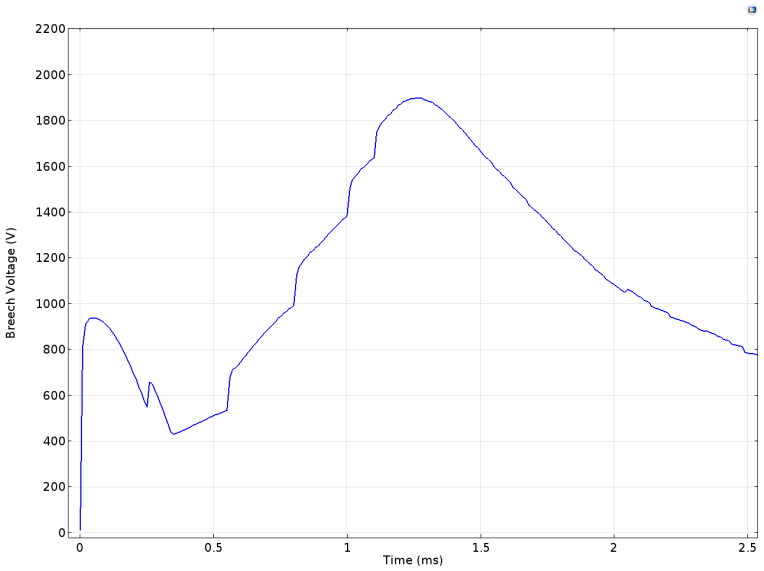

Figure 3.8: Breech voltage.

Breech voltage waveform until armature exits the barrel is given in Fig. 3.8. Since the breech voltage is proportional to the derivative of rail current, breech voltage can take negative values during the excitation. This happens if the period between switching instants is long enough. Firing one of the modules after the polarization of breech voltage changes is dangerous situation, as the polarization of the barrel is negative, diodes of the modules, which are not fired yet, starts conducting by themselves. Then, if one of these module is fired in this situation, its capacitor is shorted through conducting diode which may damage both the capacitors and the diodes.

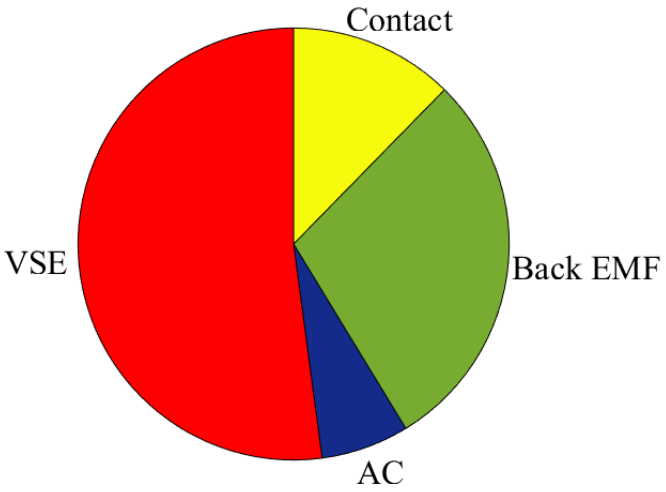

Figure 3.9: Energy loss distribution due to the barrel resistances.

In Eq. (3.6), power loss calculations due to the barrel resistances are given.

$$\begin{aligned} P_{vse} &= I^2 R_{vse} \\ P_{ac} &= I^2 R_{ac} \\ P_{back\ EMF} &= I^2 R_{back\ EMF} \\ P_{contact} &= I^2 R_{contact} \end{aligned} \tag{3.6}$$

$$W_{loss} = \int_0^{t_{exit}} P_{loss}(t) dt \tag{3.7}$$

Variation of power loss due to each barrel resistance is calculated using Eq. (3.6). As given in Eq. (3.7), integration of power losses gives the energy loss for each component. The energy loss distribution due to barrel resistances is given in Fig. 3.9.

3.2 Current Density and Magnetic Field Distribution

Current density and magnetic field distribution in the rails and armature are critical in order to analyze the Lorentz force acting on them and temperature change in them. In [55], Zhao *et al.* discussed the solution of EML problem from the electromagnetic point of view. Also, very fundamental electromagnetic equations in order to reach simplest form of finite element analysis equations are listed in Eq. (3.8)-(3.14).

Ampere's law:

$$\nabla \times \vec{H} = \vec{J} + \frac{\partial \vec{D}}{\partial t} \tag{3.8}$$

Faraday's law:

$$\nabla \times \vec{E} = -\frac{\partial \vec{B}}{\partial t} \tag{3.9}$$

Gauss' law:

$$\nabla \cdot \vec{D} = \rho_v \tag{3.10}$$

Gauss' law for magnetism:

$$\nabla \cdot \vec{B} = 0 \tag{3.11}$$

Charge continuity equation:

$$\nabla \cdot \vec{J} = -\frac{\partial \rho_v}{\partial t} \tag{3.12}$$

Magnetic flux density equation:

$$\vec{E} = -\nabla V - \frac{\partial \vec{A}}{\partial t} \tag{3.13}$$

Electric field intensity equation:

$$\vec{B} = \nabla \times \vec{A} \tag{3.14}$$

In these equations, $\vec{H}$ is the magnetic field intensity [A/m], $\vec{J}$ is the current density [A/m^2], $\vec{D}$ is the electric flux density [C/m^2], $\vec{E}$ is the electric field intensity [V/m], $\vec{B}$ is the magnetic flux density [Wb/m^2 or T], t is the time [s], ρ_v is the volume charge density, V is the electric scalar potential [V] and $\vec{A}$ is the magnetic vector potential [Wb/m].

Constitutive equations for the given fundamental electromagnetic equations are also available in Eq. (3.15)-(3.19).

$$\vec{B} = \mu\vec{H} \tag{3.15}$$

$$\vec{D} = \varepsilon\vec{E} \tag{3.16}$$

$$\vec{J} = \sigma\vec{E} \tag{3.17}$$

$$\mu = \mu_0\mu_r \tag{3.18}$$

$$\varepsilon = \varepsilon_0\varepsilon_r \tag{3.19}$$

In the constitutive equations, μ is the permeability of the material [H/m], μ_0 is the permeability of free space [4π 10^{-7}], μ_r is the relative permeability, ε is the permittivity of the dielectric [F/m], ε_0 is the permittivity of free space [8.85 10^{-12}], ε_r is the relative permittivity and σ is the electric conductivity [S/m].

By assuming that all the materials used in the FE analysis, excluding containment, are magnetically linear which means their relative permeability is one, Eq. (3.20) can be written.

$$\vec{B} = \mu_0\vec{H} \tag{3.20}$$

Eq. (3.8) can be simplified to Eq. (3.21) using quasi-static approximation by assuming that the dimensions of the analyzed EML geometry in FE model are considerably smaller than the electromagnetic wavelength. This means the displacement current term is zero.

$$\nabla \times \vec{H} = \vec{J} \tag{3.21}$$

Moreover, Eq. (3.10) can be expressed as Eq. (3.22) again using quasi-static approximation by taking the time derivative on both sides of Eq. (3.10).

$$\frac{\partial \rho_v}{\partial t} = 0 \tag{3.22}$$

By substituting Eq. (3.12) into Eq. (3.22), Eq. (3.23) can be obtained.

$$\nabla \cdot \vec{J} = 0 \tag{3.23}$$

Finally, magnetic vector potential equation can be obtained by combining Eq. (3.13), (3.14), (3.17), (3.20) and (3.21). Also, scalar potential equation can be obtained by combining Eq. (3.13), (3.17), (3.20) and (3.23).

Magnetic vector potential equation:

$$\sigma \frac{\partial \vec{A}}{\partial t} + \frac{1}{\mu_0}[\nabla \times (\nabla \times \vec{A})] + \sigma \nabla V = 0 \tag{3.24}$$

Scalar potential equation:

$$\nabla \cdot (\sigma \nabla V) = 0 \tag{3.25}$$

FE software, COMSOL Multiphysics, solves Eq. (3.24) and (3.25) in each time step for each mesh element to calculate the current density and magnetic field distribution.

As discussed previously, there exist two electromagnetic phenomenons which influence the current density distribution in the rails: the skin and the proximity effects. Analytical solution to the current density distribution in an EML is complex because of these effects. In this study, described FE model includes these effects in its calculation. In Fig 3.10, a cross-section of the rails which is going to be used to observe the current density and magnetic field distribution are given.

During the current rising time, rate of change of the current is at its largest value, therefore skin depth is small. As a result, the largest current density value can be observed at the time instant when the current reaches its peak value just after current rising time. Rail current reaches its peak value at 0.7 ms. Current density distribution on the given cross-section of the rails is presented in Fig. 3.11.

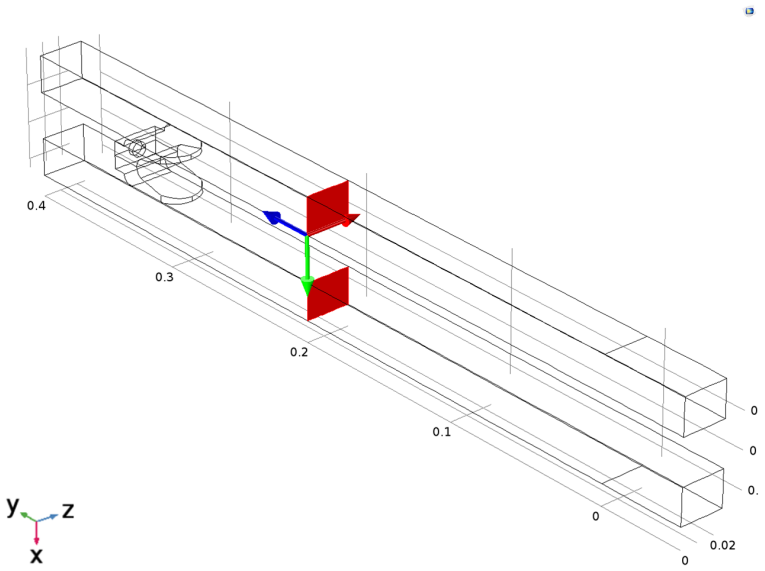

Figure 3.10: Cross-section of rails.

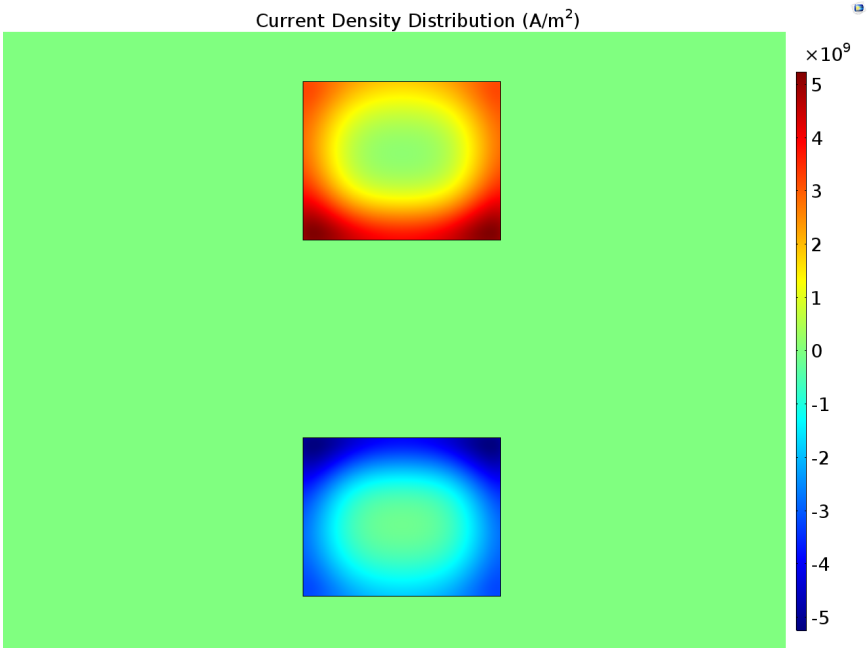

Figure 3.11: Current density distribution in y-direction in the rails at 0.7 ms when the excitation current is at its peak value, 1026 kA.

In Fig. 3.12, The magnetic flux density distribution is given with its vectors on the rail cross-section. The maximum created flux density at 0.7 ms by the excitation current is 22.3 T.

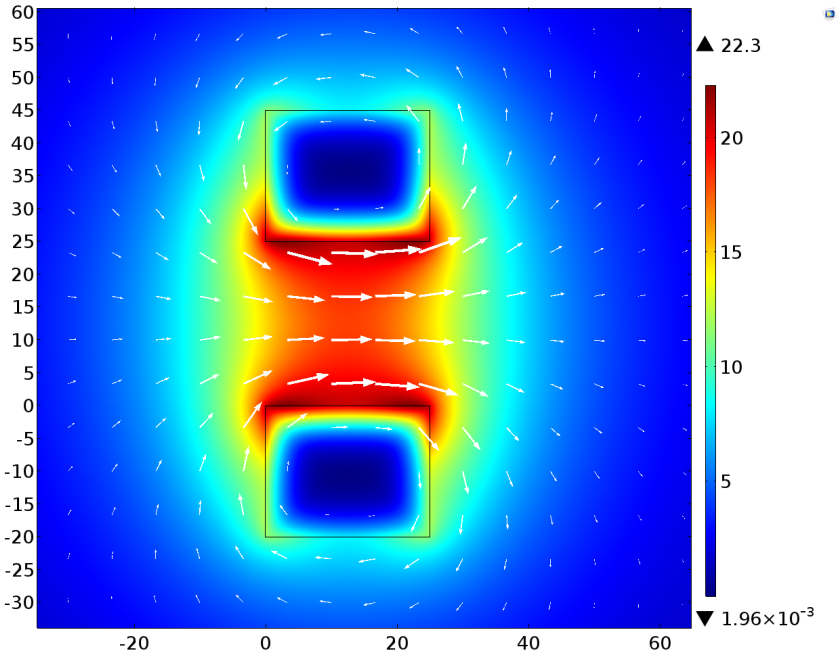

Figure 3.12: Normalized magnetic flux density distribution in the rails and air around the rails at the peak current time, 0.7 ms.

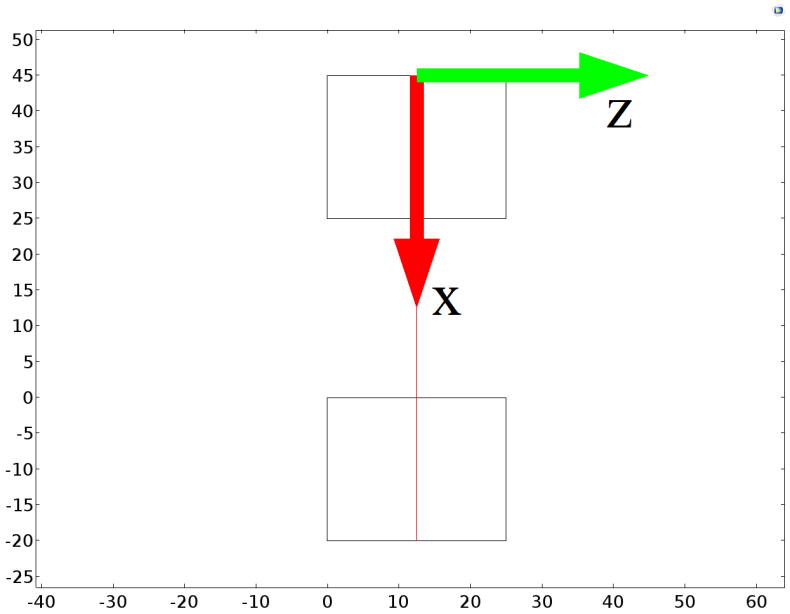

Figure 3.13: Line on the rail cross-section.

In order to analyze the current density and magnetic flux density distributions in the rails and caliber, a line from upper rail to lower one is described as given in Fig. 3.13. Fig. 3.14 shows the y component of the current density and the x component of the

magnetic flux density values along described line. In addition to the rails, current density and magnetic flux density distribution in the armature is significant in order to calculate electromagnetic force acting on the armature and kinematic equations. Normalized current density distribution and current density distribution in x-direction for 0.7 ms is given respectively in Fig. 3.15 and 3.16.

As in Fig. 3.17, maximum magnetic field density value observed in the armature at 0.7 ms is 43.7 T.

3.3 Electromagnetic Forces and Pressures

During the launch, electromagnetic forces are created on the rails and armature. Since the directions of the currents in two rails are in opposite directions, the rails repel each other. As this can cause the loss of contact between the rails and armature which may damage the barrel, a mechanical support structure is used around the rails. Analysis of the electromagnetic pressure acting on the rails is critical for the design of this mechanical support. Also, analysis of the electromagnetic pressure acting on the armature is essential for the calculation of kinematic equations of the EML.

Electromagnetic force density distribution in the rails and armature can be calculated using Eq. (3.26) where $\vec{f}$ is electromagnetic force density vector [N/m^3], $\vec{J}$ is current vector [A/m^2] and $\vec{B}$ [Wb/m^2 or T] is magnetic flux density vector.

$$\vec{f} = \vec{J} \times \vec{B} \tag{3.26}$$

By combining Eq. (3.26) with Eq. (3.20) and (3.21), Eq. (3.27) can be obtained as discussed in [56], where $\vec{H}$ is the magnetic field intensity vector [A/m] and μ_0 is the permeability of free space. In FEA, in order to calculate $\vec{f}$, Eq. (3.27) is used after solving magnetic vector potential (3.24) and scalar potential (3.25) equations.

$$\vec{f} = (\nabla \times \vec{H}) \times (\mu_0 \vec{H}) = \mu_0((\nabla \times \vec{H}) \times \vec{H}) \tag{3.27}$$

In Fig. 3.18, magnitude of electromagnetic force density distribution and vectors in

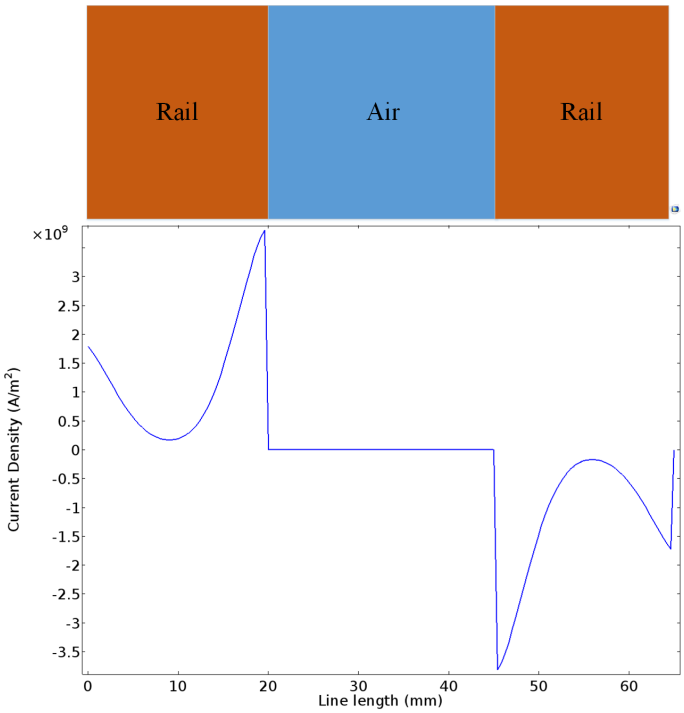

(a) Current density (y-component).

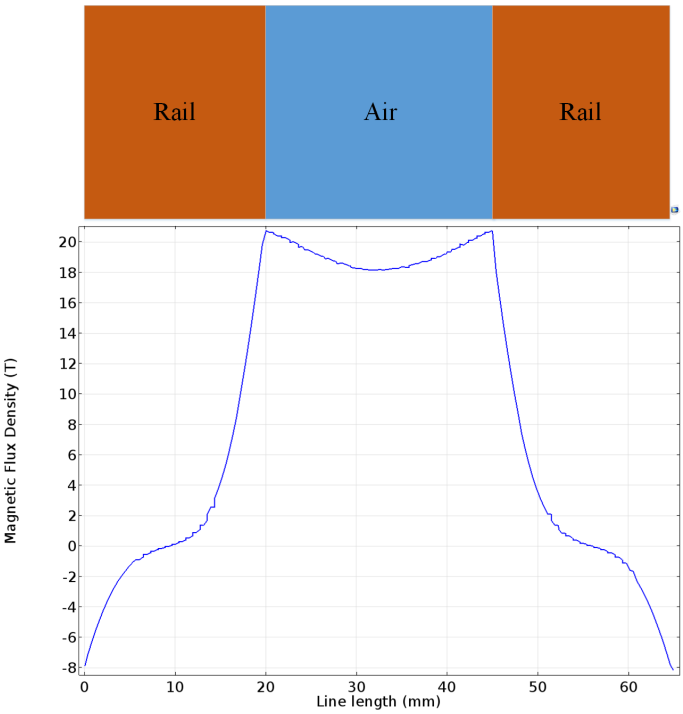

(b) Magnetic flux density (z-component).

Figure 3.14: Magnetic flux density (z-component) and current density (y-component) on the described line at 0.7 ms.

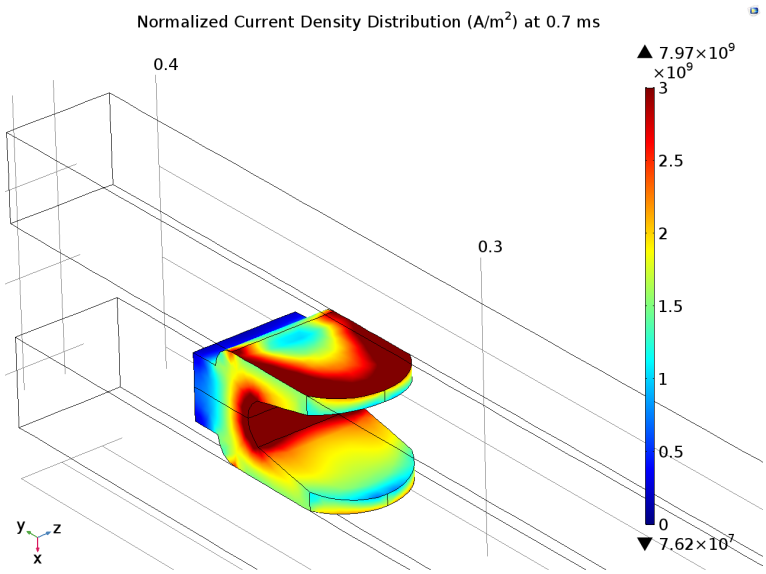

Figure 3.15: Normalized current density distribution in the armature at 0.7 ms.

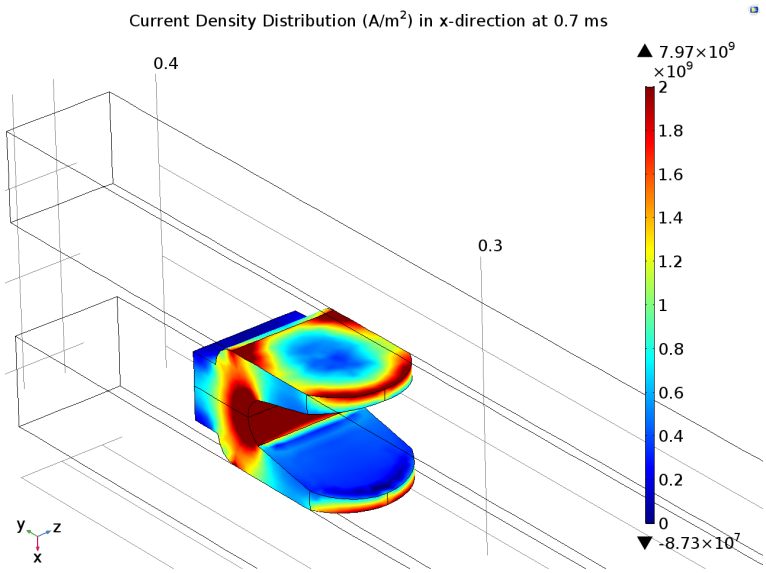

Figure 3.16: Current density distribution in x-direction at 0.7 ms.

the rails are given for 0.7 ms during the launch. Fig. 3.18 shows that rails repel each other which may cause losing contact between rails and armature.

In order to obtain the electromagnetic force vectors acting on the rails and armature, it is required to calculate the volume integral of electromagnetic force density vectors.

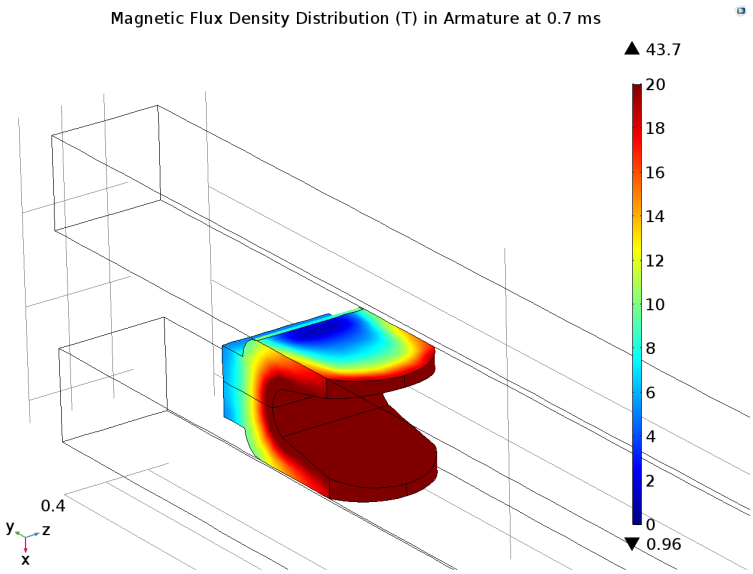

Figure 3.17: Magnetic flux density distribution in the armature at 0.7 ms.

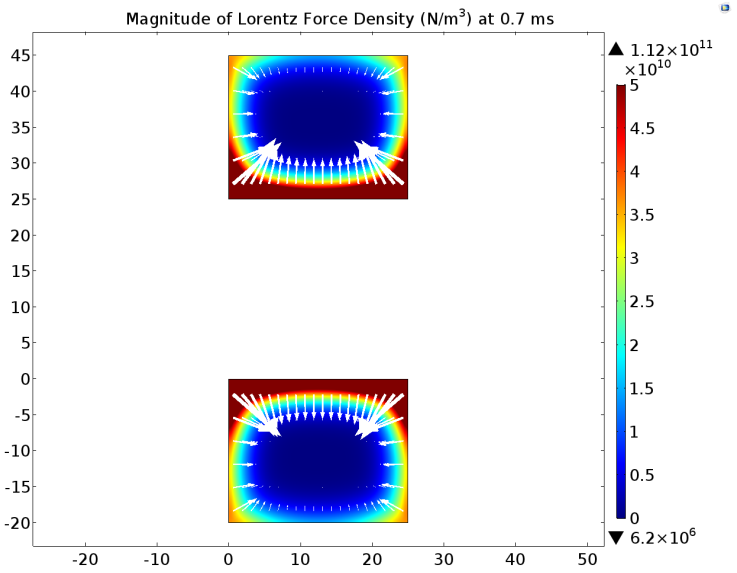

Figure 3.18: Electromagnetic force density distribution in the rails.

Eq. (3.28) shows the electromagnetic force vectors calculation.

$$\vec{F} = \mu_0 \oint ((\nabla \times \vec{H}) \times \vec{H}) dV \tag{3.28}$$

In the proposed FE model, the total electromagnetic force acting on single rail can be calculated using Eq. (3.28) with the volume integration of this rail. However, in

the proposed FE model, the armature is stationary at the position of preload ($x_{preload}$) which is 0.3 m. Therefore, in order to calculate the change of total electromagnetic force acting on one rail with respect to time, in the model, Eq. (3.29) is used where x is the armature displacement after armature loading.

$$\vec{F} = \frac{\mu_0(x + x_{preload})}{x_{preload}} \oint ((\nabla \times \vec{H}) \times \vec{H}) dV_{rail} \tag{3.29}$$

In Fig. 3.19, the total electromagnetic force acting on one rail in x-direction, which is calculated using Eq. (3.29), is given with rail current. As it can be observed from Fig. 3.19, although armature always moves forward during the excitation, the total rail force starts decreasing, since the rail current decreases after 1.3 ms.

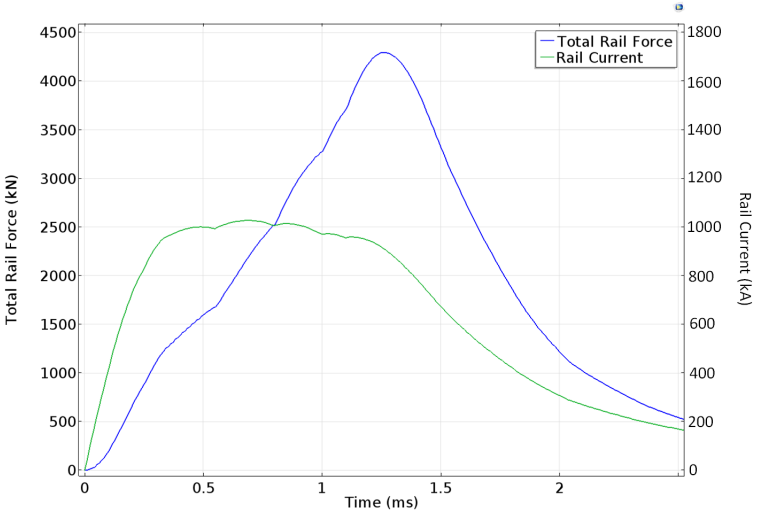

Figure 3.19: Total electromagnetic force acting on one rail in x-direction and rail current.

As discussed in [56], an EML can be considered as a transmission-line model. In that model, it may be assumed that most of the excitation current flows through the inner surfaces of the rails. Therefore, this approach can be called the inner surface approach. The magnetic field on the inner surface of one rail, which is created by another, can be written as in Eq. (3.30).

$$B = \frac{\mu_0 I}{2\pi c} \tag{3.30}$$

The electromagnetic repelling force acting on one rail can be calculated as in Eq. (3.31). Although Eq. (3.31) is an alternative formula to Eq. (3.29), Eq. (3.29) is more reliable than (3.31) because of the aforementioned assumptions.

$$F_{rail} = \frac{\mu_0 I}{2\pi c} I(x_{preload} + x) \tag{3.31}$$

Electromagnetic average pressure on the contact surface of one rail can be calculated as in Eq. (3.32) using the inner surface approach. It can be observed that the average pressure is independent of armature position.

Inner surface approach:

$$P_{rail} = \frac{\frac{\mu_0 I}{2\pi c} I(x_{preload} + x)}{h(x_{preload} + x)} = \frac{\mu_0 I^2}{2\pi c h} \tag{3.32}$$

In [57], Stonkus *et al.* from ISL use another approach for the calculation of electromagnetic pressure on the rails. In Eq. (3.33), the formula for the rail pressure used in their study is given where L' is the inductance gradient explained as derivative on the barrel inductance with respect to the armature position, c is the caliber, 25 mm, h is the height of the rails, 25 mm.

ISL's approach:

$$P_{rail} = P_{arm} = \frac{F_{arm}}{ch} = \frac{L'}{2ch} I^2 \tag{3.33}$$

It is significant to note that Eq. (3.32) and (3.33) have the same approximation which is the fact that electromagnetic forces acting on the rails are created only on the inner surface of the rails because of the skin effect. In [57], it is stated that this is a good approximation directly behind the armature; however, the magnetic diffusion leads to bulk forces in other rail sections. Therefore, in the FE model, neither inner surface approach nor ISL's approach are used. Average electromagnetic pressure for the mesh elements in the rails are calculated using Eq. (3.34) derived from Eq. (3.29).

FE approach:

$$[\vec{P}_{rail_{average}}]_x = \frac{[\vec{F}_{rail}]_x}{(x + x_{preload})h} = \frac{\mu_0}{x_{preload}h} \oint [((\nabla \times \vec{H}) \times \vec{H})]_x dV_{rail} \qquad (3.34)$$

The change of average electromagnetic pressure acting on one rail in x-direction for three approaches is given in Fig. 3.20. As expected, ISL's and inner surface approaches give larger pressure results than the approach used in the FE model because of the skin effect approximations.

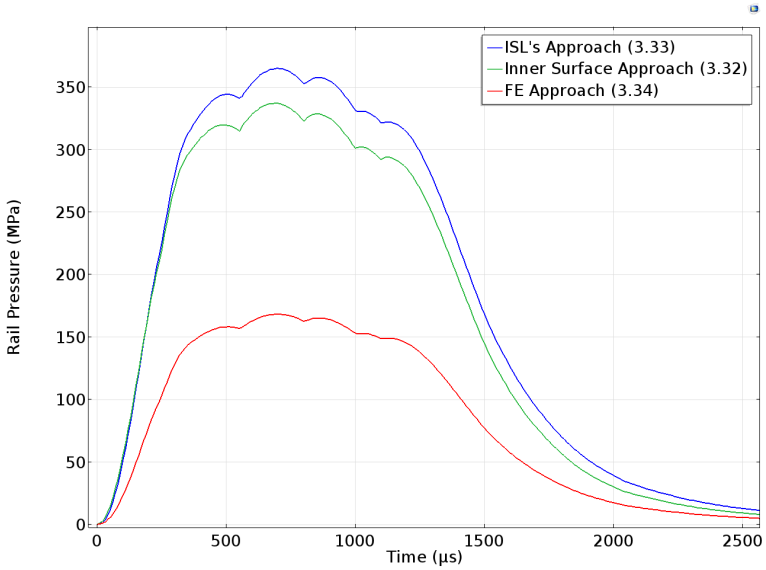

Figure 3.20: Average rail pressure in x-direction calculations using the described approaches.

Electromagnetic pressure distribution for the mesh elements in the rails are calculated using Eq. (3.35) derived from Eq. (3.27). Line integration of the force density in x-direction with constant y and z values: y_1 and z_1 gives the electromagnetic pressure value in x-direction for these constant y and z values.

$$P_x(y_1, z_1) = \int_{x_0}^{x_0+w} \vec{f}_x dx = \mu_0 \int_{x_0}^{x_0+w} [((\nabla \times \vec{H}) \times \vec{H})]_x dx \qquad (3.35)$$

Electromagnetic pressure distribution in x-direction on one rail is calculated using Eq. (3.35). The result of Eq. (3.35) for each mesh element is calculated and given in Fig.

3.21 for 0.7 ms. It can be observed that the magnitude of electromagnetic pressure acting on one rail is approximately 160 MPa aside from the rail section just behind the armature. In this part of the rail, the magnitude of electromagnetic pressure is approximately 250 MPa.

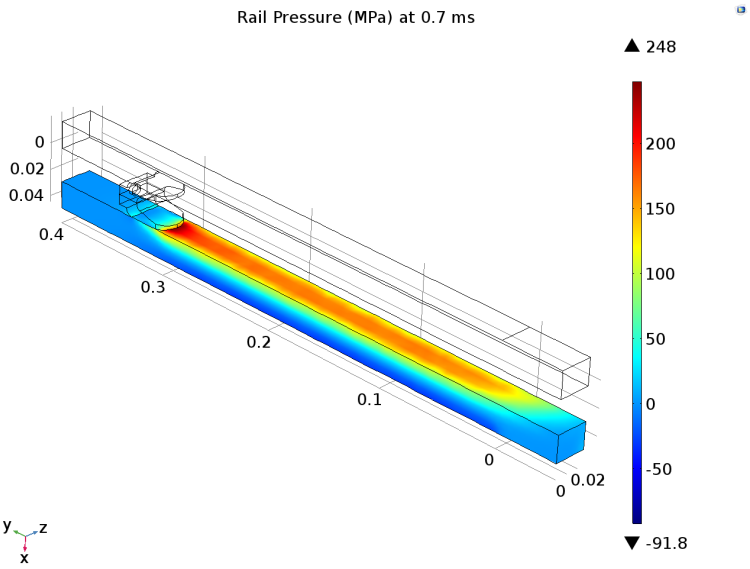

Figure 3.21: Electromagnetic pressure distribution in x-direction acting on one rail.

Effect of armature movement on the distribution of electromagnetic pressure acting on the rails can be observed from Fig. 3.22. In this figure, it can be seen that the location of the peak pressure moves with the armature. The excitation current reaches its peak value at 0.7 ms. Then, for other time instants: 1.4, 1.7 and 2.2 ms, electromagnetic pressure acting on the rails decreases as expected.

An EML can be considered as a one turn coil excited with pulsed shaped current. The total magnetic field passing through the surface between the rails is called flux linkage by definition, Eq. (3.36). In Eq. (3.36), λ is flux linkage, B is the magnetic field vector and S is the surface between two rails until the armature.

$$\lambda = \int_S \vec{B} \cdot d\vec{S} \tag{3.36}$$

Since the magnetic field between the rails depends on the magnitude of excitation current, flux linkage is also dependent of current. In Fig. 3.23, change of flux linkage with the change of current is given. The blue and red dashed areas give magnetic

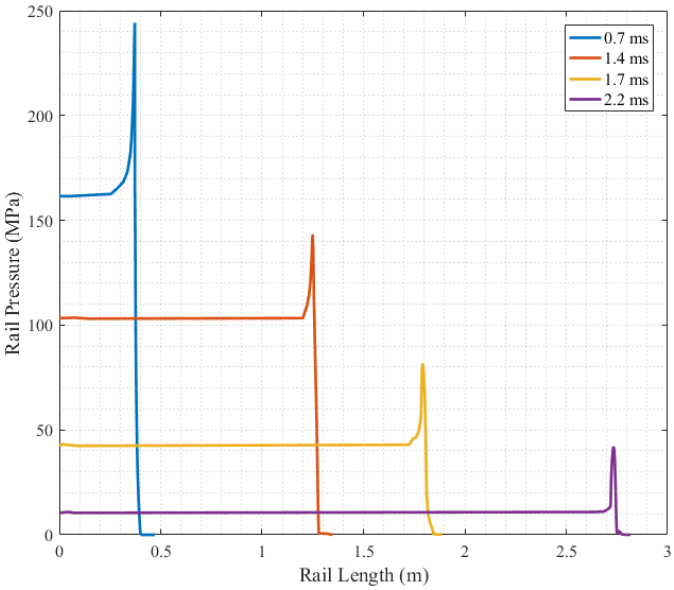

Figure 3.22: Electromagnetic pressure acting on one rail with respect to rail length for different time instants during the launch, with armature moving forward.

stored energy and coenergy respectively.

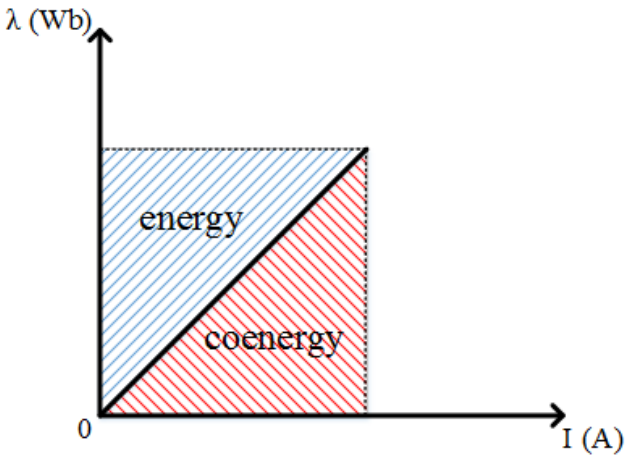

Figure 3.23: Difference between magnetic stored energy and coenergy for a linear lossless system.

As given in Eq. 3.23, in Eq. (3.37) and (3.38), equations of stored energy and co-energy in the barrel of EML are given, where W the stored energy and W′ is the

coenergy.

$$W = \int_0^{\lambda} i(\lambda) d\lambda \tag{3.37}$$

$$W' = \int_0^{i} \lambda(i) di \tag{3.38}$$

For linear lossless systems, the coenergy and stored energy is equal. Although coenergy has no physical meaning, it is useful for computing the electromagnetic force acting on the armature in acceleration direction.

Electromagnetic energy stored in the barrel of EML can be calculated using Eq. (3.39) where L is the inductance of the barrel and x is the armature position.

$$W = \frac{1}{2}\frac{\lambda^2}{L(x)} = \frac{1}{2}L(x)I^2 \tag{3.39}$$

Electromagnetic force acting on the armature in y-direction can be calculated as in Eq. (3.40) where L′ is the derivative of barrel inductance with respect to the armature position, also called inductance gradient.

$$F_{arm} = \frac{dW}{dx} = \frac{1}{2}\frac{dL(x)}{dx}I^2 = \frac{1}{2}L'I^2 \tag{3.40}$$

In Fig. 3.24, the change of electromagnetic force acting on the armature in acceleration direction with respect to time is given.

As explained in Chapter 2, friction force acting on the armature due to the contact force decreases the total force on armature in shot direction. Also, an equation for the electromagnetic component of the contact force is derived in Chapter 2 as in Eq. (3.41) where c is the length of caliber and l_{wing} is the length of armature wing.

$$F_{c_{em}} = I l_{wing}\frac{\mu_0 I}{2\pi c} = 2\ 10^{-7}\frac{l_{wing}I^2}{c} \tag{3.41}$$

For the calculation of Eq. (3.41), FEM is not required. Comparison of analytical calculation of contact force and FEM results are given in Fig. 3.25. Since the analytical

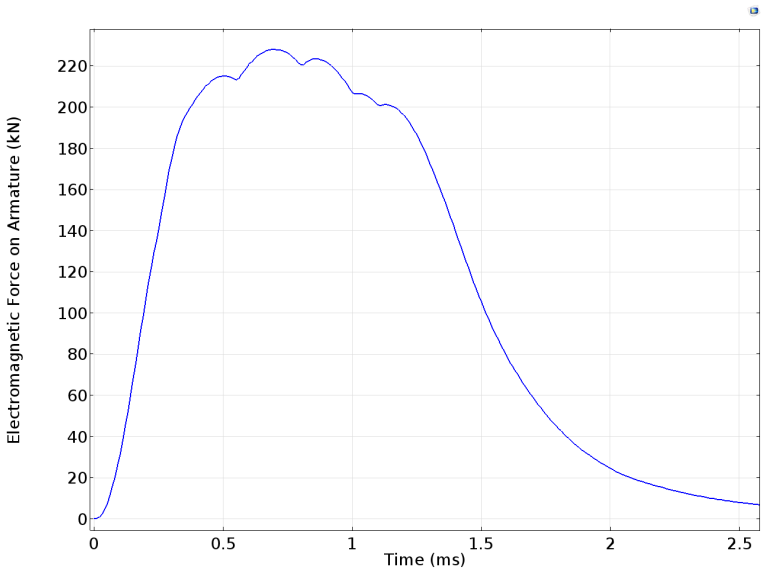

Figure 3.24: Electromagnetic force acting on the armature in shot direction during the launch.

method contains four assumptions as explained in Section 2.3, calculation of contact resistance using FEM is more realistic than the analytical method.

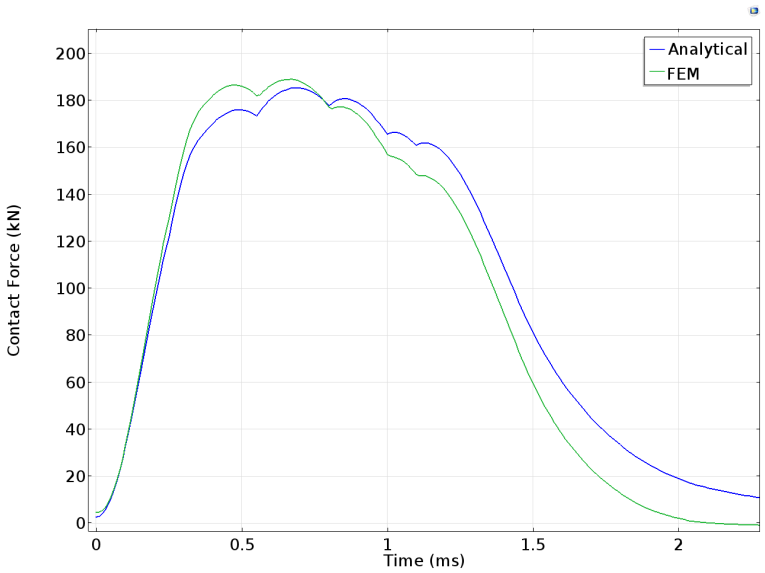

Figure 3.25: Electromagnetic component of contact for using Eq. (3.41) and FEM.

Also, frictional force can be calculated using Eq. (3.42) where $\mu(v)$ is the velocity dependent dynamic friction coefficient. The derivation for dynamic friction coefficient

is given in Chapter 2.

$$F_{fric} = 2\,F_c(t)\,\mu(v) \tag{3.42}$$

Net force acting on the armature can be calculated by subtracting the frictional force from the electromagnetic force, as in Eq. (3.43).

$$F_{net} = F_{arm} - F_{fric} \tag{3.43}$$

In Fig. 3.26, the electromagnetic, friction force acting on the armature is given with the total net force.

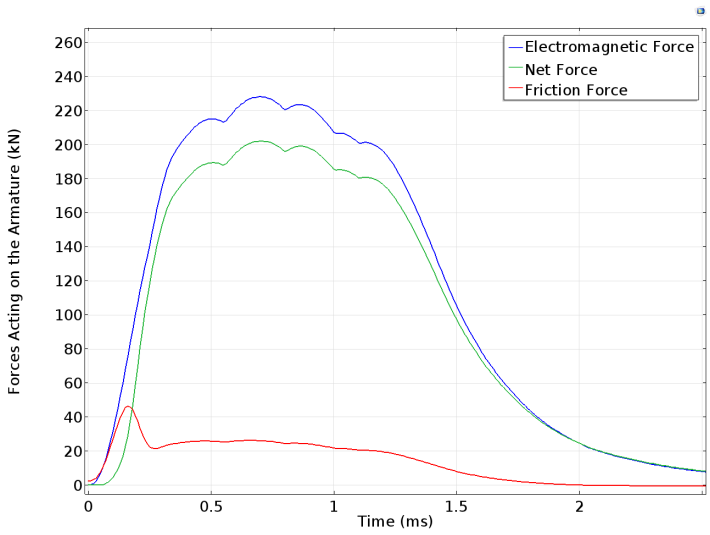

Figure 3.26: Electromagnetic, friction and net force acting on the armature.

Force density distribution in the armature can be calculated using Eq. (3.27) like the one in rails. Moreover, using force density distribution in the armature, the electromagnetic pressure distribution in shot direction can be obtained. In Fig. 3.27, pressure distribution in the armature in acceleration direction is given.

The calculation of the inductance gradient is significant in order to get the equations of motion. To derive the inductance gradient formula, let us start with the inductance calculation. By definition, inductance is the total magnetic flux linkage which can be created through a coil with 1 A current excitation. Therefore, it is possible to express

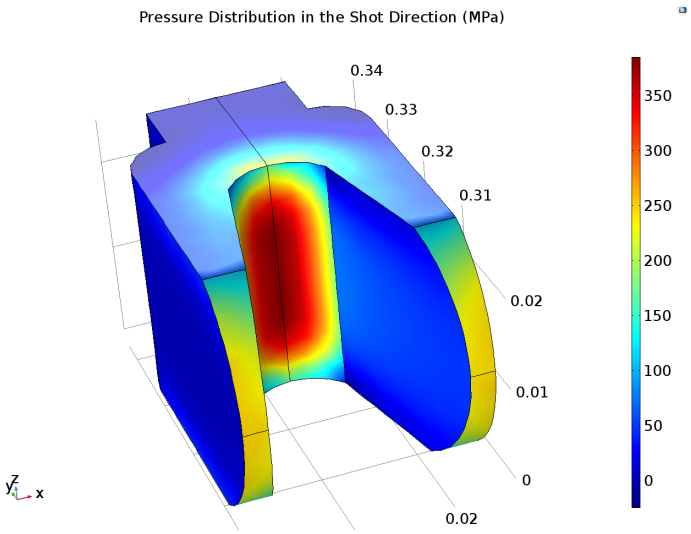

Figure 3.27: Electromagnetic pressure distribution in the armature in shot direction.

the inductance of EML barrel as in Eq. (3.44) where λ is total magnetic flux, N is the number of turns which is equal to one, ϕ is magnetic flux, B is magnetic field and S is the area between two rails and armature. Area S lies on xy-plane in the FE model.

$$L = \frac{\lambda}{I} = \frac{N\phi}{I} = \frac{\phi}{I} = \frac{1}{I}\int_S B_z(x,y)dS \tag{3.44}$$

Eq. (3.45) can be obtained by putting the boundary values of the area S.

$$L = \frac{1}{I}\int_0^{x_{preload}+x_{arm}(t)} \int_{x_1}^{x_2} B_z(x,y)dxdy \tag{3.45}$$

In Eq. (3.45), boundary of y-axis, which is the armature acceleration direction, is from the excitation bus-bars: y=0 to position of armature: $y=x_{preload}+x_{arm}(t)$. Moreover, the boundary of x-axis is from the point where the magnetic flux density is zero in one rail: x_1 to the one in the other rail: x_2. It is important to note that, in order to calculate the barrel inductance, z component of the magnetic field ($B_z(x,y)$), which is perpendicular to the xy-plane, has to be integrated through the defined area S.

Although the boundary of y-axis can be calculated analytically, the one for x-axis can be obtained only with numerical calculations. The line view of integration surface on xz-plane can be found in Fig. 3.28. Integration has to be implemented where the

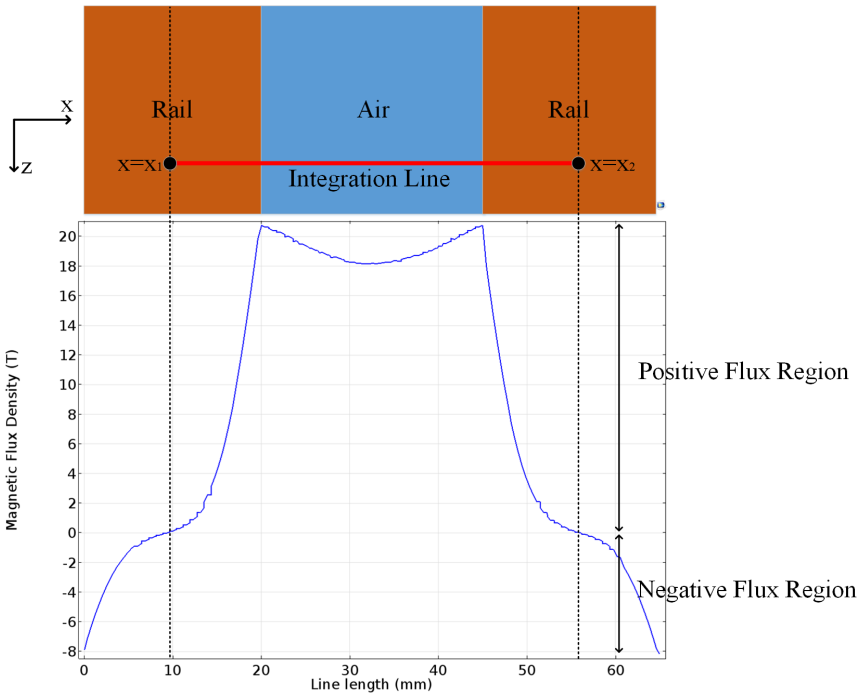

Figure 3.28: Line view of integration surface on xy-plane.

direction of the flux linkage is positive. Red line in Fig. 3.28 represents the integration line.

If it is assumed that the result of magnetic field integration through the line in Fig. 3.28 is the same for every y values which are in the range of $0<y<x_{preload}+x_{arm}(t)$, Eq. (3.45) can be modified to Eq. (3.46).

$$L = \frac{1}{I}(x_{preload} + x_{arm}(t)) \int_{x_1}^{x_2} B_z(x, y)dx \tag{3.46}$$

As explained above, the inductance gradient is the derivative of barrel inductance with respect to armature position. In other words, inductance gradient is equal to the inductance of barrel for 1 m armature position. Final equation for the inductance gradient is given in Eq. (3.47). It is important to note that x_1 and x_2 are defined in Fig. 3.28. Also, their values depends on the frequency of the excitation current. Inductance gradient is calculated as approximately 0.45 μH/m.

$$L' = \frac{1}{I} \int_{x_1}^{x_2} B_z(x)dx \tag{3.47}$$

3.4 Kinematic Results

In this section, the results of kinematic equations will be presented. The net force acting on the armature was calculated in Section 3.3. The change of armature acceleration can be found using Eq. (3.48) where a is the acceleration, m is the total mass which is chosen as 0.125 kg in this study and F_{net} is the net force acting on the armature.

$$a(t) = \frac{F_{net}(t)}{m} \tag{3.48}$$

Armature acceleration during the excitation is given in Fig. 3.29. Peak value is approximately 1.6 10^6 m/s^2 which is approximately 163.000 g.

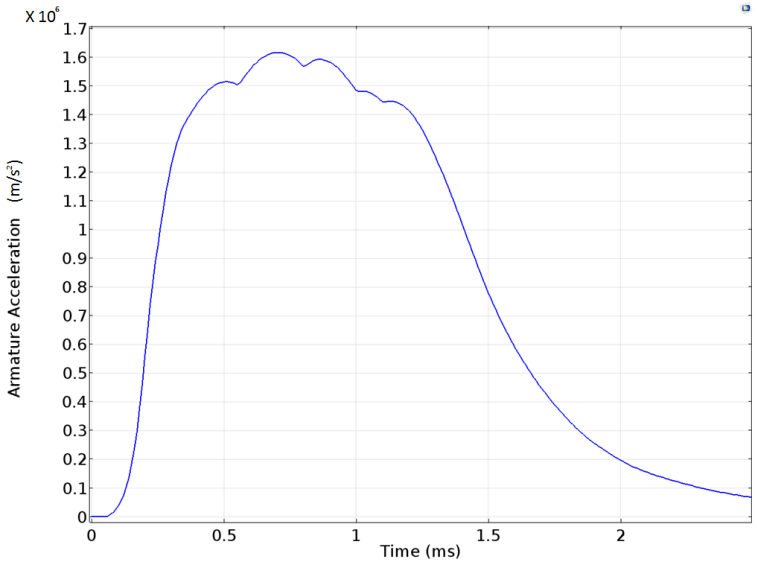

Figure 3.29: Armature acceleration.

Armature velocity can be calculated using Eq. (3.49) where v is velocity and t is time.

$$v(t) = v_0 + \int a(t)dt \tag{3.49}$$

In Fig. 3.30(a), the change of armature velocity is given. Armature position can be calculated using Eq. (3.50) where x is armature position, $x_{preload}$ is the armature position just after armature loading. In Fig. 3.30(b), the change of armature position

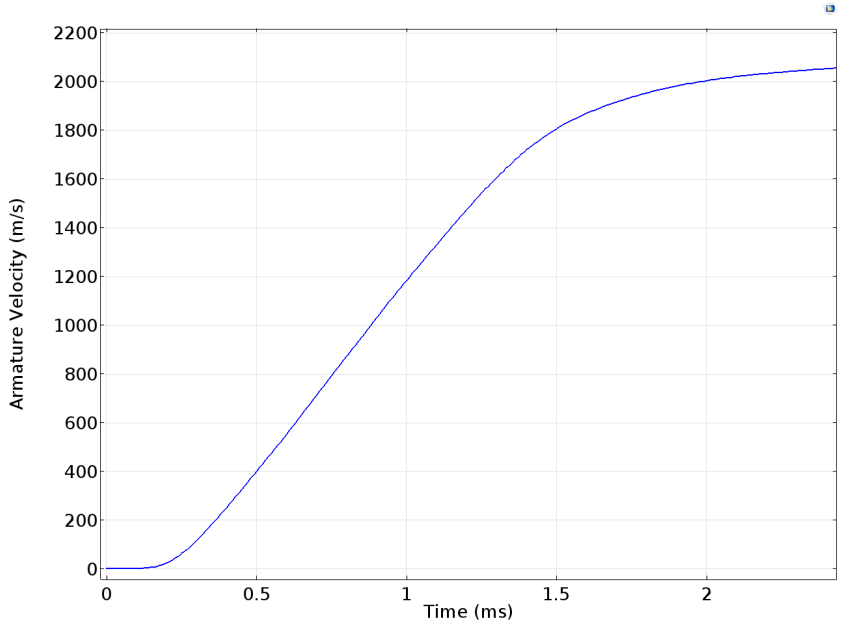

(a) Armature velocity.

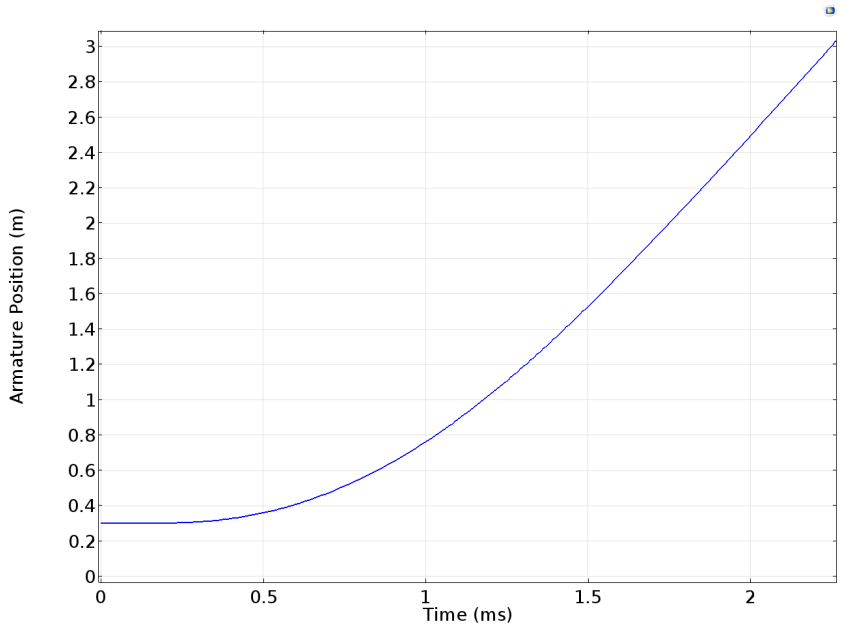

(b) Armature position.

Figure 3.30: Variation of armature velocity and position.

with respect to time is given. Initial value of the armature position is taken as 0.3 m as discussed. The armature reaches the end of the rail, 3 m, at 2.25 ms. At that instant,

the muzzle velocity is calculated as 2040 m/s from Fig. 3.30(a).

$$x(t) = x_{preload} + \int v(t)dt \tag{3.50}$$

Total kinetic energy of armature and projectile can be calculated as in Eq. (3.51). In Eq. (3.51), it is assumed that there is no melting in the armature which means that the total mass of projectile and armature does not change during the acceleration.

$$E_{kin}(t) = \frac{1}{2}mv(t)^2 \tag{3.51}$$

In Fig.3.31, the change of total kinetic energy with respect to time is given. Muzzle kinetic energy is calculated as 260 kJ. Since the initial electrical energy of the capacitive PPS is 2 MJ, total efficiency of the system is found to be 13%. Also, some critical outputs of the FE model after the calculation of kinematic equations are presented in Table 3.2.

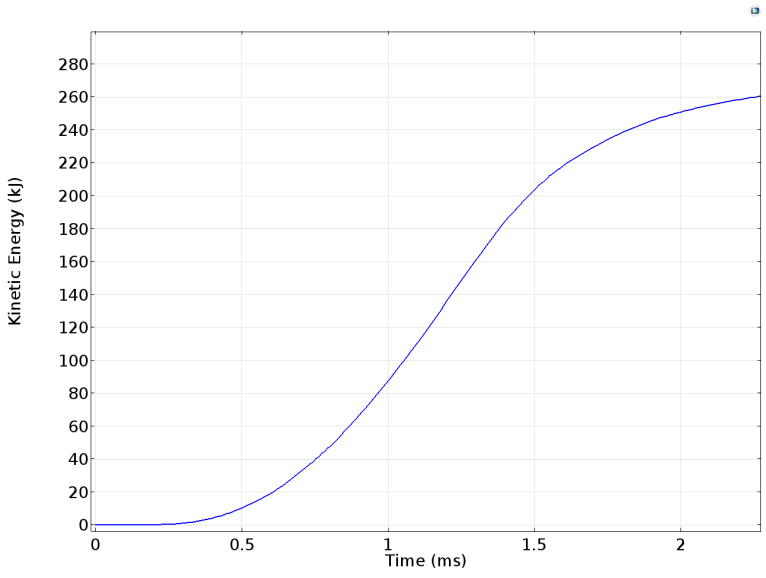

Figure 3.31: Total kinetic energy of armature and projectile.

Table 3.2: Some critical outputs of the FE simulation.

Total Mass of the Launch Package	0.125 kg
Magnitude of Current Peak	1026 kA
Inductance Gradient	0.45 μH/m
Maximum Acceleration	163 10^3 g
Muzzle Time	2.25 ms
Muzzle Velocity	2040 m/s
Muzzle Kinetic Energy	260 kJ
Efficieny of the Total System	13%

3.5 Thermal Analysis

In order to analyze the temperature change distribution after the excitation, it can be assumed that the heat generation is only considered due to the electrical resistivity as discussed in [58]. Zhao *et al.* also ignore the friction between the armature and rails the air resistance and the heat generation in the armature. In this study, heat generation in both rails and armature and friction between the armature and rails are considered in the temperature analysis. Energy equation is written in [58] as in Eq. (3.52).

$$dc\frac{\partial T}{\partial t} = \nabla \cdot (k\nabla T) + \frac{\vec{J} \cdot \vec{J}}{\sigma} \tag{3.52}$$

In Eq. (3.52), d is the density of the material [kg/m^3], c is the specific heat of the material [J/(kg·K)], T is the temperature [K], k is the thermal conductivity of the material [W/(m·K)], $\vec{J}$ is the current density vector and σ is the electrical conductivity [S/m].

Since the duration of excitation is approximately 2.5 ms, thermal conductivity term (∇·(k ∇ T)) of Eq. (3.52) can also be ignored. Then, Eq. (3.52) can be simplified to

Eq. (3.53).

$$dc\frac{\partial T}{\partial t} = \frac{\vec{J}\cdot\vec{J}}{\sigma} \tag{3.53}$$

Then, by taking the time integral of both sides, Eq. (3.54) can be obtained.

$$dc\Delta T = \int_0^{t_{muzzle}} \frac{(\sqrt{J_x^2+J_y^2+J_z^2})^2}{\sigma}dt \tag{3.54}$$

Since both armature and rails are taken into account as heat source, it is required to solve Eq. (3.54) for both aluminum and copper materials. Then, for the armature, Eq. (3.55) and for the rails, Eq. (3.56) can be written.

$$\Delta T_{arm} = \frac{1}{d_{arm}c_{arm}\sigma_{arm}}\int_0^{t_{muzzle}} (\sqrt{J_x^2+J_y^2+J_z^2})^2 dt \tag{3.55}$$

$$\Delta T_{rail} = \frac{1}{d_{rail}c_{rail}\sigma_{rail}}\int_0^{t_{muzzle}} (\sqrt{J_x^2+J_y^2+J_z^2})^2 dt \tag{3.56}$$

The heat equation constants in Eq. (3.55) and (3.56) for the armature and rail materials are given in Table 3.3

Table 3.3: Heat equation constants for rail and armature materials.

	Armature	**Rail**
Density (d)	2700 kg/m^3	8960 kg/m^3
Electric Conductivity (σ)	3.77 10^7 S/m	5.99 10^7 S/m
Specific Heat Capacity (c)	900 J/(kg·K)	385 J/(kg·K)

Eq. (3.57) and (3.58) can be obtained using the constant values in Table 3.3.

$$\Delta T_{arm} = 10.9\ 10^{-15}\int_0^{t_{muzzle}} (\sqrt{J_x^2+J_y^2+J_z^2})^2 dt \tag{3.57}$$

$$\Delta T_{rail} = 4.8\ 10^{-15}\int_0^{t_{muzzle}} (\sqrt{J_x^2+J_y^2+J_z^2})^2 dt \tag{3.58}$$

Finally, in order to obtain the temperature variation distribution in the rails and armature, Eq. (3.57) and (3.58) are solved for each mesh element in the armature and rails. The distribution is given in Fig. 3.32.

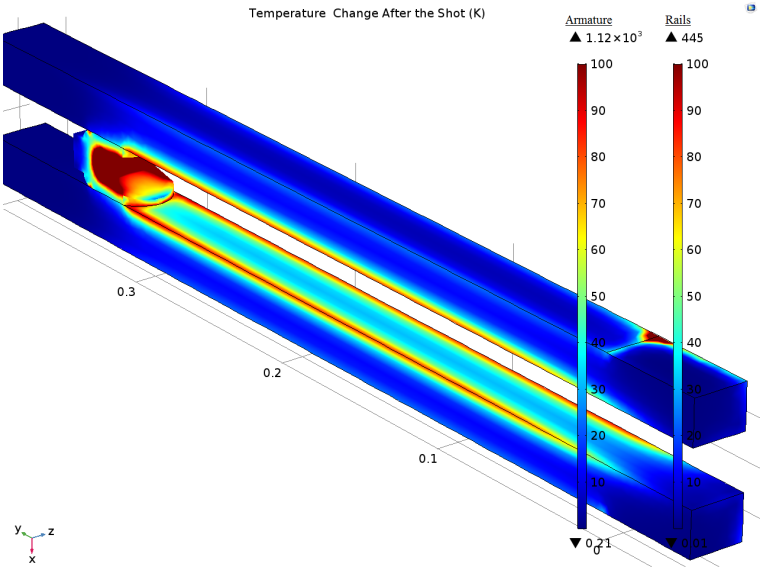

Figure 3.32: Temperature change in the armature and rails after one shot.

In Fig. 3.32, results of Eq. (3.57) and (3.58) are combined. Therefore, there are two legends in the figure, the first one is for armature and the second one is for rails. It can be observed that while the maximum temperature change in the rail volume is 445 K, it is 1120 K for the armature volume. Hence, it can be concluded that although there is no melting problem in the rails for the given shot scenario, aluminum material starts to melt during the excitation. Melting in the armature can damage the armature with large electromagnetic forces acting on it. Also, melting of aluminum material of the armature on the contact surface can cause an erosion on the rail.

3.6 Recoil Force Analysis

In order to excite the rails, there exist two busbars at the breech side of the barrel. In addition to the propulsive force acting on the armature and deflection force acting on the rails, there exist a recoil force acting on the busbars due to the conservation of momentum in reverse of the shot direction as defined in Section 1.5.4. The schema of recoil forces is given Fig. 3.33.

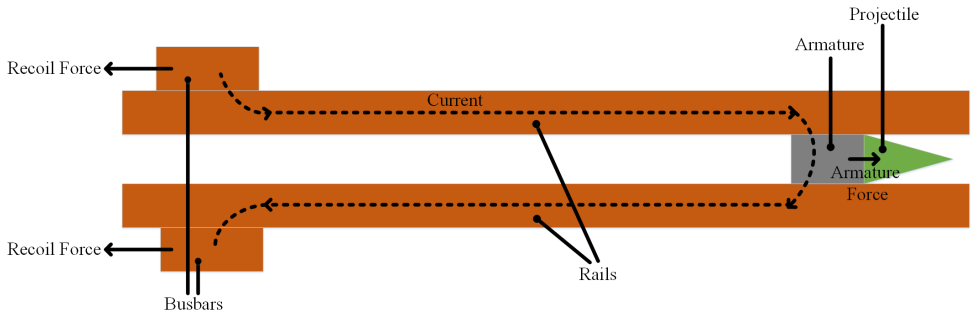

Figure 3.33: Electromagnetic recoil forces on the busbars.

Witalis proposed the idea of using coaxial cables to connect the PPS units to these basburs, [59]. Using coaxial cables to excite the busbars decreases the total force on the cables. In addition, due to the conservation of momentum, there exist electromagnetic force on the busbars called recoil force. In Fig. 3.34, the geometry of busbars and coaxial cable are presented.

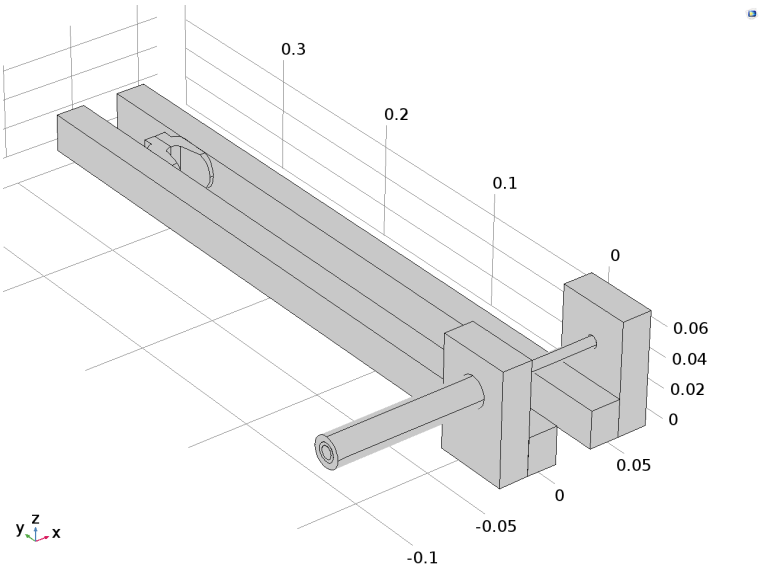

Figure 3.34: Geometry of busbars and coaxial cable.

Coaxial cables contains four parts: Outer insulator, outer conductor, inner insulator and inner conductor. In the model, while outer conductor of the coaxial cable carries the current in the -X direction, inner one carries in +X direction. Moreover, although the inner insulator has to be modeled for the insulation between conductors, it is not required to add the outer insulator to the model. In Fig. 3.35, the current density

distribution in the X-direction in conductors of the coaxial cable used in the model is given.

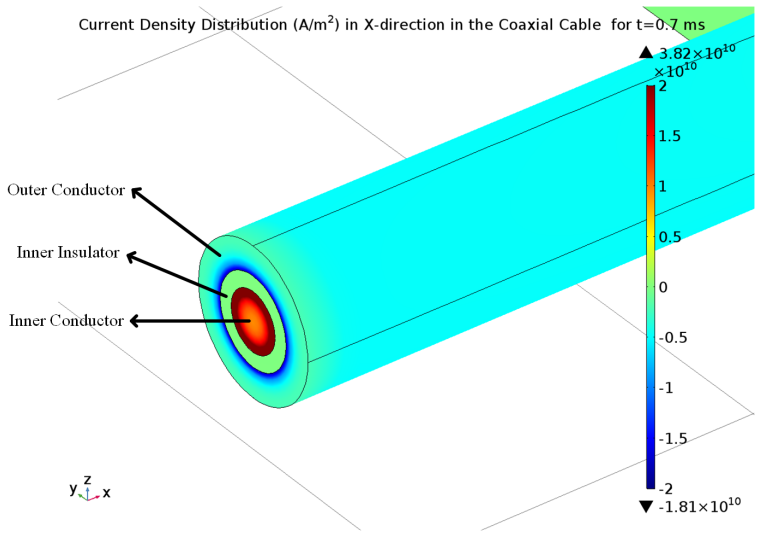

Figure 3.35: Current density distribution in X-direction in the coaxial cable at 0.7 ms.

In addition, the current density magnitude distribution and the current density vectors in the busbars, rails and armature are given in Fig. 3.36.

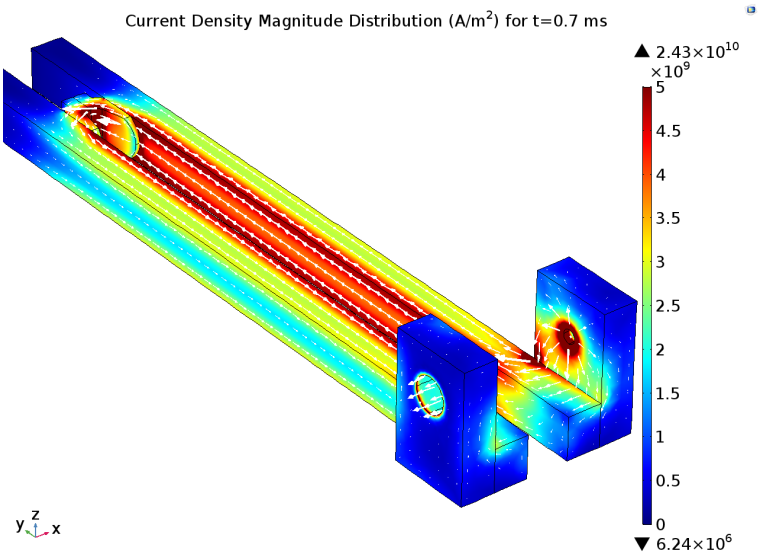

Figure 3.36: Normalized current density distribution and the current density vectors in the busbars, rail and armature.

Although the recoil force is created according to conservation of momentum, Schneider *et al.* conclude that the intuitive action-reaction considering, $J_{rail} \times B_{arm}$, does

not work at all for the calculation of the recoil forces, in [60]. Estimation of the location and magnitude of the recoil forces is very hot topics in the literature, [61] and [62]. The common conclusions are the fact that recoil force is created in the fixed connection part in the breech side, the direction of the recoil force is in the opposite direction with the one acting on the armature, and its value is not necessarily equal to the armature force. It means that the recoil and the armature forces are not the interaction forces. Therefore, using FEM to calculate recoil is a reasonable idea.

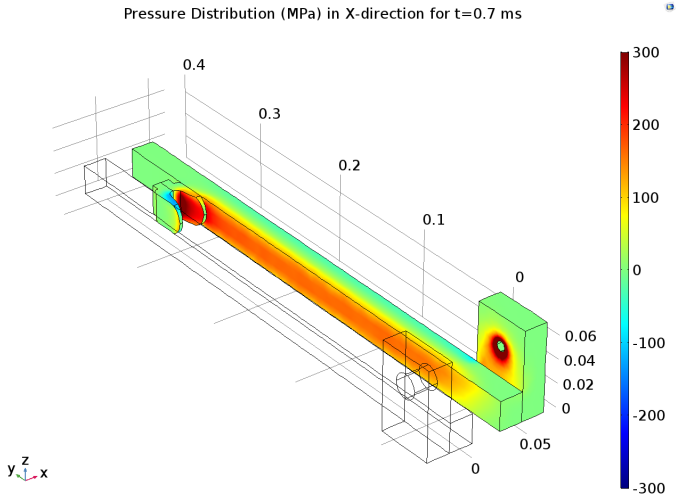

(a) Electromagnetic pressure in X-direction.

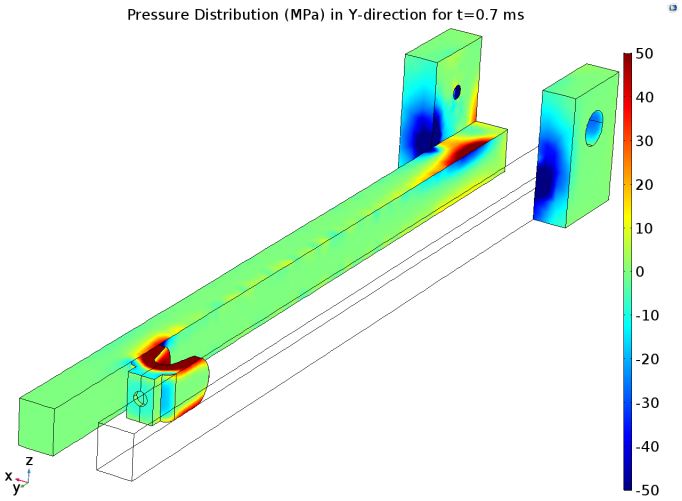

(b) Electromagnetic pressure in Y-direction.

Figure 3.37: Electromagnetic pressure distribution in the armature, rail and busbar in X and Y-direction at 0.7 ms.

In Fig. 3.37, the electromagnetic pressure distributions in the armature, rail and busbar in the X and the Y directions are given for t=0.7 ms. Fig. 3.37(b) shows that most of the recoil forces acting on the busbars are created around the connection of the busbars and rails.

In Fig. 3.38, the comparison of the total electromagnetic forces in Y-direction acting on the armature, rails and busbars is given. Although the direction of current density vectors in X-axis are the same in both rail and busbar, the direction of magnetic field in Z-direction are opposite in rail and busbar. Therefore, although the recoil force is negative in Fig. 3.38, rail force is positive. Moreover, it can be observed that the summation of electromagnetic forces presented in Fig. 3.38 is not equal to zero due to the recoil forces acting on the cables which are connected to the busbars.

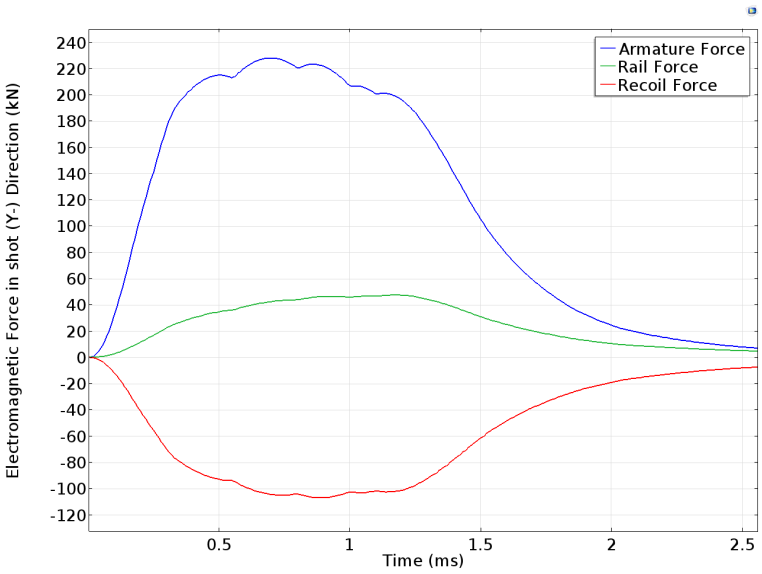

Figure 3.38: Electromagnetic forces in Y-direction acting on the armature, rails and busbars.

In this chapter, the significant results of the developed FE model were presented. In Chapter 4, two critical parts of the EML: containment and armature will be analyzed in detail. In Section 4.1, the difference of laminated and solid containment will be discussed in terms of their eddy current losses. Also, the effect of lamination thickness on the muzzle kinetic energy will be presented using FEM. In Section 4.2, the geometry of the armature will be optimized using genetic algorithm (GA). Then, the effect of geometric parameters of the armature on the muzzle kinetic energy, contact

current distribution between the rails and armature and damaging electromagnetic force acting on the armature will be discussed.

CHAPTER 4

IMPROVEMENTS ON THE CONTAINMENT AND ARMATURE STRUCTURE

In this chapter, two critical improvement studies for the barrel side of an EML will be presented in detail: lamination of the containment and optimization of the armature shape. In Section 4.1, geometry of the proposed containment will be described. Then, the difference between the solid and laminated containment will be presented. Finally, the effect of lamination thickness of the containment on the armature force, muzzle velocity, average rail pressure and the total electromagnetic force acting on the containment will be discussed. The study in this section was published in 18th International Symposium on Electromagnetic Fields in Mechatronics, Electrical and Electronic Engineering, [38]. Then, in Section 4.2, armature geometry optimization study, published in IEEE Transactions on Plasma Science, [53] , will be presented. In this study, armature shape is optimized in order to maximize the muzzle kinetic energy including contact resistance modeling. Constraints of the optimization study is maximum contact current density and damaging electromagnetic pressure acting on the armature limbs constraints.

4.1 Effect of Laminated the Containment on the Efficiency

During the excitation of an EML, in addition to the electromagnetic force acting on the armature, electromagnetic deflection forces are created on the rails as in Fig. 4.1. Because of these deflection forces, rails repel each other. These forces may cause the loss of contact between the rails and armature. Hence, mechanical support around the rails in order not to lose the contact is a requirement for EMLs. To support the

rails mechanically with metal containment is a widely used method in EML technology, as in [63–66]. Although using metal containment close to rails is a critical issue for electromagnetic launchers in terms of mechanical requirements, existence of the containment negatively affects the system in terms of electromagnetic perspective. During this study, the electromagnetic effect of conducting metal containment is investigated for Tufan EML. The digest of this study is published as [38]. The extended version of this study is explained in this Section.

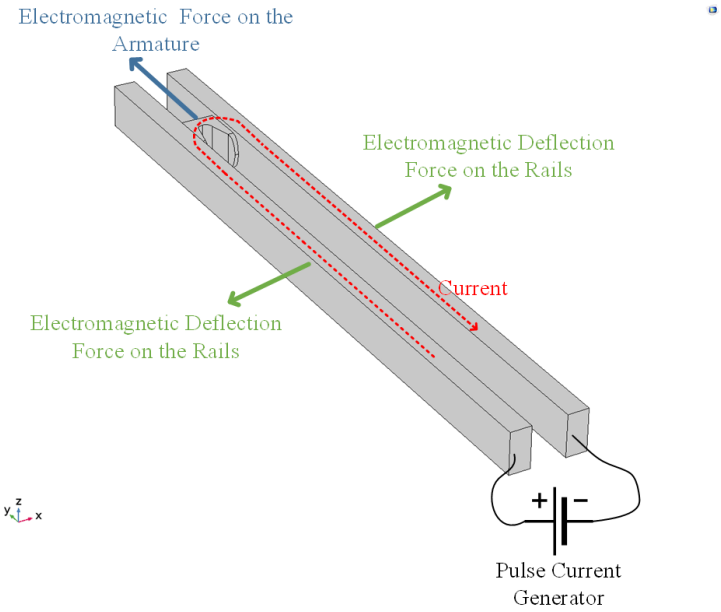

Figure 4.1: Electromagnetic forces on the armature and rails, [38].

Rapid change of magnetic field during the firing creates an induced electromotive force in compliance with Lenz's Law. Induced eddy current in the containment tends to resist the change of magnetic field, which is the reason of minus sign in Lenz's Law. Moreover, the eddy current causes power dissipation in the containment core as given in Eq. (4.1).

$$P = \frac{V \pi^2 B_{peak}^2 d^2 f^2}{k\ \rho} \tag{4.1}$$

Note that, in Eq. (4.1), V is the volume of the containment, B_{peak} is the peak magnetic field, d is the density of the containment material, f is the frequency, k is the constant and ρ is the resistivity of containment.

Eq. (4.1) shows that dissipated power in the metal containment is related with the square of frequency and maximum magnetic field value. Hence, the magnitudes of eddy currents induced in containment are not the same during current rise and fall intervals. Also, its direction reverses while the current decreases.

One way to reduce the eddy current losses in the containment is to use laminated metal sheets. At this point, the lamination thickness becomes a significant parameter which determines the amount of eddy current loss. However, making laminations too thin reduces mechanical endurance and complicates the manufacturing. Core loss in the containment reduces the muzzle kinetic energy of the railgun as presented in [64]. In [36], Parker et al. proposed a containment design for the medium caliber launcher with steel laminations. Although change of propulsive inductance gradient with respect to armature-to-containment gap is investigated in this study, effect of lamination thickness on the efficiency of energy conversion is not covered.

In this study, external pulse current excitation with 1.5MA peak is applied to 3D stationary railgun FE model. Also, to reduce the computation time, quarter symmetry property of the model is used. In Fig. 4.2, 2D view of launcher and containment is given. Externally applied pulse current is generated by firing more than one pulse power supply at different instants to keep the current around its peak value longer.

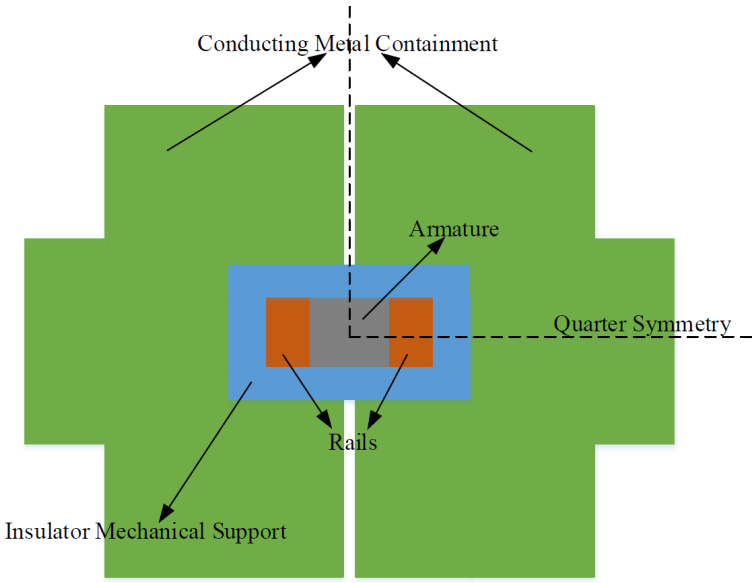

Figure 4.2: Sectional view of laminated containment model, [38].

In order to analyze the effect of containment lamination on the efficiency of the system, lamination thicknesses of 5, 10, 30, 50, and 100 mm are simulated in addition to the solid stainless steel containment. The stacking factor was chosen as 97% for each laminated containment. Instead of anisotropic conductivity method in [67] and [68], actual laminated sheets and air gap geometries are created in COMSOL Multiphysics FEM software. Although it increases the computation time, using the lamination sheets and insulation layers in the FEM model is plausible, to observe the exact distribution of the eddy currents in the containment.

The material of the conducting containment is another significant parameter that effects the efficiency of the launcher. In this study stainless steel is chosen as the metal material for the containment. Relative permeability (μ_r) of the chosen stainless steel is approximately one which means it is non-magnetic.

4.1.1 Eddy Current Distribution in the Metal Containment

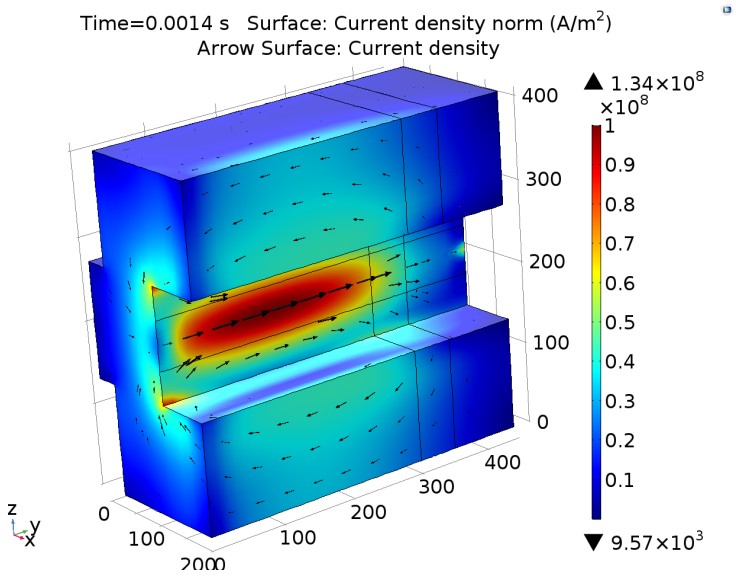

Figure 4.3: Magnitude and direction of eddy current in the solid containment during the current rising.

The time derivative of magnetic flux determines the direction of the eddy current. Frequency and peak magnetic field determine the magnitude of the eddy currents. In Fig. 4.3, eddy current density vectors induced in the solid containment and magnitudes are

given for the current rise time. Note that for the current fall time, its direction will be reversed as explained in [37].

In Fig. 4.3, only left part of the solid containment without any lamination is shown. From the figure, one can observe that the magnitude of the current density is largest in the surface facing the rail. Also, eddy currents are induced in the containment from the excitation terminal to the position of the armature: 0.3 m. For the rails beyond the position of the armature, there is almost no induced eddy current in the metal containment as expected.

In the FE simulation, armature is held steady in the position of 0.3 m from the excitation side of the rails. In Fig. 4.4, eddy current density distribution on a XZ cut plane of the solid containment is given. The cut plane is placed where Y=0.15 m.

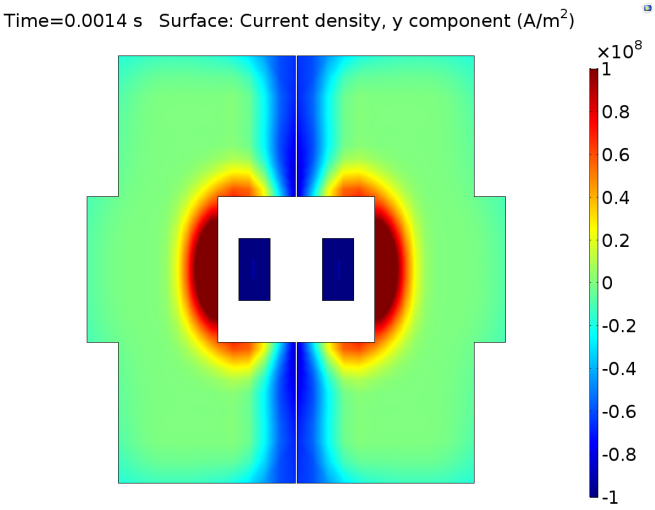

Figure 4.4: Eddy current density distribution on a XZ cut plane of the solid containment and the rails.

In addition to the solid metal containment which causes larger induced current density in the containment, laminated containment is investigated in the study. In Fig. 4.5, current density distribution in a single lamination sheet for the 10 mm lamination thickness case is given.

While the maximum current density due to the eddy current is 134 A/mm^2 for the solid containment, it is reduced with 10 mm lamination to 9 A/mm^2. As a result, the core loss in the containment is reduced.

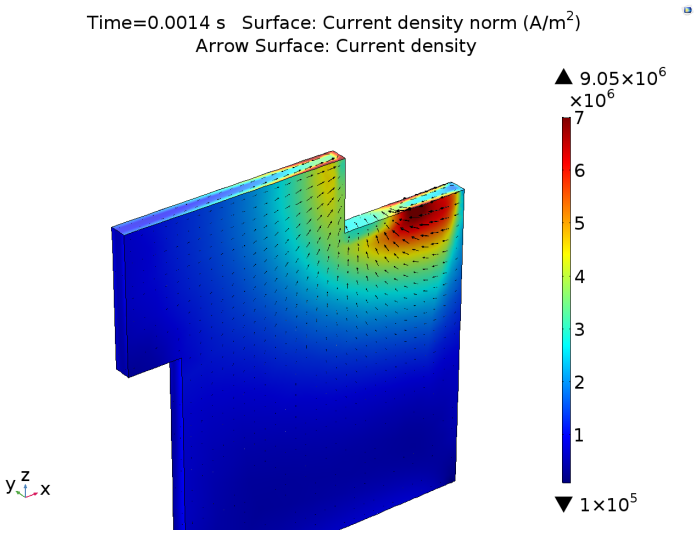

Figure 4.5: Magnitude and direction of eddy current in one lamination sheet of the laminated containment during the current rising.

4.1.2 Effect of Lamination on the Armature Force and Velocity

EML with solid laminated containment will be compared with respect to the electromagnetic force acting on the armature. In Fig. 4.6, effect of lamination thickness on the armature repulsive force is given.

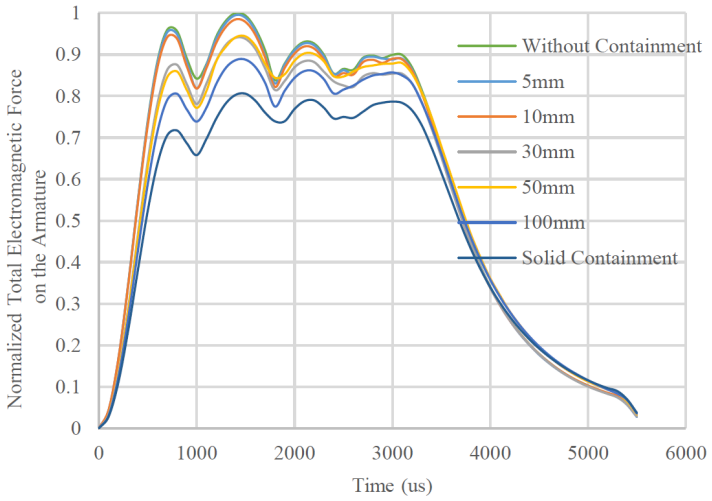

Figure 4.6: Change of armature repulsive force for different lamination thicknesses.

Electromagnetic launcher without any containment, which is not reasonable according to mechanical concerns, has the largest electromagnetic repulsive force on the ar-

mature. While the containment with 5 and 10 mm lamination sheets have negligible negative effect on the armature repulsive force, other lamination strategies decreases the armature force with respect to no containment case.

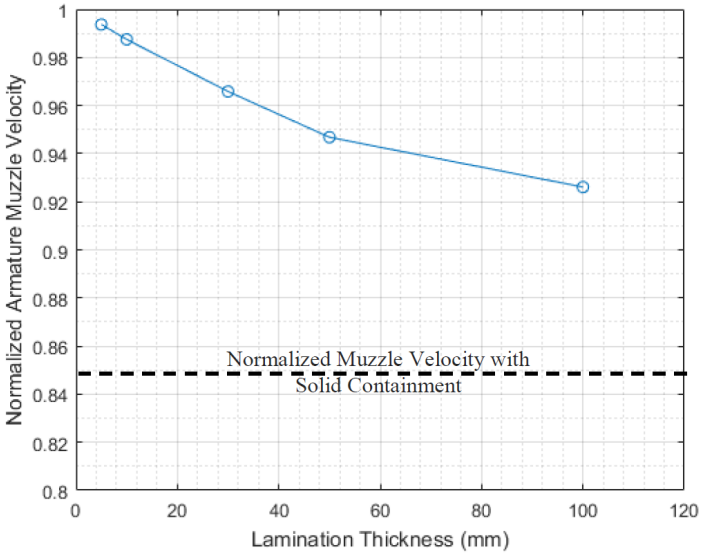

(a) Muzzle velocity.

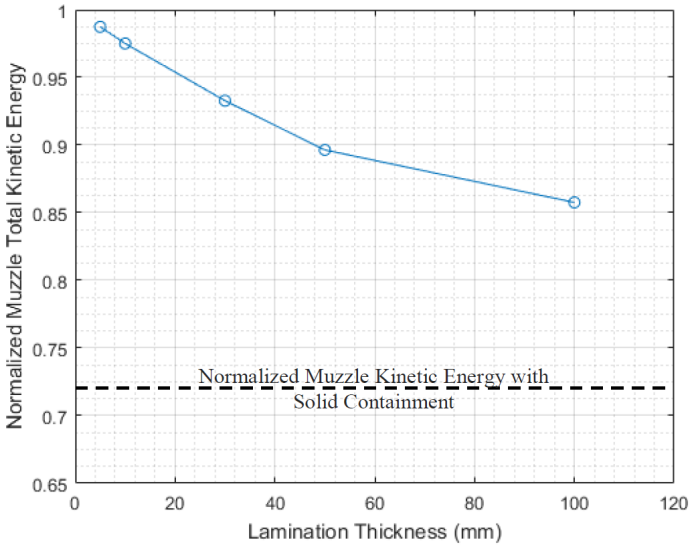

(b) Muzzle kinetic energy

Figure 4.7: Effect of lamination thickness on the armature muzzle velocity and kinetic energy.

Armature force reduction affects the armature muzzle velocity. Fig. 4.7a shows the change of normalized muzzle velocity for different lamination sheet thicknesses. Armature muzzle velocity of launcher without any containment is calculated as 1600 m/s

(note that friction force and contact resistance are neglected). It is shown as unity in order to calculate the normalized muzzle velocities for different lamination thicknesses. Then the comparison of ratio of muzzle velocities of launcher with other lamination thicknesses over muzzle velocity of launcher without any containment is given in Fig. 4.7a. One can observe that solid containment decreases the normalized muzzle velocity to 0.85. In addition to normalized muzzle velocity comparison, effect of lamination thicknesses on the normalized total muzzle kinetic energy is given in Fig. 4.7b. Note that solid containment decreases the normalized muzzle velocity down to 0.72.

4.1.3 Effect of Lamination on the Average Rail Pressure

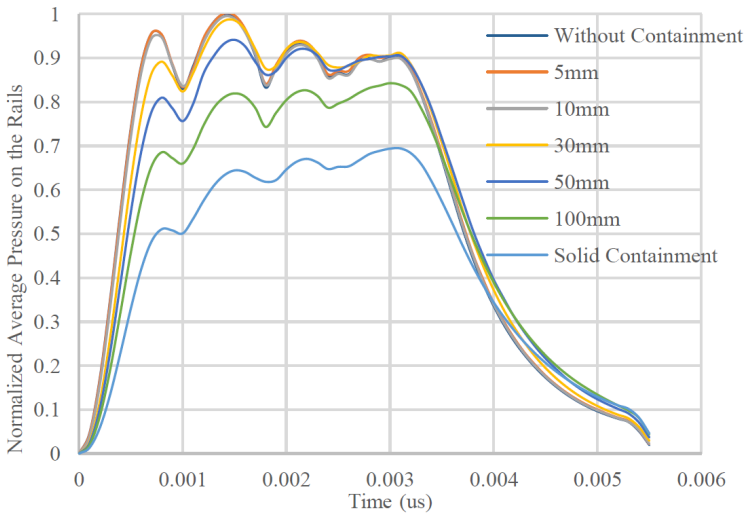

Figure 4.8: Effect of lamination thickness on the average pressure acting on single rail.

During the excitation, in addition to the armature repulsive force, electromagnetic deflection force acting on the rails, shown in Fig. 4.1, should be taken into account. In addition to the geometric parameters such as rail-to-rail distance (caliber), armature shape, and rail thickness, containment lamination also affects the average pressure on the rails, see [69]. This effect is directly related with the derivative of the current waveform with respect to time. From Fig. 4.8, one can observe that addition of a containment decreases the average rail pressure because of the eddy current loss in

the containment. Also, its impact is larger for the time interval of the current rising, since the first derivative of the current is larger in this interval, which creates larger eddy current loss in the containment.

4.1.4 Effect of Lamination on the Containment Force

Eddy current and magnetic field in the containment creates an electromagnetic force on the containment in the X direction. In this part of the study, half symmetry model of the containment is analyzed to observe the effect of the lamination thickness on the total electromagnetic force. As shown in Fig. 4.9, maximum force acting on the containment is created for the case of solid containment, since the magnitude of eddy current is larger for this case. It should be noted that, for different lamination thicknesses, the direction of the force acting on the containment changes at different instants when the direction of the eddy current induced in the containment changes during the excitation.

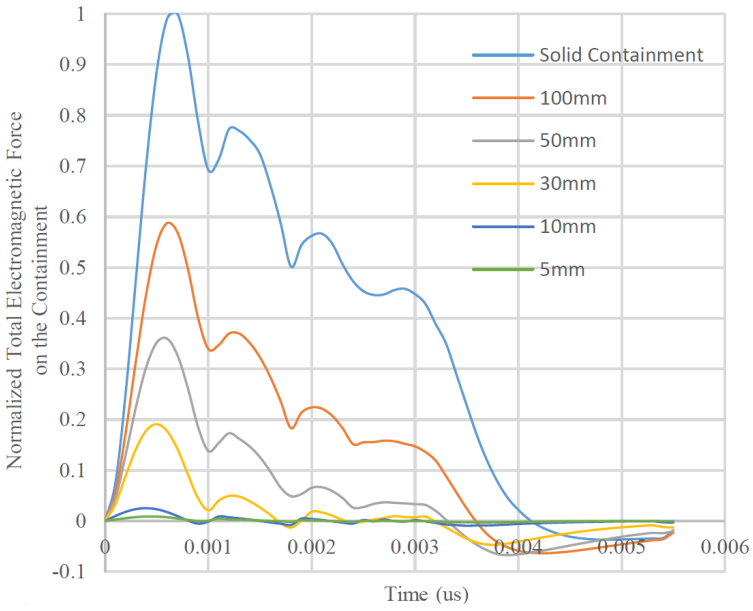

Figure 4.9: Effect of lamination thickness on the total electromagnetic force in the X-direction.

During the design process of an EML, effect of the conducting containment has to be taken into account as it affects the armature muzzle velocity and kinetic energy. In

Table 4.1, the influence of the lamination thickness on the muzzle velocity and kinetic energy is given.

Table 4.1: The influence of the lamination thickness on the normalized muzzle velocity and kinetic energy.

Lamination Thickness (mm)	**Normalized Muzzle Velocity**	**Normalized Muzzle Kinetic Energy**
Air Cored	1	1
5	0.99	0.99
10	0.99	0.98
30	0.97	0.94
50	0.95	0.90
100	0.93	0.87
Solid	0.85	0.72

To sum up, 10 mm lamination sheet thickness is observed to be a critical value for armature muzzle velocity and kinetic energy. Also, the worst case according to muzzle velocity and kinetic energy is solid conducting containment without any lamination. In addition to the muzzle velocity and kinetic energy, containment lamination thickness also affects the pressure on the rail and the force acting on the containment. For the solid containment case, the peak value of the normalized force acting on the containment is unity while it is 0.01 for the laminated containment with 5 mm lamination thickness case as can be observed from Fig. 4.9. Moreover, using lamination in the metal containment increases the pressure on the rails in X direction. For air cored and laminated EMLs with 5 and 10 mm thicknesses, applied current results unity average pressure on the rails while for the solid containment case, the average pressure on the rails is approximately 0.65 at the same instant. Although from the electromagnetic point of view, the smaller lamination thickness provides the larger efficiency, mechanical endurance of the containment decreases with the decrease of the lamination thickness. Since decreasing the lamination thickness smaller than 10 mm does not effect the electromagnetic parameters discussed in the study significantly, the study shows that 10 mm is the most reasonable lamination thickness for the EML analyzed

in this study.

4.2 Armature Shape Optimization

In order to create maximum muzzle kinetic energy using the same amount of electrical energy, a number of parameters both in the barrel side and the pulse power supply should be carefully considered. In particular, the armature shape plays a key role in achieving a high efficiency. In Tufan EML, C-shaped solid armature is used. In this part of the thesis, shape of the solid armature will be discussed. This study is published in IEEE Transactions on Plasma Science, [53].

4.2.1 Properties of the EML Used in the Optimization Study

PEGASUS EML described in [70] is used for the optimization study instead of Tufan due to the confidentiality agreement with ASELSAN Inc. Therefore, the height and width of the rails, caliber, projectile mass and current waveform are taken constant from [70] as in Tab 4.2. Since solving the FE model in the optimization algorithm is time consuming, current excitation is used instead of voltage excitation which means there is no pulse power supply in the FE model. Also, the current waveform is simplified as in Fig 4.10.

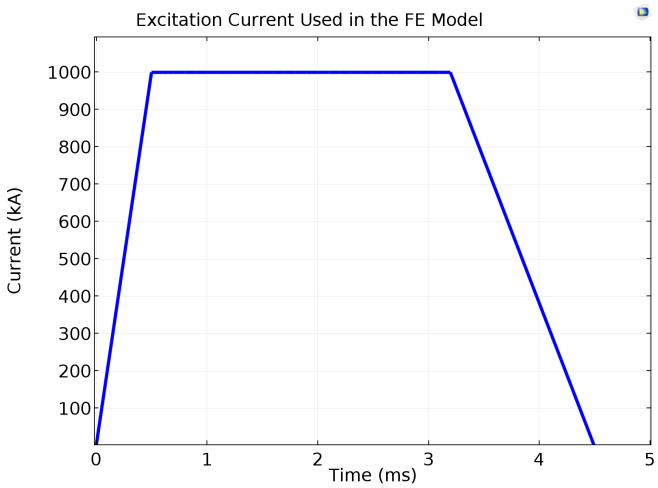

Figure 4.10: Excitation current waveform used in FEM, [53].

Table 4.2: Constant EML parameters for the armature shape optimization, [70].

Height of the Rails	40 mm
Width of the Rails	30 mm
Caliber Dimensions	40x40 mm
Mass of Projectile	300 g

4.2.2 Optimization Parameters

The optimization parameters that present the exact geometry of the armature is given in Fig. 4.11. Since the caliber is constant, x_3 is a dependent factor of x_1 and x_2. Therefore, although in the figure there exist six variables, there are five independent variables that define the geometry of the armature.

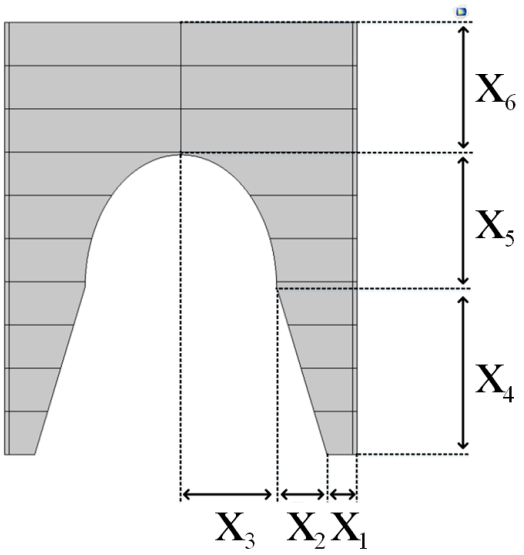

Figure 4.11: Armature shape optimization parameters, [53].

4.2.3 Objective Function, Constraints and Penalty Parameters

In the optimization study, the objective function is the projectile muzzle kinetic energy that is desired to be maximized. Moreover, the constraints are the maximum pressure on the contact surface, maximum pressure on the inner surface and the max-

imum current density on the contact surface. In Eq. (4.2), the equation used in the optimization for the objective function is given.

$$\begin{aligned} Obj(x_n) &= \hat{E}_p(x_n) - C_1(x_n) - C_2(x_n) - C_3(x_n) \\ C_1(x_n) &= P_1 * max\left\{0, (\hat{J}_{cont} - \hat{J}_{cri})\right\} \\ C_2(x_n) &= P_2 * max\left\{0, (\hat{P}_{cont} - \hat{P}_{cri})\right\} \\ C_3(x_n) &= P_3 * max\left\{0, (\hat{P}_{in} - \hat{P}_{cri})\right\} \end{aligned} \tag{4.2}$$

In Eq. (4.2), $Obj(x_n)$ is the objective function. $\hat{E}_p(x_n)$ is normalized value of muzzle kinetic energy of the projectile, $\hat{J}_{cont}$ is normalized value of maximum current density on the contact surface, $\hat{J}_{cri}$ is normalized value of critical current density which causes the contact surface to start melting on the contact surface, $\hat{P}_{cont}$ and $\hat{P}_{in}$ are normalized values of maximum electromagnetic pressure on the contact and inner surfaces of the armature respectively, $\hat{P}_{cri}$ is normalized value of critical pressure value for the two surfaces. If the current density and the pressure values are smaller than the critical values, penalty function does not have any effect on the objective function. If one of them is greater than the critical value, it starts to reduce the value of objective function. The amount of this decrease is determined by penalty parameters: P_1, P_2, and P_3. Since the armature melting on the contact surface damages the rail surface and affects the next round of shot, it is intolerable. Therefore, P_1 is chosen as 100 to emphasize this constraint. On the one hand selecting P_2 and P_3 large can cause the objective function to converge to a value with a small muzzle energy, but on the other hand selecting these penalty parameters too small can result in a decrease the effect of pressure penalty. Therefore, P_2 and P_3 are chosen relatively small value: 2.

In order to reduce the maximum electromagnetic pressure on the contact and inner surfaces of the armature, the critical value for the pressure constraint is chosen as 100 MPa with a small penalty parameter. Since the penalty parameter of the maximum current density on the contact surface is much larger than the one for the pressure, it is crucial to estimate the critical value of the critical current density on the contact surface in order not to melt the aluminum material of the armature. In the following part of this subsection, the determination of the critical current density value will be discussed.

Since it is too time consuming to calculate the temperature change for each mesh element of each armature shape, it is assumed that the position of the maximum current point on the contact surface does not change during the excitation. The melting constraint is checked only for that part of the contact surface. The change of the place of the maximum current point is given when the magnitude of the excitation current is equal to its peak value is given in Fig. 4.12 in order to show that the assumption is true. Hence, a critical value for the contact current density which melt the unit volume of the aluminum is calculated with this assumption.

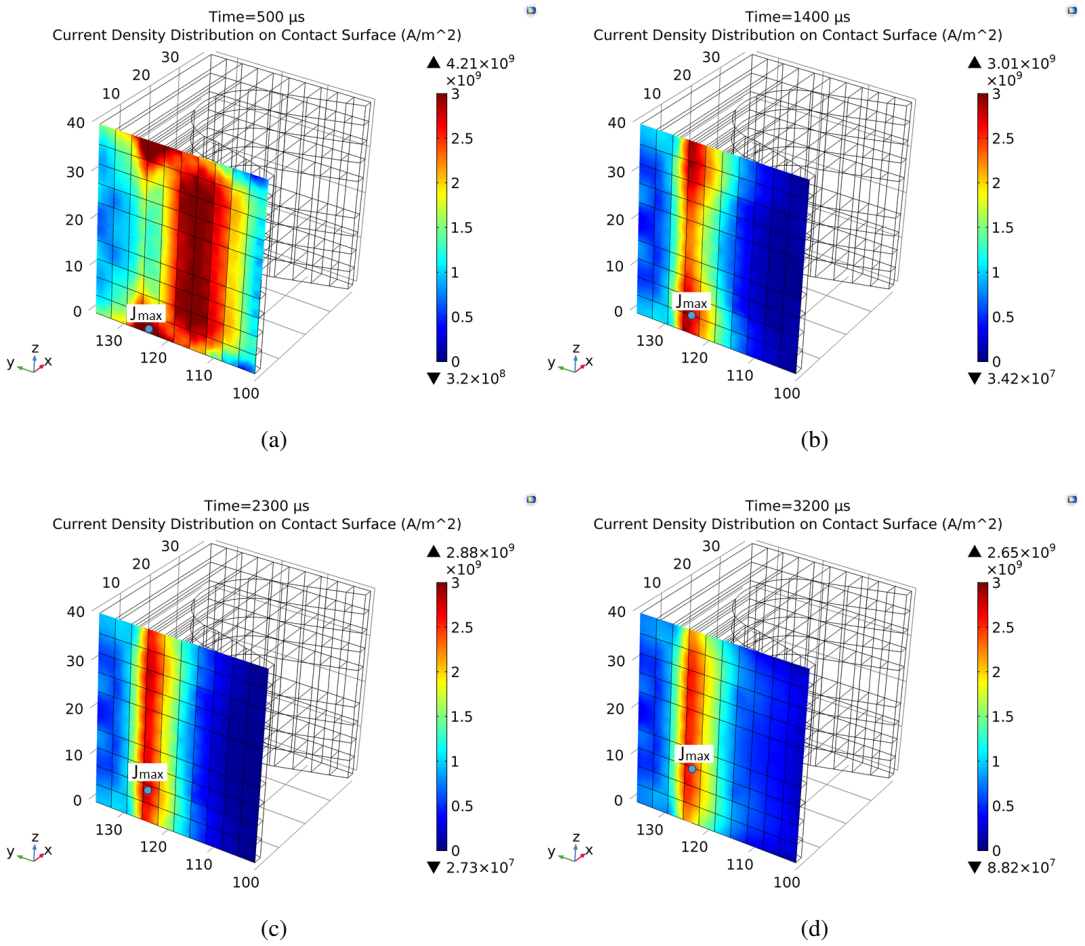

Figure 4.12: Current density distribution on the contact surface when the magnitude of the excitation current is equal to its peak value, [53].

In Eq. (4.3), equation of energy required to melt per unit volume of aluminum material of armature is given. In Eq. (4.3), m is the mass of per unit volume of aluminum, c is the heat capacity of aluminum (900 J/kgK), ΔT is the required temperature to

melt the armature (635.3°C for 25°C room temperature), V is the volume of per unit volume and d is the density of aluminum material (2700 kg/m^3).

$$Q = m\,c\,\Delta T = V\,d\,c\,\Delta T \tag{4.3}$$

Equation of energy loss at that per unit volume is given in Eq. (4.4), where $J_{cri}(t)$ is the critical maximum current density waveform, ρ is aluminum resistivity (2.65 10^{-8} Ωm), t_{last} is the time value when the current reaches zero (i.e. 4.5 ms).

$$Q = \oint \int_0^{t_{last}} J_{cri}^2(t)\rho\,dt\,dV \tag{4.4}$$

Since it is assumed that the position of the maximum current density point does not change during the excitation, time integration of square of $J_{cri}(t)$ waveform can be found using Eq. (4.5).

$$\int J_{cri}^2\,dt = \frac{d\,c\,\Delta T}{\rho} \tag{4.5}$$

In [53], it is shown that maximum value of the critical current density for this excitation current waveform is found to be 4.04 10^9 A/m^2. It means that if the value of maximum current density on the contact surface exceeds this critical value, aluminum material of the armature starts to melt.

4.2.4 Flow Chart of the Optimization

FE model is used to calculate the objective function. Also, genetic algorithm (GA) is used as optimization method. Penalty constraint method is used for the described constraints. Flow chart of the optimization algorithm is given in Fig. 4.13.

Each population has 20 different armature geometries. Objective function given in Eq. (4.2) is calculated using FE model for each armature design. Then, unique sorting, and selecting methods are implemented. After sorting the individuals (armature geometries), elitism, crossover, and mutation filters are applied. Hence, the new gen-

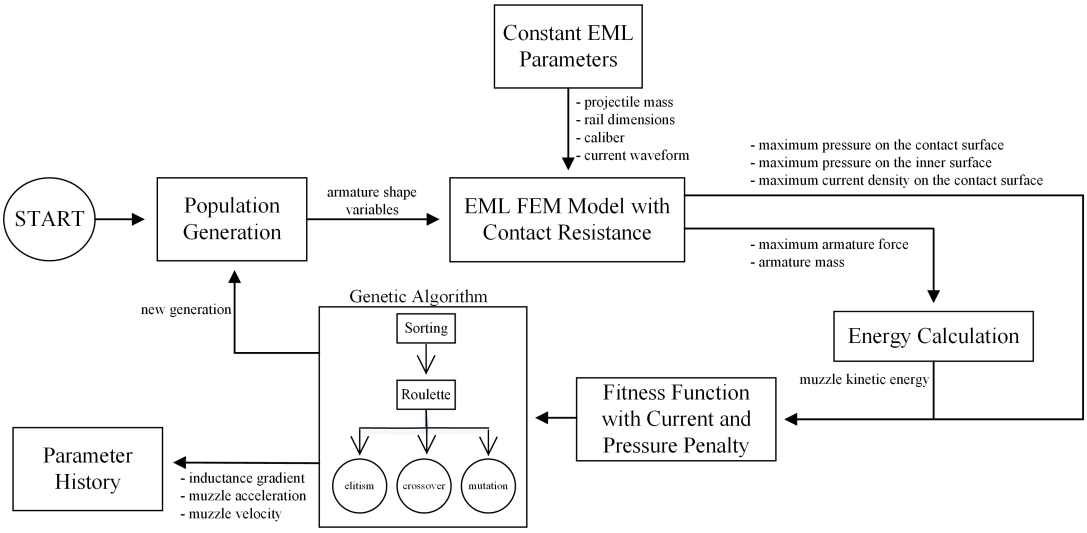

Figure 4.13: Flowchart of optimization, [53].

eration converges to the optimum point using the roulette wheel selection method as in Fig. 4.13.

4.2.5 Contact Resistance Modeling

The main problem in armature shape optimization is the risk of melting the aluminum material of the armature due to the large and nonuniform current density distribution. Therefore, contact resistance should be included in the optimization, as explained in Section 2.2.3. Contact resistance is modeled as two layers between the rails and armature. Armature and contact layer are divided into 100 pieces as in Fig 4.14. Although aluminum material of armature has a constant resistivity value: 2.65 10^{-8} Ωm , resistivity of a contact layer piece is dependent of contact force acting on it. Contact force consists of mechanical preload and electromagnetic contact force parts as in Eq. (4.6).

$$F_c(t) = F_{pre\text{-}load} + F_{em}(t) \tag{4.6}$$

In [51], an empirical equation is found using the experiment of electrical contact

between a rotating disc and a stationary conductor, as in Eq. (4.7).

$$R_c(t,y,z) = \frac{19.2}{\mathrm{F_c}(t,y,z)} = \rho_c(t,y,z)\frac{l}{\mathrm{A}} \tag{4.7}$$

Then, the position and time dependent resistivity of each contact layer piece can be calculated using Eq. (4.8).

$$\rho_c(t,y,z) = \frac{19.2\mathrm{A}}{\mathrm{F_c}(t,y,z)\,l} = \frac{19.2}{\mathrm{P_c}(t,y,z)\,l} \tag{4.8}$$

In the final formula for the resistivity of each contact layer piece, Eq. (4.7), A is the area of one contact layer piece which changes for different armature shapes, l is the thickness of the contact layer which is chosen as 0.5 mm in this study and $\mathrm{P_c}$ is the average contact pressure for each contact layer piece.

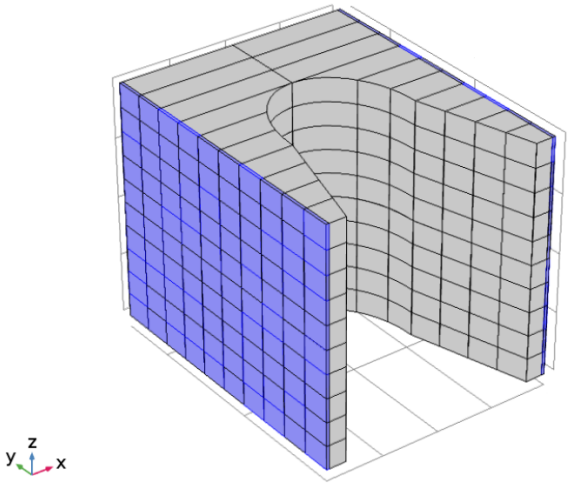

Figure 4.14: Contact layers with pressure-dependent conductivities, [53].

4.2.6 Results of the Optimization Study

Solving the 20 iterations of the algorithm takes around 120 hours with the workstation computer used in the lab with 16 GB RAM and Intel(R) Xeon (R) i7 CPU E3-1271 v3 @ 3.60 GHz processor.

In Fig. 4.15, the variation of the geometric independent variables during the optimization is given. In Fig. 4.15 each blue dot represents one individual. Dark blue dot means larger individual density in the population. Moreover, green lines show the change of the fittest individual in each generation. The converged values of the independent variables described in Fig. 4.11 are given in Table 4.3.

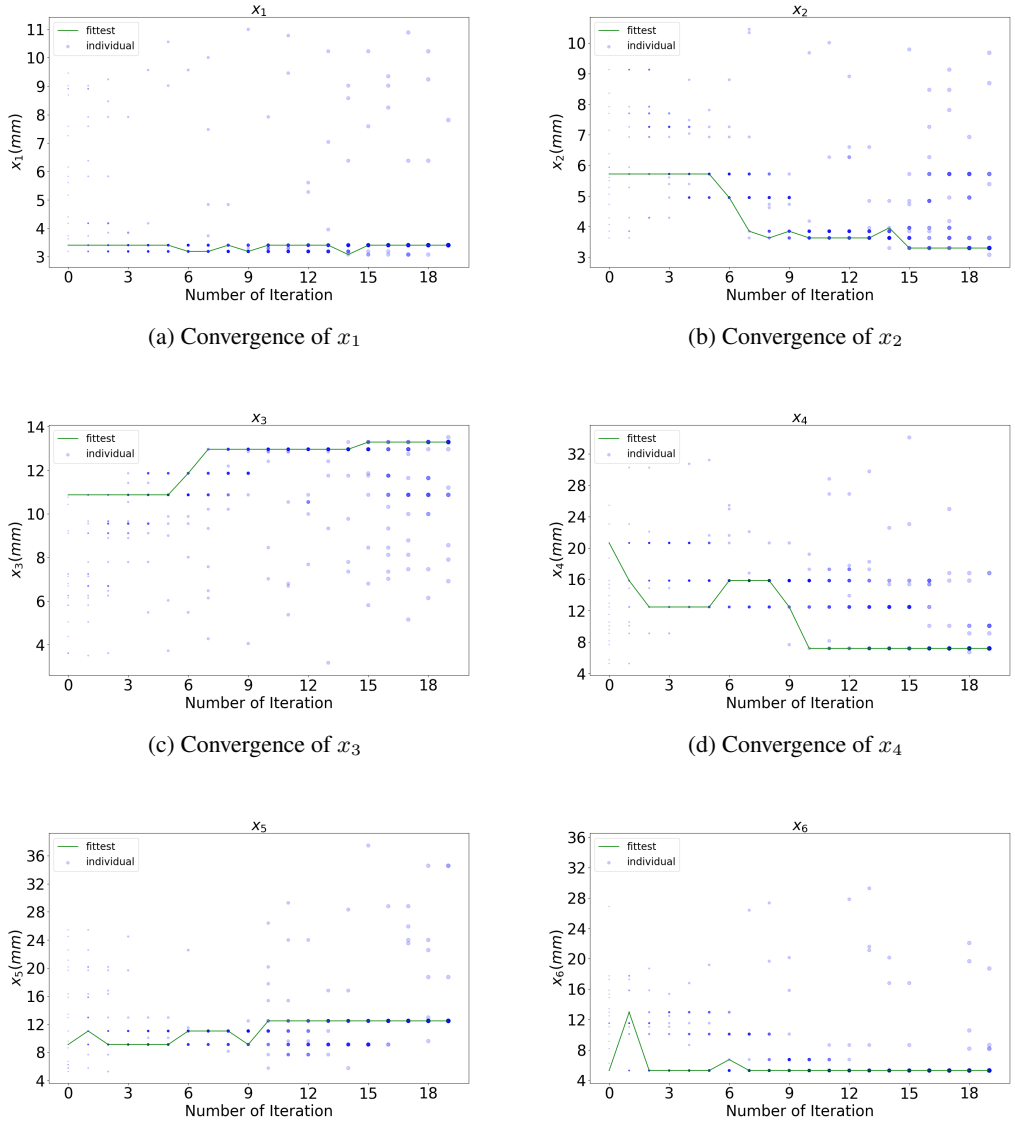

(a) Convergence of x_1

(b) Convergence of x_2

(c) Convergence of x_3

(d) Convergence of x_4

(e) Convergence of x_5

(f) Convergence of x_6

Figure 4.15: Variation of the independent variables during the optimization, [53].

Fig. 4.16 shows the current density distribution for the optimum armature geometry which created by the converged geometric parameters. It can be observed that, due to

Table 4.3: Optimum values of geometric parameters, [53].

$\mathbf{x_1}$	3.4 mm
$\mathbf{x_2}$	3.3 mm
$\mathbf{x_3}$	13.3 mm
$\mathbf{x_4}$	7.2 mm
$\mathbf{x_5}$	12.5 mm
$\mathbf{x_6}$	5.3 mm

the contact resistance layer, current enters the armature from its leading edge instead of trailing edge as discussed in [71].

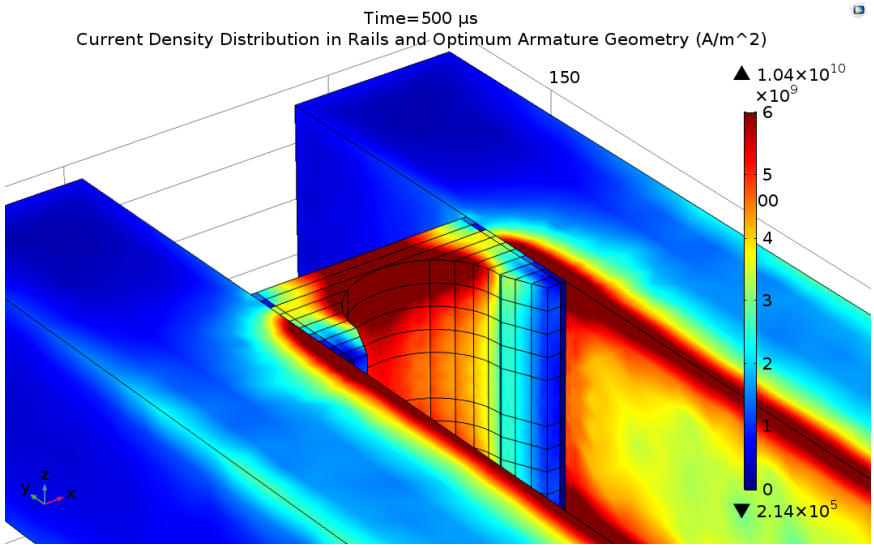

Figure 4.16: Optimum armature geometry and rails with their current density distribution, [53].

Fig. 4.17 shows the main outputs of the optimization algorithm. Fig. 4.17 (c) shows that the current density in the fittest armature geometry (green solid line) never exceeds the critical current density value (red solid line). Although inductance gradient of EML does not change in a wide range, muzzle kinetic energy and velocity of the projectile increase significantly during the optimization. In addition to the penalty functions, the increase of muzzle kinetic energy and velocity can be observed in Fig. 4.17 (a) and (b). Moreover, in Table 4.4, the converged values of the optimization outputs are given.

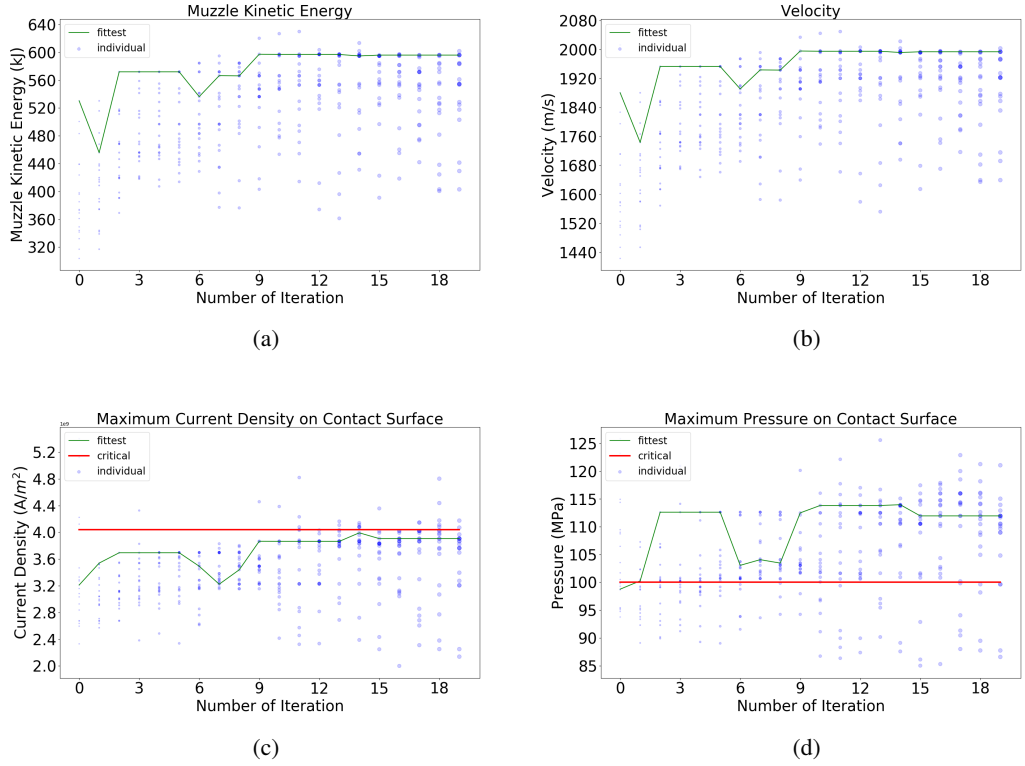

Figure 4.17: Iteration of main optimization outputs, [53].

Table 4.4: Converged values of the optimization outputs, [53].

Kinetic Energy	596 kJ
Velocity	1993 m/s
Inductance Gradient	0.4 μH/m
Maximum Pressure	112 MPa
Mass of Armature	51 g
Maximum Current Density	$3.91\,10^9$A/m^2

To sum up, as discussed in the conclusion part of [53], EML has 6% total system efficiency while the efficiency of the accelerator is found to be 47%. Moreover, although using shorter armature increases the magnetic flux density behind the armature and the force acting on the armature, it also increases the pressure beyond a value that damages the material. Moreover, x_5 directly affects the maximum value of the contact current density. Increasing x_5 is a solution for the armature contact surface melting.

One interesting outcome of this study is that the maximum armature force does not mean the maximum projectile muzzle kinetic energy. In addition, although the large armature mass decreases the acceleration and muzzle kinetic energy, there exist contact current density and armature damaging pressure constraints, which influence the size of the armature.

CHAPTER 5

CONCLUSIONS AND FUTURE WORK

5.1 Conclusions

To sum up, a detailed and multi-physics FE model of Tufan EML is developed in this study. Pulsed power supply of the EML in the study has 10 modules each of which has 200 kJ electrical energy. With the given PPS component parameters and switching scenario, rail current reaches approximately 1 MA at 0.7 ms. Some critical outputs of the developed FE model is given in Table 5.1.

Moreover, it is significant to note that EML system is a multiphysics problem. Therefore, in addition to the power electronics (like PPS modules) and electromagnetic concepts in the barrel side (like skin, proximity, velocity skin effects, induced back EMF), contact transition, friction and recoil have been taken into account. In general, there exist two main challenges in the modeling of an EML: the fact that electrical and magnetic circuit change during the armature movement and requirement of combined model of the PPS and the barrel.

In order to calculate the armature force accurately, it is required to use quite fine mesh elements around the armature. However, since the armature moves between 3 m long rails, the simulation of armature movement with a 3D moving mesh structure has large computational cost. Therefore, in the developed model, although armature is stationary at the preload position, the armature movement is emulated by external variable resistances and inductances: AC resistance, VSE resistance, contact resistance, back EMF resistance and inductance due to the armature motion to take the change of electrical circuit of the barrel into account. Analytic and numeric calculations to find the equations for these resistances and inductances are discussed in

Table 5.1: Some critical outputs of the developed FE model.

Maximum breech voltage	1.9 kV
Maximum magnetic flux density between the rails	22.3 T
Maximum total electromagnetic deflection force acting on one rail	4300 kN
Average deflection pressure on one rail	170 MPa
Maximum deflection pressure just behind the armature on one rail	250 MPa
Maximum electromagnetic force acting on the armature	230 kN
Maximum frictional force acting on the armature	20 kN
Inductance gradient	0.44 μH/m
Maximum armature acceleration	1.6 10^6 m/s^2
Armature exit time	2.25 ms
Rail current at armature exit time	320 kA
Muzzle velocity	2040 m/s
Muzzle kinetic energy	260 kJ
Efficiency of the total system	13%
Maximum temperature change in the armature	1120 K
Maximum temperature change in the rails	445 K
Maximum recoil force acting on the busbars	100 kN

Chapter 2. These parameters depend on the armature position and velocity, frequency of excitation current and inductance gradient.

In addition to the armature movement, another challenge is the voltage excitation. FE model of an EML with current excitation does not give realistic results. Because, the change of electrical parameters of the rails and armature effect the excitation current waveform. Therefore, PPS modules have to be integrated into the FE model. The developed model for Tufan EML consists of both electrical simulation of PPS side and electromagnetic simulation of the barrel side.

In Section 3.1, the variation of barrel resistance components during the excitation is discussed. It can be observed that most of the resistive loss is due to the VSE resistance in the barrel side of the EML. In order to find VSE resistance equations for the rails and armature, a 2D moving mesh model is developed. Using this model, effect

of the armature velocity and position on the VSE resistances is observed. Moreover, it is shown that although contact resistance is large at the beginning and last part of the excitation, it is negligible when the current is at its peak value. Then, in Section 4.2, it is shown that although contact resistance does not have large effect on the waveform of the excitation current, it is critical for the armature design. Moreover, due to the change of both magnetic flux between the rails and inductance of the barrel, there have to be an extra resistance term called back EMF resistance in the model as derived in Section 3.1. AC resistance due to the skin and proximity effects is also calculated during the excitation. It is observed that AC resistance of the rails is influenced by the frequency of the excitation current. Also, it increases with the armature position. In addition to the barrel resistance, the variation of its inductance during the excitation is also investigated. It is observed that the inductance of the barrel depends on only the position of the armature. Inductance of the rails per meter is called inductance gradient which affects the electromagnetic force acting on the armature in the acceleration direction, directly.

Furthermore, it can be concluded that the current density distribution in the rails is affected by the skin, proximity and velocity skin effects. Due to these effects, magnitudes of the current density and the magnetic field are maximum at the contact surfaces of the rails between the rails and armature. Moreover, while the direction of the electromagnetic force acting on the armature is in Y-direction, the one on the rails is in X-direction. It is observed that the electromagnetic pressure acting on the rails is maximum at the position of just behind the armature position. Also, it is investigated that, just after the beginning of the excitation, the electromagnetic contact force becomes much larger than the mechanical contact force due to the preload. However, since the dynamic friction coefficient decreases with increasing armature velocity, frictional force acting on the armature has a peak value just after the beginning of the excitation. One significant outcome of the study is the fact that it is not enough to integrate the magnetic flux density between the rails to calculate the inductance of the barrel. Positive flux densities in the rails also have to be taken into account for the inductance calculation of the barrel.

In addition to development of the FE model, optimization of EML's two crucial parts is also discussed in this study: lamination thickness of the containment and shape

of the armature. Although it is a must to use a containment to support the rails mechanically, it causes eddy current loss in the system. In Section 4.1, it is observed that without any lamination, the solid containment decreases the normalized muzzle kinetic energy to 0.72. However, it is observed that normalized muzzle kinetic energy is 0.98 with 10 mm laminated containment. It is important to note that structural analysis of the designed containment has to be performed in addition to the electromagnetic analysis. However, the structural analysis is beyond the scope of this thesis. Moreover, in Section 4.2, armature shape optimization study shows that armature shape influences not only muzzle kinetic energy but also the maximum current density on the contact surface and maximum electromagnetic pressure acting on the armature. For instance, while x_5 effects the current density on the contact surface, x_6 has large influence on the armature mass and muzzle kinetic energy. Moreover, although shorter armature increases the electromagnetic force acting on the armature, it also increases the damaging electromagnetic pressure on it.

5.2 Future Work

The development of a FE model for the proposed EML, the optimization of armature geometry and effect of laminated containment were presented in this thesis. While the proposed FE model has good agreement with the experimental results, which are not presented in this thesis due to the confidentiality agreement between ASELSAN Inc. and subcontractor in METU, some possible future works may be conducted to further improve the proposed model to get better contact transition and larger efficiencies:

- **Rail Geometry Optimization:** The EML analyzed in this thesis has rectangular cross-section. As discussed in Section 1.5.2, since the rails with rounded cross-section have larger contact area than the rectangular rail geometries, they may provide better contact transition. Also, it may possible to increase the mechanical strength of both rails and armature by rounded rails. An optimization procedure may be developed for the geometric parameters of the rounded rails to get more uniform contact current density distribution in the contact surface and maximize the mechanical strength of the rails and armature.

- **Analysis of Brushed and Plasma Type Armatures:** The analysis and optimization of the C-shaped solid armature of the proposed EML were presented in this thesis. Investigation of the brushed and plasma type armatures were out of the scope of this study. Although, these types of armatures may increase the efficiency of the system, they have more complex structures than the solid armatures.

- **Analysis of Inductive PPS and Pulsed Alternator:** Capacitor based PPS was used in the investigated EML. As discussed in Section 1.4, there exist two alternatives to excite an EML: inductive PPS and pulsed alternator. These topologies can be analyzed and compared with the capacitive PPS in terms of efficiency, cost and power density.

- **Study on Rail and Armature Materials:** Copper, aluminum and stainless steel are commonly used materials in rails, armature and containment, respectively, because of their conductivity, mechanical strength and permeability. Also, in this thesis, these materials are used in the EML. However, efficiency can be increased using a more conductive material in the rails and containment. Also, the most important limitation to increase the excitation energy of an EML is the mechanical strength of the rails and armature. The excitation energy can be increased by developing their mechanical strength.

REFERENCES

[1] L. Tang, J. He, L. Chen, S. Xia, and D. Feng, "Study of some influencing factors of armature current distribution at current ramp-up stage in railgun," *IEEE Trans. Plasma Sci.*, vol. 43, no. 5, pp. 1585–1591, 2015.

[2] C. Gong, X. Yu, and X. Liu, "Study on the system efficiency of the capacitive pulsed-power supply," *IEEE Transactions on Plasma Science*, vol. 43, no. 5, pp. 1441–1447, 2015.

[3] J. Lan, "Design and optimization of the pulsed power supply system used for electromagnetic railgun," *Conference Proceedings - 2012 16th International Symposium on Electromagnetic Launch Technology, EML 2012*, pp. 1–4, 2012.

[4] T. G. Engel, J. M. Neri, and M. J. Veracka, "The maximum theoretical efficiency of constant inductance gradient electromagnetic launchers," *IEEE Transactions on Plasma Science*, vol. 37, no. 4 PART 2, pp. 608–614, 2009.

[5] T. G. Engel, J. M. Neri, and M. J. Veracka, "The velocity and efficiency limiting effects of magnetic diffusion in railgun sliding contacts," *2008 14th Symposium on Electromagnetic Launch Technology, EML, Proceedings*, no. 4, pp. 417–421, 2008.

[6] M. Karagoz, Y. Çevik, E. Tan, A. Civil, O. Cavbozar, U. Gocmen, B. Yildirim, E. Durna, and M. S. Sahin, "ASELSAN EMFY-1 electromagnetic launcher: first experiments," in *IEEE 21st International Conference on Pulsed Power*, no. 3150230, 2017.

[7] I. R. McNab, "Early electric gun research," *IEEE Trans. Magn.*, vol. 35, no. 1, pp. 250–261, 1999.

[8] H. Kolm, P. Mongeau, and F. Willisms, "Electromagnetic launchers. (1980)," *IEEE Trans. Magn.*, vol. MAG-16, no. 5, pp. 719–721, 1980.

[9] A. Egeland, "Birkeland's electromagnetic gun: a historical review," *IEEE Transactions on Plasma Science*, vol. 17, no. 2, pp. 73–82, 1989.

[10] A. L. O. Fauchon-Villeplee, "Canons electriques," 1920.

[11] P. Lehmann, "Overview of the electric launch activities at the French-German Research Institute of Saint-Louis (ISL)," *IEEE Transactions on Magnetics*, vol. 39, no. 1, pp. 24–28, 2003.

[12] J. McFarland and I. R. McNab, "A long-range naval railgun," *IEEE Transactions on Magnetics*, vol. 39, no. 1 I, pp. 289–294, 2003.

[13] I. R. McNab, F. Stefani, M. Crawford, M. Erengil, C. Persad, S. Satapathy, H. Vanicek, T. Watt, and C. Dampier, "Development of a naval railgun," *IEEE Transactions on Magnetics*, vol. 41, no. 1, pp. 206–210, 2005.

[14] H. D. Fair, "Advances in electromagnetic launch science and technology and its applications," *IEEE Transactions on Magnetics*, vol. 45, no. 1, pp. 225–230, 2009.

[15] J. Hansler, "A contribution to the problem of an electric gun: design of an electric 40-mm flak," *Halstead Exploiting Centre Report HEC 209, UT- IAT Library Report L-06446*, 1945.

[16] J. S. Bernardes, M. F. Stumborg, and T. E. Jean, "Analysis of a capacitor-based pulsed-power system for driving long-range electromagnetic guns," *IEEE Transactions on Magnetics*, vol. 39, no. 1, pp. 486–490, 2003.

[17] P. Liu, J. Li, Y. Gui, S. Li, Q. Zhang, and N. Su, "Analysis of energy conversion efficiency of a capacitor-based pulsed-power system for railgun experiments," *IEEE Transactions on Plasma Science*, vol. 39, no. 1 PART 1, pp. 300–303, 2011.

[18] X. Guo, L. Dai, Q. Zhang, F. Lin, Q. Huang, and T. Zhao, "Influences of electric parameters of pulsed power supply on electromagnetic railgun system," *IEEE Transactions on Plasma Science*, vol. 43, no. 9, pp. 3260–3267, 2015.

[19] S. Ma, X. Yu, and Z. Li, "Conceptual design and comparison for 100-kJ inductive pulse power supplies," *IEEE Transactions on Plasma Science*, vol. 45, no. 7, pp. 1196–1201, 2017.

[20] K. Lindner, J. Long, D. Girogi, T. Navapanich, and O. Zucker, "A meatgrinder circuit for energizing resistive and varying inductive loads (EM guns)," *IEEE Trans. Magn.*, vol. Mag-22, no. 6, pp. 1591–1596, 1986.

[21] X. Yu, X. Liu, and S. Member, "Overview of circuit topologies for inductive pulsed power supplies," *CES Transaction on Electrical Machines and Systems*, vol. 1, no. 3, pp. 265–272, 2017.

[22] R. D. Ford, R. D. Hudson, and R. T. Klug, "Novel hybrid XRAM current multiplier," *IEEE Transactions on Magnetics*, vol. 29, no. 1, pp. 949–953, 1993.

[23] W. Carey and J. Mayes, "Marx generator design and performance," *Conference Record of the Twenty-Fifth International Power Modulator Symposium, 2002 and 2002 High-Voltage Workshop.*, pp. 625–628, 2002.

[24] O. Libfried, V. Brommer, and S. Scharnholz, "Development of XRAM generators as inductive power sources for very high current pulses," *Pulsed Power Conference*, pp. 2–7, 2013.

[25] P. Dedié, V. Brommer, and S. Scharnholz, "Twenty-stage toroidal XRAM generator switched by countercurrent thyristors," *IEEE Transactions on Plasma Science*, vol. 39, no. 1 PART 1, pp. 263–267, 2011.

[26] J. E. King, R. M. Kobuck, and J. R. Repp, "High speed water-cooled permanent magnet motor for pulse alternator-based pulse power systems," *2008 14th Symposium on Electromagnetic Launch Technology, EML, Proceedings*, pp. 475–480, 2008.

[27] C. Ye, K. Yu, Z. Lou, Z. Ren, and Y. Pan, "Investigation of pulse excitation in air-core pulsed-alternator system," *IEEE Trans. Plasma Sci.*, vol. 39, no. 1, pp. 342–345, 2011.

[28] S. Cui, S. Wang, S. Wu, O. S. Yuryevich, and I. M. Milyaev, "Research of a modular pulsed alternator power system," *IEEE Transactions on Plasma Science*, vol. 45, no. 7, pp. 1406–1413, 2017.

[29] L. Chen, J. He, Z. Xiao, S. Xia, D. Feng, and L. Tang, "Experimental study of armature melt wear in solid armature railgun," *IEEE Transactions on Plasma Science*, vol. 43, no. 5, pp. 1142–1146, 2015.

[30] O. Liebfried, M. Schneider, and S. Balevicius, "Current distribution and contact mechanisms in static railgun experiments with brush armatures," *IEEE Transactions on Plasma Science*, vol. 39, no. 1 PART 1, pp. 431–436, 2011.

[31] B. Wild, F. Alouahabi, D. Simicic, M. Schneider, R. Hoffman, and A. R. Rafira, "A Comparison of C-Shaped and Brush Armature Performance," *IEEE Trans. Plasma Sci.*, vol. 45, no. 7, pp. 1227–1233, 2017.

[32] R. A. Marshall, "Structure of plasma armature of a railgun," *IEEE Trans. Magn.*, vol. Mag-22, no. 6, pp. 1609–1612, 1986.

[33] R. L. Ellis, J. C. Poynor, B. T. McGlasson, and A. N. Smith, "Influence of bore and rail geometry on an electromagnetic naval railgun system," *IEEE Transactions on Magnetics*, vol. 41, no. 1 II, pp. 182–187, 2005.

[34] L. Jin, B. Lei, Q. Zhang, and R. Zhu, "Electromechanical performance of rails with different cross-sectional shapes in railgun," *IEEE Trans. Plasma Sci.*, vol. 43, no. 5, pp. 1220–1224, 2015.

[35] M. S. Bayati and A. Keshtkar, "Novel study of the rail's geometry in the electromagnetic launcher," *IEEE Trans. Plasma Sci.*, vol. 43, no. 5, pp. 1652–1656, 2015.

[36] J. V. Parker, S. Levinson, and W. B. Lane, "Loss of propulsive force in railguns with laminated containment," *IEEE Trans. Magn.*, vol. 35, no. 1, pp. 442–446, 1999.

[37] J. Mallick, "Phenomenological electromagnetic modeling of laminated-containment launchers," *IEEE Trans. Magn.*, vol. 43, no. 1, pp. 359–363, 2007.

[38] D. Ceylan and O. Keysan, "Effect of conducting containment on electromagnetic launcher efficiency," *2017 18th International Symposium on Electromagnetic Fields in Mechatronics, Electrical and Electronic Engineering, ISEF 2017*, 2017.

[39] E. L. Kathe, "Recoil considerations for railguns," *IEEE Transactions on Magnetics*, vol. 37, no. 1 I, pp. 425–430, 2001.

[40] D. R. Sadedin, "Conservation of momentum and recoil in the railgun," *IEEE Transactions on Magnetics*, vol. 33, no. 1, pp. 599–603, 1997.

[41] L. Shoubao, R. Jiangjun, D. Zhiye, W. Dong, and Z. Chun, "Calculation of railgun inductance gradient by 2-D finite element method," *2008. ICEMS 2008. International Conference on Electrical Machines and Systems*, no. 8, pp. 4057–4060, 2008.

[42] K. T. Hsieh, S. Satapathy, and M. T. Hsieh, "Effects of pressure-dependent contact resistivity on contact interfacial conditions," *IEEE Trans. Magn.*, vol. 45, no. 1, pp. 313–318, 2009.

[43] X. Yu and Z. Fan, "Simulation and two-objective optimization of the electromagnetic-railgun model considering VSEC resistance and contact resistance," *IEEE Trans. Plasma Sci.*, vol. 39, no. 1 PART 1, pp. 405–410, 2011.

[44] M. S. Bayati, A. Keshtkar, and A. Keshtkar, "Transition study of current distribution and maximum current density in railgun by 3-D FEM-IEM," *IEEE Transactions on Plasma Science*, vol. 39, no. 1, pp. 13–17, 2011.

[45] J. P. Barber, D. P. Bauer, K. Jamison, J. V. Parker, F. Stefani, and A. Zielinski, "A survey of armature transition mechanisms," *IEEE Transactions on Magnetics*, vol. 39, no. 1 I, pp. 47–51, 2003.

[46] J. P. Barber and Y. A. Dreizin, "Model of contact transitioning with realistic armature-rail interface," *IEEE Transactions on Magnetics*, vol. 31, no. 1, pp. 96–100, 1995.

[47] J. P. Barber and R. A. Marshall, "The velocity skin effect on plasma armatures in railguns," *IEEE Transactions on Plasma Science*, vol. 17, no. 3, pp. 450–454, 1989.

[48] L. E. Thurmond and J. P. Barber, "Measurement of the velocity skin effect," *IEEE Transactions on Magnetics*, vol. 27, no. 1, pp. 326–328, 1991.

[49] T. G. Engel, J. M. Neri, and M. J. Veracka, "Characterization of the velocity skin effect in the surface layer of a railgun sliding contact," *IEEE Transactions on Magnetics*, vol. 44, no. 7, pp. 1837–1844, 2008.

[50] R. Holm, *Electric Contacts Handbook*. 1958.

[51] J. Xu and K. Li, "The research on resistance of electric contact," in *J. Elect. Eng. Mater*, no. 1, pp. 10–13, 2011.

[52] Y. Zhou, D. Zhang, and P. Yan, "Modeling of electromagnetic rail launcher system based on multifactor effects," *IEEE Trans. Plasma Sci.*, vol. 43, no. 5, pp. 1516–1522, 2015.

[53] D. Ceylan, U. Gudelek, M, and O. Keysan, "Armature shape optimization of an electromagnetic launcher including contact resistance," *IEEE Transactions on Plasma Science (Early Access)*, no. 99, pp. 1–9, 2018.

[54] S. Aigner and E. Igenbergs, "Friction and ablation measurements in a round bore railgun," *IEEE Transactions on Magnetics*, vol. 25, no. 1, pp. 33–39, 1989.

[55] H. Zhao, J. A. Souza, and J. C. Ordonez, "Three-dimensional launch simulation and active cooling analysis of a single-shot electromagnetic railgun," *Simulation: Transaction of the sicient for modeling and simulation international*, vol. 90, no. 12, pp. 1312–1327, 2014.

[56] I. Kohlberg and W. O. Coburn, "A solution for the three dimensional rail gun current distribution and electromagnetic fields of a rail launcher," *IEEE Transactions on Magnetics*, vol. 31, no. 1, pp. 628–633, 1995.

[57] R. Stonkus, J. Račkauskas, M. Schneider, and R. Kačianauskas, "Structural mechanics of railguns with open barrels and elastic supports: The influence of multishot operation," *IEEE Transactions on Plasma Science*, vol. 43, no. 5, pp. 1510–1515, 2015.

[58] H. Zhao, J. A. Souza, and J. C. Ordonez, "Three-dimensional launch simulation and active cooling analysis of a single-shot electromagnetic railgun," *Simulation: Transactions of the Society for Modeling and Simulation International*, vol. 90, no. 12, pp. 1312–1327, 2014.

[59] E. A. Witalis, "Origin, location, magnitude and consequences of recoil in the plasma armature railgun," *IEE Proc.-Sci. Meas. Technol.*, vol. 144, no. 1, pp. 197–200, 1995.

[60] M. Schneider, J. Račkauskas, and M. J. Löffler, "Electromechanical modeling of components of a linear electromagnetic accelerator," *IEEE Transactions on Plasma Science*, vol. 41, no. 10, pp. 2796–2799, 2013.

[61] C. C. Su, "Mechanisms for the longitudinal recoil force in railguns based on the lorentz force law," *IEEE Transactions on Magnetics*, vol. 42, no. 9, pp. 2193–2195, 2006.

[62] Z. Su, W. Guo, B. Cao, Y. Chen, K. Huang, and X. Ge, "The study of the simple breech-fed railgun recoil force," *Conference Proceedings - 2012 16th International Symposium on Electromagnetic Launch Technology, EML 2012*, pp. 7–10, 2012.

[63] D. Landen and S. Satapathy, "Eddy current effects in the laminated containment structure of railguns," *IEEE Transactions on Magnetics*, vol. 43, no. 1, pp. 150–156, 2007.

[64] Y. Lou, G. Wan, Y. Jin, B. Tang, and B. Li, "Research on energy loss distribution of an augmented railgun," *IEEE Transactions on Plasma Science*, vol. 44, no. 5, pp. 857–861, 2016.

[65] P. Lehmann, M. D. Vo, and W. Wenning, "Comparative study of railgun housings made of modern fiber wound materials, ceramic, or insulated steel plates," *IEEE Transactions on Magnetics*, vol. 41, no. 1 II, pp. 200–205, 2005.

[66] W. Yuan and P. Yan, "Simulation of the eddy current effects on the inductance gradient of railgun," *2008 14th Symposium on Electromagnetic Launch Technology, EML, Proceedings*, vol. 1, no. c, pp. 582–584, 2008.

[67] J. Ziske, H. Neubert, and R. Disselnkötter, "Modeling of Anisotropic Laminated Magnetic Cores using Homogenization Approaches," *COMSOL Conference, Cambridge*, 2014.

[68] P. Hahne, R. D. Dietz, B. Rieth, and T. Weiland, "Determination of anisotropie equivalent conductivity of laminated cores for numerical computation," *IEEE Transactions on Magnetics*, vol. 32, no. 3 PART 2, pp. 1184–1187, 1996.

[69] B. Kim and H. Kuo, "Effect of rail/armature geometry on current density distribution and inductance gradient," *IEEE Transactions on Magnetics*, vol. 35, no. 1, pp. 413–416, 1999.

[70] S. Hundertmark, M. Schneider, D. Simicic, and G. Vincent, "Experiments to increase the used energy with the PEGASUS railgun," *IEEE Transactions on Plasma Science*, vol. 42, no. 10, pp. 3180–3185, 2014.

[71] L. Tang, J. He, L. Chen, S. Xia, D. Feng, J. Li, and P. Yan, "Influencing factors study of armature current distribution at current ramp-up in railgun," *17th International Symposium on Electromagnetic Launch Technology*, pp. 0–4, 2014.